# Modelling a gravitational launch of gravity based foundations for offshore wind turbines

## MSc Thesis

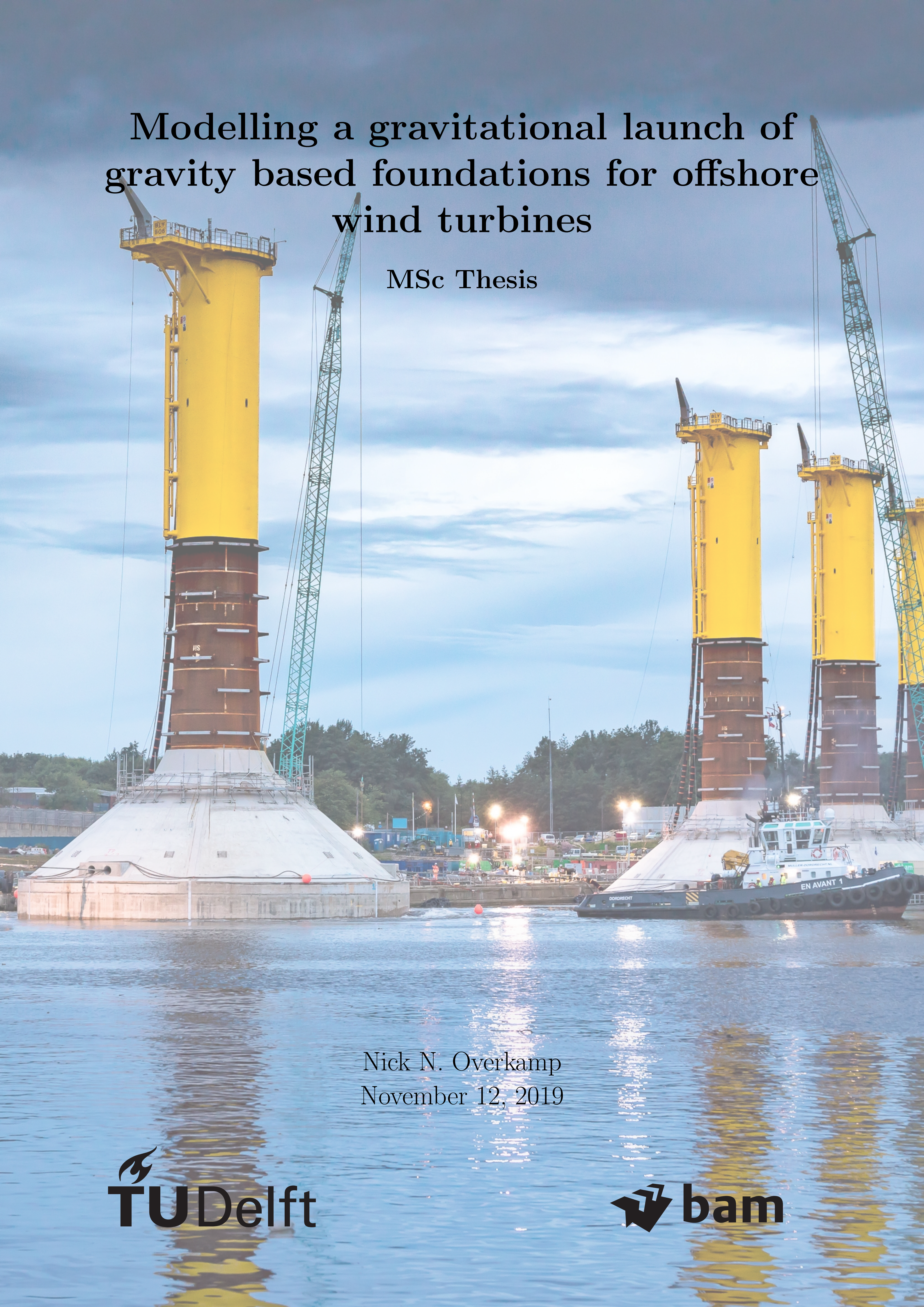

Nick N. Overkamp
November 12, 2019

Title page background image shows the float-out of the first gravity based foundation at the Blyth Offshore Demonstrator Project on 11-7-2017. The picture was obtained from BAM (2017).

# Modelling a gravitational launch of gravity based foundations for offshore wind turbines

by

**Nick N. Overkamp**

in partial fulfilment of the requirements for the degree of

**Master of Science**
in Civil Engineering

at the Delft University of Technology,
to be defended publicly on Monday November 18, 2019 at 10:00 AM.

| | | |
|---|---|---|
| Student number: | 4221869 | |
| Project duration: | January 2019 - November 2019 | |
| Graduation committee: | Prof.dr.ir. S.N. (Bas) Jonkman, | TU Delft (chair) |
| | Dr.ing. M.Z. (Mark) Voorendt, | TU Delft |
| | Dr.ir. P.C.J. (Pierre) Hoogenboom, | TU Delft |
| | Dr.ir. M. (Markus) Muttray, | BAM Infraconsult bv |

# Preface

This report is the final result of my graduation project to obtain a MSc degree in Hydraulic Engineering at the faculty of Civil Engineering and Geosciences at the Delft University of Technology.

My quest to find an interesting and challenging graduation project resulted in a subject that I was not uncommon to at the start of my graduation: gravity based foundations for offshore wind turbines. For me, this structure is the ultimate combination of sustainable energy, innovation and hydraulic engineering. I believe in the future of this product, I wanted to be a part of developing it and BAM Infraconsult gave me the opportunity to do so.

I would like to thank many people who have directly or indirectly supported my during this project. First of all, I owe many thanks to Markus Muttray and Mark Voorendt, who were somehow always available for my endless number of questions. I would like to thank Bas Jonkman and Pierre Hoogenboom for their valuable contributions in the committee meetings.

Additionally, I would like to thank the whole Coastal Engineering and Marine Engineering departments at BAM Infraconsult for their kindness and support, and Martijn Meijer specifically for giving me this opportunity. Special thanks are in order for Ikbal Kelkitli, for always answering his phone when I had questions about the testing facility and of course also for the 'gezelligheid' during my days in Gouda. Also, my thanks go out to Erik ten Oever, who proposed this project and constructed the GBF scale model.

I want to thank my friends, housemates and rowing teams for making my student years a very fun period of my life. Their energy has always kept me positive and motivated me to work hard but balanced. Last but definitely not least, I thank my family and girlfriend for their unconditional love and support.

*Nick Overkamp*
*Den Haag, November 2019*

# Summary

**Figure 1:** Image of a gravitational launch of a GBF during an experiment performed for this thesis.

This thesis focuses on modelling a gravitational launch of gravity based foundations (GBF's) for offshore wind turbines. This is an extension of the Blyth Offshore Demonstrator project by BAM Infraconsult. To become more competitive in the offshore wind energy market, the construction of self-buoyant GBF's installed using the 'float and submerge' technique needs to be optimized. GBF's will need to be constructed on land, which calls for a way to 'launch' the GBF's. Another study suggests the use of semi-submersibles or immersion structures, which are very expensive. Due to the GBF's high strength and stability, it might be suitable for a gravitational launch. Although these launching methods have been widely applied on steel ships and jackets, the application for reinforced concrete structures is rare, especially using slipways with an abrupt ending. A conceptual design is needed to test the technical and economic feasibility of this launching technique. For the purpose of making a conceptual design, the launching process must be modelled. The goal of this thesis is to develop models that can be used in a conceptual design phase to easily determine the optimal shape and dimension of the slipway used to gravitationally launch GBF's. This thesis contains three modelling methods: (simple) mathematical models, physical scale model tests and a Computational Fluid Dynamics (CFD) model in ANSYS Fluent.

Simple mathematical models were derived to model each phase of the launching process. Translational movements when the GBF is in full contact with the slipway were described using a simple force balance, both for a dry and a partially submerged slipway. For the kinematics as it tips over the slipway edge, equations of motion were derived and solved. The main limitation of this set of equations of motion is that hydrodynamic forces are not included. For the kinematics of the freely floating structure, equations of motions were solved and hydrodynamic components were determined analytically from literature and numerically using ANSYS Aqwa.

Physical scale model tests were performed to (1) validate and calibrate the mathematical models, (2) determine the most favourable slipway geometry, and (3) develop more insight into the GBF behaviour during a gravitational launch. The tests were conducted at a 1:100 scale. For calibration of the hydrodynamic components, free decay tests were performed. In the abruptly ending slipway launch tests, slipway inclination (9°, 14° and 21°), freeboard height (positive, zero and negative), and initial GBF velocity (high and low) were taken as variables to investigate their effect on the severity of GBF dynamics. Severity of the dynamics was parameterized by the maximum GBF rotation measured around the horizontal axis during the launch (pitch). A large GBF rotation means large motion amplitudes thus violent movements, which are undesirable.

Comparisons to mathematical models show good agreement in most cases after a calibration of the hydrodynamic components. The full launch procedure was not modelled accurately by the mathematical models. An empirical formula was developed relating the slipway variables to maximum GBF rotation, which provided more accurate results for a larger range of variables. A lower freeboard and a steep slipway inclination was always favourable. That is, within the range of tested variables, most favourable in terms of maximum GBF rotation. No such trend was observed for the initial velocity. For approximately half of the set-ups, a higher initial velocity was beneficial while the opposite is true for the other half. Most favourable slipway geometry tested had a slipway inclination of 21° and a slipway ending below the water surface (negative freeboard), resulting in a maximum GBF rotation of 29° around the horizontal axis. This was the only variant that did not cause a 'splash'. Least favourable was a 9° slipway ending above the water, resulting in a GBF rotation of 62°.

A CFD modelling strategy was proposed and used to compare to the physical model tests. The CFD model was set-up in 3D using a dynamic mesh and a three degree of freedom solver to compute all acting forces on the moving body. Despite a coarse mesh with insufficient quality, the solution converged and showed numerical stability, also for large motion amplitudes. Depending on the scale, the CFD model showed good agreement to the physical scale model tests. The CFD model has a high potential in terms of the range of initial conditions, flexibility in structure shape and dimension, and amount of output data.

The simple mathematical models (force balance, equations of motion and an empirical formula) are sufficiently accurate to analyse key differences between slipway alternatives to make choices in the conceptual design phase, after a calibration using physical scale model tests. Due to a long computational time and time consuming improvements, the CFD model is more suitable in a more detailed design phase, where it could be very valuable.

A first estimate of most important launch requirements was made using the mathematical models for abruptly ending slipways and showed technical feasibility. More research should mainly focus on improving the CFD modelling strategy and on making a conceptual design for a specific location to further investigate economic and technical feasibility.

# Table of Contents

# Chapter 1

# Motivation and background

“There is a transition ongoing and we should all be part of it”, Michael Olsen of Statoil Wind US said at the annual offshore wind conference of the American Wind Energy Association in October 2017 (John Rogers, 2017). Two weeks before publishing this thesis, the International Energy Agency said “offshore wind set to become \$1 trillion industry by 2040 in what it called ‘the most comprehensive’ study of offshore wind to date” (Jacobsen, 2019). Not only should research in this field be interesting for people who aim to make money, “renewables replacing fossil fuel is crucial to meet a globally-agreed goal of limiting temperature rise to below 2 degrees Celsius this century and the expansion of offshore wind could avoid 5-7 billion tonnes of CO2 emissions from the power sector globally.” (Jacobsen, 2019).

This chapter starts with the motivation for this thesis, after which background information led to the motivation is given. The background information contains a description of offshore wind farm trends, current knowledge on offshore wind turbine foundations and information on gravity based foundations with a focus on a specific project: the Blyth Offshore Demonstrator project by BAM Infraconsult. After a short problem analysis, the idea to gravitationally launch a gravity based foundation for offshore wind turbines is proposed, which forms the basis of this thesis. The background information in this chapter led to the problem statement of this thesis which is presented in the next chapter along with the objective, scope and a reading guide.

## 1.1 Motivation for this research

The rapidly growing offshore wind energy sector is causing new developments in the offshore wind turbine foundation market. Recent trends in the offshore wind energy market indicate a shift towards larger turbine sizes and deeper waters. While monopiles are reaching their technical limits, other wind turbine foundations, such as concrete gravity based foundations (GBF’s), are gaining popularity. Optimizing the construction of this structure calls for the use of an on-land production line. In the application of this construction method, transporting the GBF from land into water is one of the main challenges. Traditional techniques for moving large concrete structures from land to water, such as using special cranes or semi-submersible vessels, increase construction cost significantly. Low-cost gravitational launching techniques such as sliding the GBF from the side of a quay using a slipway have potential, but are very uncommon for large reinforced concrete structures. Reinforced concrete structures have been launched gravitationally in the past, but their motion is often restricted by means of winches. It is not known whether it is possible to launch concrete GBF’s for offshore wind turbines gravitationally and unrestricted.

To check this, one could perform a feasibility study in which the economic and technical feasibility is investigated. To make a cost estimate, a conceptual slipway design is required. Regarding technical feasibility, requirements for a successful launch of large concrete structures are mostly related to the GBF motions (kinematics). The design of the slipway will directly impact these kinematics. Therefore, to make a conceptual slipway design, models are required that describe the GBF kinematics for varying slipway properties such as inclination, length and ending type. The models should be sufficiently detailed to be able to compare different slipway designs and to determine the most optimal. In addition, to be useful during the conceptual design phase, the models should be simple and quick (coarse) in compliance with the general design approach, which goes from coarse to fine.

## 1.2 Background

In this problem analysis, relevant background information is described that led to this thesis. First, an explanation of offshore wind farm trends and types of wind turbine foundations is given. Then, gravity based foundations are described in more detail by means of an example project. At last, difficulties regarding the mass production and cost reductions of gravity based foundations are analysed, which forms the basis for the proposal of an uncommon launching method for these types of structures.

### 1.2.1 Offshore wind farm trends

With increasing global electricity demand and aims to reduce the impact of global warming and climate change, governments are looking for ways to switch from using fossil fuels to renewable energy. The European Union has set a legally binding goal to generate 27% of the final energy consumption by means of renewables by 2030 (European Wind Energy Association, 2015). Offshore wind farms have been playing an important role in facilitating this energy transition and will continue to do so to achieve this goal. By the end of 2011, the total installed capacity of offshore wind turbines was 3,813 MW (European Wind Energy Association, 2012). End of 2017, a total of 15,780 MW has been installed in Europe and it is expected that the total offshore wind energy capacity will grow towards 25,000 MW by 2020 (WindEurope, 2018). Recent trends have shown that wind farms are moving further offshore, into deeper water, and using larger wind turbines (European Wind Energy Association, 2013). With increased water depth comes increased foundation costs, as can be seen in Figure 1.1.

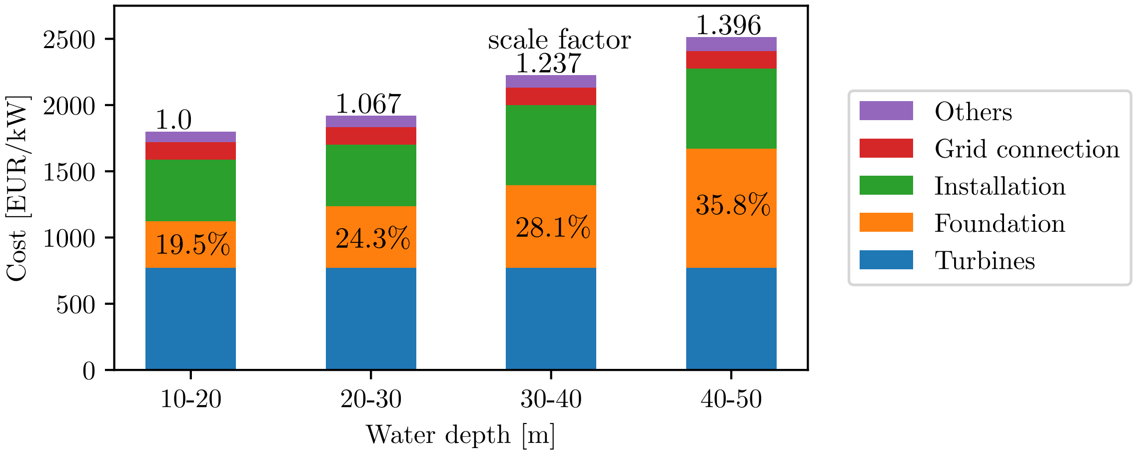

**Figure 1.1:** Offshore wind farm installation cost for increasing water depth. Data is from European Environment Agency (2009, p. 39)

In a water depth of 40-50 m, the foundation cost consist of more than a third of the total wind turbine installation cost. Foundations will therefore become a bigger cost driver for offshore wind farm projects. According to Leanwind (2017, p. 16), a consortium investigating cost reductions in offshore wind funded by the European Union, “the development of wind farms further offshore in deeper water requires advances in both turbine foundation technology and the vessels required to construct and service these wind farms”. Operability of vessels is limited by shorter favourable weather windows due to harsher meteorological conditions. These factors increase the cost of offshore wind farms considerably with regard to foundation solutions, transportation, installation and decommissioning.

### 1.2.2 Types of offshore wind turbine foundations

There are several types of foundations for offshore wind turbines: monopiles, jackets, tripods, tripiles, gravity based foundations (GBF’s) and floating structures. Although the first offshore wind farm (Vindeby, Denmark, 1990) used gravity based support structures, it is not the most common foundation for offshore wind turbines. Monopiles are by far the most popular foundation type, due to the relatively simple manufacturing process and large potential production volumes. As can be seen in Table 1.1, 81.7 % of all offshore wind turbine foundations in Europe are monopiles.

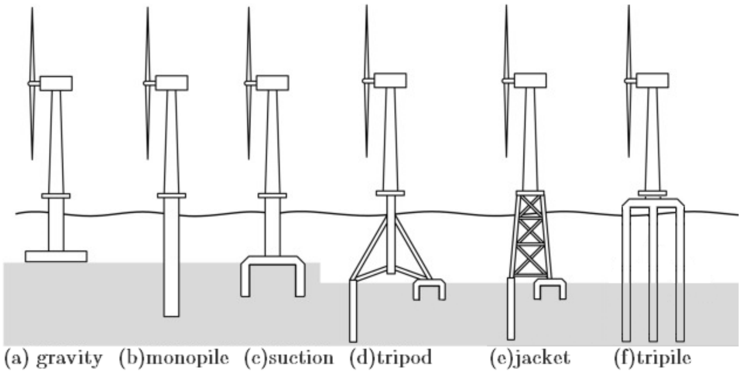

**Figure 1.2:** Grounded offshore wind turbine foundation types. Tripods (d) and jackets (e) can be founded on either suction buckets or piles. The figure is adapted from Oh et al. (2018)

| Foundation type | Number | Percentage |
|---|---|---|
| Monopile | 3720 | 81.7 % |
| Jacket (Piled & Bucket Suction) | 315 | 6.9 % |
| Gravity Based | 283 | 6.2 % |
| Tripod | 132 | 2.9 % |
| Tripile | 80 | 1.8 % |
| Floating | 7 | 0.2 % |
| Other | 18 | 0.4 % |

**Table 1.1:** Foundation types for offshore wind turbines in the North Sea installed up to 2017. Data is from: (WindEurope, 2018).

Following offshore wind market developments, foundations will need to be adapted for deeper water and larger wind turbines. Regarding monopiles, this introduces challenges that are not limited to design and analysis methods, but also to manufacturing, logistics and installation (TNO, n.d.) (Hermans & Peeringa, 2016) (Birkeland, 2016). Monopile size is limited by factory equipment for metal works, crane capacity, and driving limitations. Furthermore, several organisations have expressed concerns regarding the impact of piling noise on marine life (Heinis,

2015) (C. de Jong & Ainslie, 2012). With increased monopile size (diameter and wall thickness), noise levels are also bound to increase (Koschinski & Ludeman, 2011). The heaviest monopile made weighs 1300 tons, is 84 meters long, has a 7.8 meter diameter and supports a 6 MW wind turbine in approximately 40 meters water depth (Garus, 2016). For its installation, worlds largest offshore wind jack-up vessel, SeaJacks Scylla was used, which has a crane lifting capacity of 1500 tons. For monopiles, "cutting and leaving in situ the rest is usually the preferred option (for removal of monopiles)" (Topham & McMillan, 2017). This might become an issue as recent trends in the North Sea regarding decommissioning and removal of offshore structures indicate an increased awareness towards the effect of leaving behind these structures (Koster, 2019).

To facilitate developments in the offshore wind energy market, alternative foundation solutions need to be investigated. Other foundations such as jackets, floating or gravity based foundations could become a preferred alternative for installing large wind turbines in deeper water. Most grounded foundations can be increased in size with regards to design and construction but installation still requires massive lifting operations. This creates opportunity for GBF's that do not require lifting operations while still able to support large wind turbines in deep water.

### 1.2.3 Gravity based foundations

Gravity based foundations are foundations using gravity as the main stabilizing force. Traditionally, GBF's have only been considered for low water depths. Recent scientific articles do not consider the GBF as a suitable foundation in waters deeper than 10 meters, due to the heavy weight and high construction costs (Oh et al., 2018). Recently however, GBF's have been installed in water depths up to 41 meters. This contradiction can be explained by the fact that there are two main types of GBF's for offshore wind turbines: the flat base, open caisson type and the conical type. Flat base, open caisson GBF's are only suitable for shallow water (up to 10 meters) and is widely installed in calm, shallow seas such as the Baltic Sea (Leanwind, 2017). The conical GBF has been used in deeper waters (Energinet.dk, 2015). Most GBF's in Europe, including those at the Vindeby wind farm are flat base, open caisson type as shown in Figure 1.3. The conical GBF as shown in Figure 1.4 and 1.5 is less common, and have been constructed using steel, concrete or a mix of steel and concrete and have been installed in deeper seas such as the North Sea.

**Figure 1.3:** Flat based, open caisson GBF. (Energinet.dk, 2015)

**Figure 1.4:** The concrete conical GBF installed at the Thornton Bank I. (Energinet.dk, 2015)

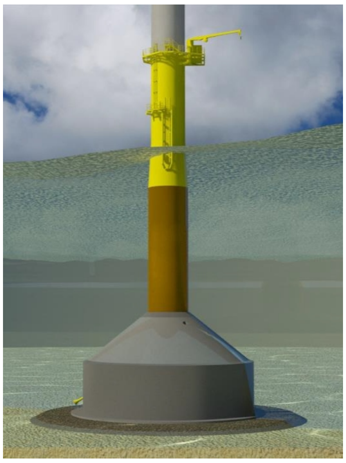

**Figure 1.5:** The concrete and steel conical GBF installed near Blyth. (Ten Oever & Overbeeke, 2017)

Two offshore wind farms in the North Sea use GBF's as wind turbine foundations, Thornton Bank I wind farm in Belgium and Blyth Offshore Demonstrator wind farm in the UK. Both wind farms use a version of the conical GBF. The Thornton Bank I wind farm foundations are made fully of concrete while for Blyth, a steel shaft is fixed into a concrete caisson. Details of both wind farms can be seen in Table 1.2.

**Table 1.2:** Gravity-based wind farms in the North sea. Data is from: (www.4offshore.com, 2019).

| Wind farm | No. of turbines | Turbine capacity [MW] | Depth [m] |
|---|---|---|---|
| Thornton Bank I | 6 | 5 | 18-28 |
| Blyth Offshore | 5 | 8.3 | 36-41 |

### 1.2.4 Blyth Offshore Demonstrator Project

In 2017, the Blyth Offshore Demonstrator project marked a milestone in the development of GBF's for offshore wind turbines. BAM Infraconsult demonstrated the feasibility of the GBF for large turbines in deep water. For this project, 5 GBF's were constructed and installed in a water depth of up to 41 meters below the lowest astronomical tide [LAT]. The GBF's support an 8.3 megawatt (MW) wind turbine generator with a rotor diameter of 164 meters and hub height of LAT +110 m. The complete structure, from base to blade tip when standing upright, is over 230 meters. This project proved that gravity based foundations are not just suitable for shallow water but also for deep water, while supporting the largest wind turbine generator at that time. A combination of this water depth and wind turbine capacity has not yet been accomplished using monopile foundations. This was also the first offshore wind farm that used the float and submerge technology (EDF, 2018).

The Blyth GBF has a significant advantage. In contrast to most other grounded offshore wind turbine foundations, it is buoyant. Consequently, installation does not require expensive heavy-lift or jack-up vessels with high crane capacity as the GBF floats and can be towed offshore using standard tugs. In addition, piling the seabed is avoided since the GBF's are immersed and ballasted by water and sand. This reduction in costly marine operations significantly reduces installation cost.

Regarding the installation phase, enlarging the GBF does not introduce new challenges as it does for monopiles or other bottom founded structures. The installation method and equipment is independent of foundation size, making this type of foundation easily scalable and more future-proof. The self-buoyant GBF also provides a massive advantage in decommissioning. After removal of the wind turbine and tower, ballast can be removed from the GBF and it can be floated and towed away. This creates new opportunities for reusability or recycling of materials.

#### Geometry

In the original design, the base slab has a diameter of 30.5 meters and a thickness of 1.1 meters. On top of the base slab, 9 meter high vertical walls supports a cone roof. Total height of the foundation is 60 meters, which includes the concrete caisson and a part of the steel shaft. the GBF geometry is also shown in Figure 1.6.

#### Construction method

The GBF's for the Blyth Offshore wind farm were constructed in a dry-dock in the Port of Blyth. This is not favourable for larger wind farm projects due to delay caused by filling and emptying

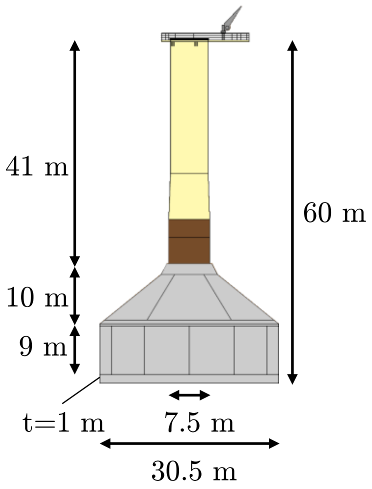

**Figure 1.6:** Approximate geometry of the GBF as constructed for the Blyth Offshore wind farm. This geometry will be used in this research.

the dry dock and high rental costs. Also, construction is slowed due to space limitations and only a few units can be constructed simultaneously. As previously mentioned, BAM aims to construct GBF's at an on-land production site for future wind farm projects.

The construction method applied in Blyth is summarized by pictures in Figure 1.7. The structure consists of a thick base slab on which inner and circular outer walls were cast by slip-form. Six inner walls subdivide the caisson into six compartments. These compartments improve hydrodynamic stability during transport and immersion. After casting the walls, a prefabricated steel shaft was inserted and fixed to the base pate and the six prefab roof elements were placed to form the conical roof. The roof connections were cast and the top of the steel shaft, including the access platform, was welded to the inserted bottom half of the shaft.

### Installation method

As the dry dock was filled with water, the GBF's float and can be towed out. Outside of the dry dock, where the water depth was larger, the GBF was filled with extra ballast concrete to increase the stability during the transport and installation phases. During the floating phase inside the dry-dock, the draft of the structure was approximately 7.5 m and the structure weighed 5500 tonnes. The draft increased to approximately 10 m after filling the GBF with ballast concrete. The 7 000 tonne structure was then towed offshore, where it was ballasted with water as it immersed onto a prepared gravel bed as can be seen in Figure 1.8. When the GBF touched the seabed, it was not yet completely filled with water, hence the pressures inside and outside the concrete caisson were not equivalent. Just before touch down, the GBF resisted a net hydrostatic pressure of 40 meters. After immersion, the water was replaced by sand and the foundations has an immersed (effective) weight of 12 000 tonnes when installed on the seabed. Scour protection was placed and the tower and wind turbine generator were installed. Decommissioning and removal can be done by reversing the above procedure, by flushing out the sand and pumping out the water, causing the GBF to float again.

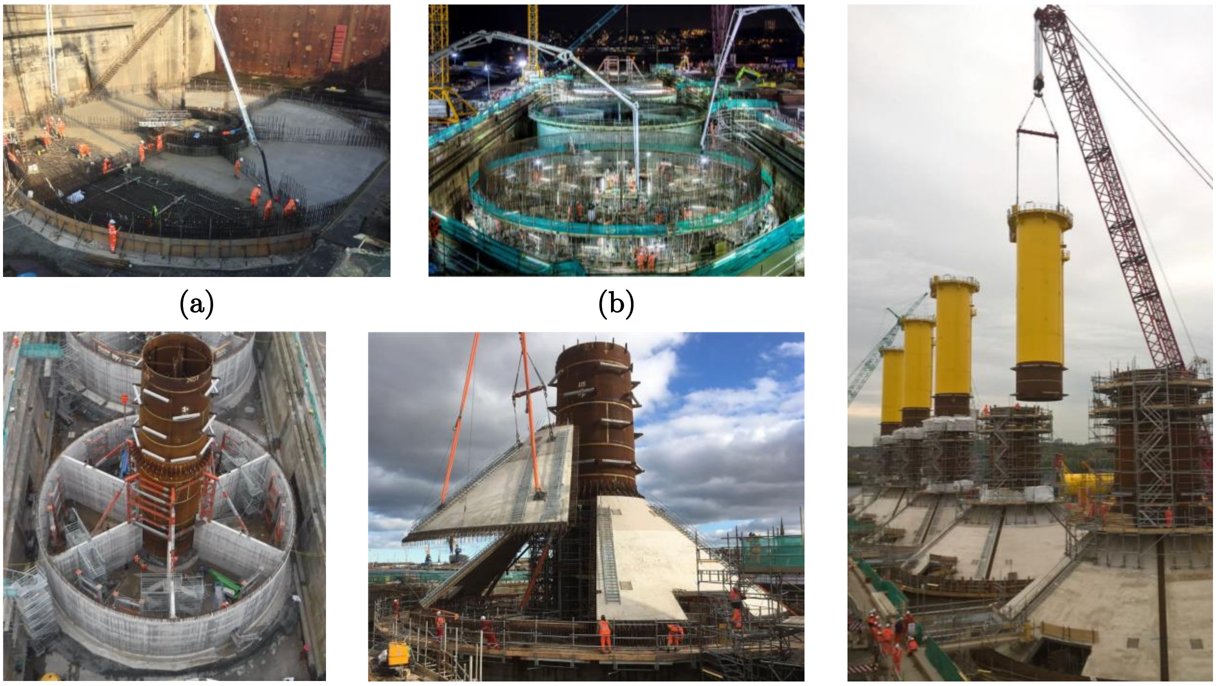

(a) (b) (c) (d) (e)

**Figure 1.7:** Construction phases of the GBF. The base slab (a) was cast in-situ on a gravel bed inside the dry-dock. The outer and internal walls (b) were then cast by slip-form to a height of 8 m. Then, the lower shaft (c) was inserted and fixed to the base slab. The conical roof elements (d) were then lifted and fixed to the outer wall and shaft. Lastly, the upper shaft (e) was welded to the lower shaft in the field. Images from: (Bewell, 2018).

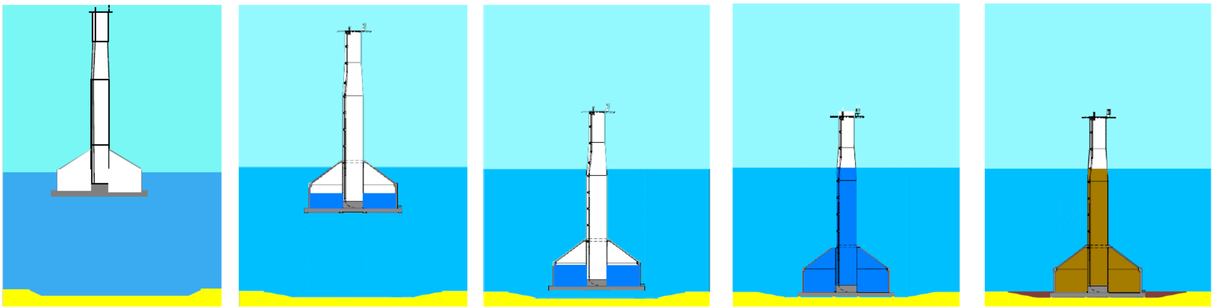

**Figure 1.8:** Offshore installation of the GBF. After arrival, the compartments were filled in a controlled manner, causing the GBF to sink. During this process, 4 tugs accurately kept the GBF in position. After touch-down, the full structure (including the shaft) was filled with water. Then, a vessel pumped a mixture of sand and water into the GBF, replacing the water by sand. When installed, the structure has an effective weight of 12 000 tonnes. Image is from (Bewell, 2018).

## 1.3 Problem analysis and proposal

This section first explains the main challenge related to mass production and cost reduction of GBF's, after which a solution is proposed, which is to gravitationally launch GBF's. Gravitational launches of ships, concrete caissons, and jackets are then described.

### 1.3.1 Problem analysis

Although the feasibility of GBF's for large wind turbines in deep water was demonstrated, there are numerous challenges to overcome when applying this type of foundation for full-sized commercial wind farm projects. To compete in the current offshore wind foundation market, many units will need to be constructed in a short period of time. Also, constructing the GBF is expensive in comparison to the monopile and construction time is long. Mass production and cost reduction are essential for GBF's to become a competitive solution to other offshore wind turbine foundation types. This calls for a further optimization in design, construction and installation. Construction of GBF's in a dry-dock as was done at the Blyth project is not optimal for constructing many units in a short period of time. The problems of using a dry-dock are:

- It is expensive to rent.
- Limited space slows down construction.
- The diameter and draft of the GBF is limited by the dimensions of the dry-dock.
- Only a few (5 in the case of the Blyth project) GBF's can be constructed simultaneously.

**(a)** Aerial view of the construction site at the Port of Blyth. The five GBF's were constructed simultaneously in a dry-dock. Image is from: (www.bam150years.com, n.d.).

**(b)** An on-land construction site for GBF's, more suitable for mass production and offer more flexibility in the construction method and planning. Image is from: (The Construction Index, 2016).

**Figure 1.9:** The previous and proposed construction methods for GBF's for offshore wind turbines.

Tuin (2018) has investigated optimizations to shorten the construction time of GBF's and he has proposed a construction site on land. This is congruent with the aims of BAM Infraconsult for future GBF projects. The plan is to construct an on-land production line as illustrated in Figure 1.9b with a capacity of constructing 1 GBF per week. In the application of this method, transporting the GBF from land into water (launching) is one of the challenges. The main advantage of self-buoyant GBF's for offshore wind turbines is that heavy lift, jack-up or semi-submersible vessels are not required. Combining this with an on-land construction site calls for a way to 'launch' the GBF's from land into water without using special vessels. Due to the large weight of the GBF, it cannot be easily lifted by an on-land crane. According to Tuin, the best solution is to use a semi-submersible vessel although he realises that this is very expensive. Taking into account the production of 1 GBF per week for a standard size wind farm of 50 turbine foundations, production would take 1 year (Muttray, 2019). Rental costs of heavy-lift semi-submersible vessels range from 60,000 - 100,000 USD per day, averaging to over 29 million USD for 1 year (De Jong, 2010). Alternatively, he suggested the construction of an immersion structure, which costs even more but can be reused. Tuin focused on optimizations of GBF construction at one specific site: Oostende harbour.

### 1.3.2 Proposal

The suggested optimal launching techniques require a special vessel or immersion structure, increasing cost, complexity, and dependency on availability of special vessels. Alternatively, gravitational launching methods could be applied. A gravitational launching is the process of transporting a structure from land into water on an inclined slipway using gravity as the main driving force. This technique uses an inclined surface on which a floating structure can travel freely into the water (unrestricted). Intuitively, gravitational launching methods are low-cost if they can be applied without substantial structural modifications to either the GBF structure or port infrastructure. Gravitational launches are common in the shipping industry, but have not been applied often to large concrete structures such as caissons. The sections below summarize different types of gravitational launches that have been applied to launch ships, caissons, and jacket foundations.

#### End launch of a ship

On an inclined slipway, ships are constructed fully above water and slid into the water upon completion. This method, illustrated in Figure 1.10 is referred to as an end launch, although this method can also be applied in transverse direction making it a side launch. When the ship is finished, its weight is transferred from building blocks onto cradles on the greased sliding ways. A slipway might consist on one, two or up to four ways, depending on ship weight and size. When the blocks are knocked away, gravity pulls the ship on the cradles along the sliding ways into the water. As the stern becomes more and more buoyant, the ship is lifted as it pivots around the bow, which still has contact with the sliding ways. The ship then floats freely and is slowed by tugs, dragging lines or anchors to prevent it from drifting afar.

Slipway dimensions differ greatly but typically, declivity is 1 in 20 and with a length of 300 meters (Tupper & Rawson, 2001). Loads on the vessel can be estimated by setting up a moment balance around the pivot point at several time intervals. Dynamic effects are neglected, making the approach quasi-static. This produces a so-called "launching curve", displaying moments and forces as the ship travels down the slipway. For more information, see Chapter 8 in Tupper and Rawson (2001).

**Figure 1.10:** End launch of a ship. Image is from: (GS Yard, 2010).

**Figure 1.11:** Side launch of a ship. Image is from: (Slater, 2016).

Sometimes, the slipway does not extend far into the water. Although partially submerged, the stern will become a sort of cantilever, imposing a large moment and concentrated load on the hull. For very short slipways, the ship might even tip over the end of the slipway. The bow will be lifted off the ways and the large concentrated load will definitely damage the ship. Sliding ways often have a camber, causing the stern to enter the water more steeply, increasing buoyancy. This will prevent tipping but increases loads on the bow.

### Side launch of a ship

A side launch is often applied in areas with limited space, such as narrow rivers or canals using a slipway that ends above the water surface, as shown in Figure 1.11 (Bruce & Eyres, 2012). The ship tips over the end of the slipway and plunges into the water. During this launching process, the ship hits the water violently and could roll thirty degrees or more. Therefore, the ship should have great strength and stability. The declination of the way is often in the order of 1 to 8 to ensure the ship falls clear of the quay (Tupper & Rawson, 2001).

This launching process is dynamic and simulating dynamic behaviour and structure-water interaction requires numerical methods and CFD programs. Motions and velocities during the sliding and tipping phase can be derived from equations of motions. Ye (1994) has simplified the six degree-of-freedom system to three degree-of-freedoms, and proposed a numerical method to find a solution. Many studies have looked into these equations as it defines the input parameters for the CFD model that determines wave impact loads and the hydrodynamic behaviour (Hak, 2005) (Fitriadhy & Malek, 2017). These studies use commercial CFD programs such as Comflo or Flow-3D to simulate the hydrodynamics of the launching process.

There are certain aspects that can go wrong during a sideways launch, listed below (Schaaf & Sas, 2013):

- Insufficient water depth.
- Insufficient speed, structure hits quay after tilting back.
- Insufficient stability, the rotation is not damped enough so the structure capsizes.
- Structure slams the water flat, overloading the base plate.
- Quay wall is not strong enough to resist the loads.

Ships are often constructed on top of the launching ways but the GBF's are to be constructed elsewhere and will be transported to the launching structure. This is the main difference when these launching methods are applied to GBF's. This launching method has not yet been applied on concrete structures. Probably, concrete caissons are usually not strong enough to resist the large impact and tipping forces.

### Launching a concrete caisson

Gravitational launching methods have been applied on concrete structures in the past, mainly on caissons. As early as 1901, the caissons for the Quebec Bridge were constructed on a timber launching ways and launched into the river as can be seen in Figure 1.12. The declivity of the slipway is often very low to decrease launching velocities. Concrete structures are often lowered mechanically using winches to further decrease velocities. This more controlled way of launching is suitable for concrete caissons because the velocities and loads are less severe. In more recent times, caissons have been launched on tracks (see Figure 1.13) or launching airbags.

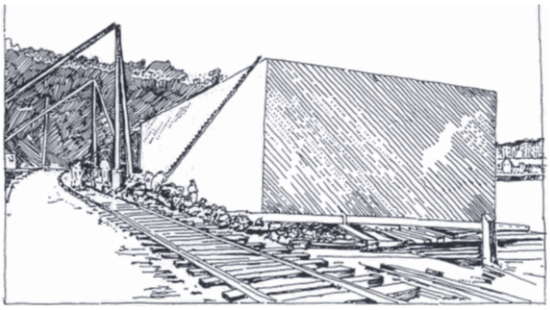

**Figure 1.12:** Slipway launch of a caisson in transverse direction. Drawing by Werner K. Sensbach from an illustration in the July 20 1901, *Le Soleil* of Québec.

**Figure 1.13:** A caisson is lowered into the water on an inclined slipway equipped with rails. The motion is restricted by cables and winches. Image is from: (YouTube, 2017).

### Jacket launch

Jackets for offshore purposes are sometimes launched using a barge. Constructed horizontally onshore, the jackets are transported on a barge equipped with skid rails (skid beams) which are lined with Telfon. Upon reaching its destination, the barge is ballasted until it reaches the required trim and draft at which the jackets starts sliding due to gravity.

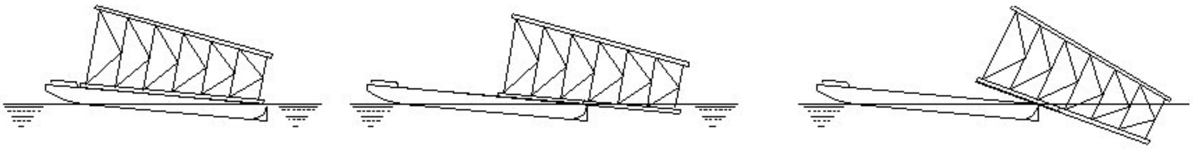

**Figure 1.14:** Launching procedure of a jacket launch. After reaching the required trimming angle, the jacket starts sliding into the water. As soon as the center of gravity passes over the edge of the barge (pivot of the rocker arm), the jacket starts rotating into the water. Image is from: (ESDEP, n.d.).

The ends of the skid rails are often equipped with rocker arms or tilting beams to avoid large point loads on the skid rails or launching cradles as the jacket rotates and launches into the water. Jackets of over 50,000 tonnes have been launched using this method.

**Figure 1.15:** Rocker arm on a barge used to distribute tipping loads when launching jackets. Image is from: (ombugge, 2016).

**Figure 1.16:** Largest jacket every launched using a barge, the Bullwinkle jacket by Shell in 1989 which was over 500m long and weighed over 50,000 tons. Image is from: (ESA, 2011).

## 1.4 Launching a GBF

A gravitational launch was proposed to move the GBF from the on-land construction site into the water. Based on a literature study, this launching method is not commonly applied to concrete structures due to limited strength and stability. The GBF is a concrete structure that naturally resist extreme loads and might be suitable for this launching technique. The GBF was designed to resist large moment and axial forces. During the immersion phase, resists more than 40 m of hydrostatic water pressure. The base slab is 1.1 meters thick and has a high reinforcement ratio, giving the structure great strength. Due to its low center of gravity, it is self-righting, which means that when placed horizontally in the water, it returns to its upright position.

In this section, a gravitational launch of a GBF is looked at in more detail to examine the process in more detail. Then different slipway geometries are presented and an analysis is made of the requirements for a launch.

### 1.4.1 Process analysis

The launch is the activity that connects two phases of the complete GBF production process: (1) the GBF arrives at the waterside on a horizontal surface and (2) the GBF floats in the water at rest. This is illustrated in Figure 1.17. The function of a gravitational launch is therefore to move the GBF from its position on land to the water.

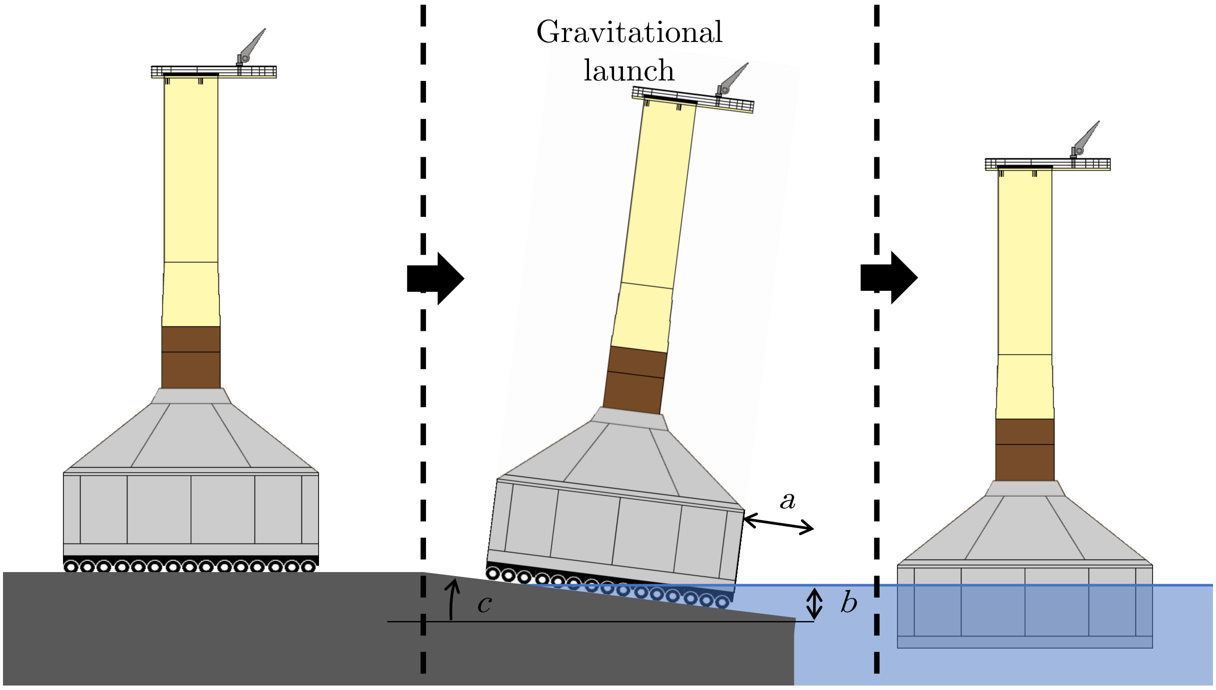

**Figure 1.17:** The gravitational launch is an activity between the GBF travelling horizontally on the quay wall and it floating at rest in the water. The slipway can have varying length (a), freeboard height (b) and inclination (c).

There are several activities that take place when launching a GBF gravitationally, which are listed below.

1. The GBF arrives from the end of the production line on a horizontal surface.
2. The GBF is transferred onto the inclined slipway

3. The GBF is released and it starts moving.
4. The GBF moves on the slipway.
5. The GBF is transferred into the water.
6. The GBF moves in the water with certain motions induced by the launching process.
7. The motions are controlled until the GBF floats at rest in the port.

As will be mentioned in the scope in Section 2.3, only the dynamics of the GBF during a launch are modelled in this thesis. With respect to the above activities, this regards steps 3-6. These steps are looked at in more detail below.

### 1.4.2 Slipway ending

The ending of the slipway can take different shapes and has a large impact on the dynamics of the GBF. The launching physics depend mainly three slipway properties: (a) the length of the slipway, i.e. the distance the GBF travels to the water, (b) the height of the edge with respect to the water level (freeboard height), and (c) the inclination of the slipway. These properties are clarified in Figure 1.17. Different examples of slipway endings are illustrated in Figure 1.18. There are two main variants, the first of which has a slipway extending indefinitely into the water (until the GBF floats), shown in Figure 1.18a. The other has an abrupt slipway ending. In that case, the GBF will slide off the slipway, tip over and fall over the edge of the slipway, plunging violently into the water. The slipway can end above or below the water, shown in Figure 1.18b and Figure 1.18c respectively.

**Alternative A: Fully submerged slipway end**
A fully submerged slipway, as illustrated in Figure 1.18a, will allow the GBF to move into the water until it floats. Although the motion is not restricted, the GBF can be launched in a very controlled manner by giving the slipway a small inclination which results in a small launching velocity. This method is similar to the launching method applied on concrete structures in the past, only without restrictions.

**Alternative B: Dry slipway end**
Similar to a sideways ship launch, the slipway can abruptly end above the water surface. In this case, no slipway section is submerged and therefore the complete slipway is dry. When the center of gravity passes over the edge of the slipway, the GBF will tilt and fall off the slipway. It will then plunge violently in the water.

**Alternative C: Partially submerged slipway end**
As illustrated in Figure 1.18c, the slipway can be partially submerged. This is similar to the launching method applied in jacket launches. When the GBF reaches the end of the slipway, it will start tilting while the bottom is already partially submerged. This variant is an intermediate variant between the two other variants.

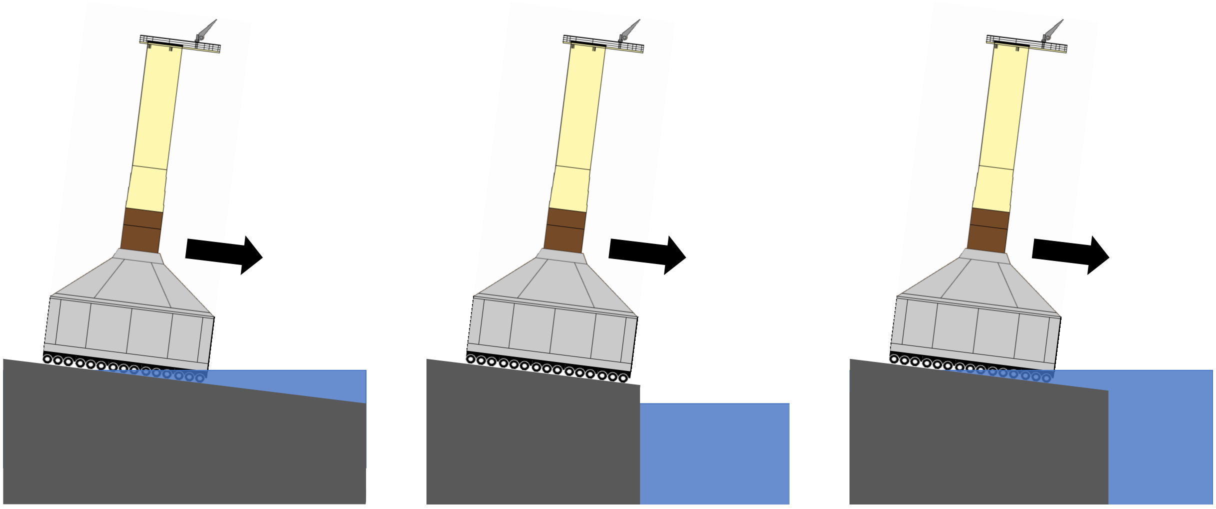

**(a)** A fully submerged slipway end. The slipway extends far into the water and the GBF is gradually slowed down by the increasing water column until it becomes buoyant.

**(b)** A dry slipway end. The slipway ends above the water line. The GBF will fall off the slipway and drop into the water. This method is similar to a sideways ship launch.

**(c)** A partially submerged slipway end. The slipway ends below the water surface but does not extend far into the water, the GBF will tip over the slipway end while partially submerged.

**Figure 1.18:** Different slipway endings that can be applied a gravitational launch.

More focus is to be placed on the variants with an abruptly ending slipway because the slipway with an infinite ending is not considered to be interesting, although it might be (financially) feasible. With a draft of 10 meters, and realistic slipway inclinations ranging from 5 to 20 degrees, the slipway length is 114 to 30 meters, all underwater, which is very expensive to construct. Furthermore, it is assumed that these launches will *always* be possible because similarly to ship end launches, winches can be used as a restriction to reduce the GBF velocity. Therefore, this variant is regarded as less interesting and will therefore only be modelled using a force balance, but not regarded in the final analysis or discussions.

### 1.4.3 Launch requirements

Based on the background information, relevant requirements regarding gravitational launches for GBF's specifically are presented. To determine the success of a gravitational launch, there are several aspects that should be taken into account, which are listed below. This list is partly based on Schaaf and Sas (2013). The GBF has sufficient stability and is self-righting, so stability is not an issue for this specific structure.

- The GBF does not sustain damage during any phase of the launching process. The GBF should be able to resist all loads during all phases of the launching process. Some of the main loads include: the point load on the GBF base during tipping, the moment on the shaft due to rotations and hydrodynamic pressures due to plunging.
- During the launch, the GBF follows a safe trajectory with adequate bottom clearance and the GBF should not hit the quay when it returns upright.
- The maximum draft of the GBF should be small since the launch will occur inside a port with limited water depth.
- The generated wave should have a limited impact on the surroundings.
- The maximum angle of inclination (rotation) should be kept small.

All critical aspects listed above can be related to GBF motions, or kinematics. When the GBF motions are known, loads on the GBF or slipway and other parameters such as the radiation wave or GBF trajectory can be determined. Models describing the transient behaviour of a GBF during a launch need to take into account all main acting forces. Based on Newton's second law, a balance of these forces can be solved and motions can be derived using kinematic equations. There are several mathematical models that can be used to do this, including a simple force balance or a set of equations of motions. Other than mathematical models, physical models can also be used to determine the kinematics of a GBF subject to a launch. Finally, a more recent modelling approach (at least compared to classical kinematics) can be used to solve the kinematic equations with a lot more detail using computer software known as Computational Fluid Dynamics (CFD).

## 1.5 Concluding remarks

This chapter presented the motivation and background of this thesis. Offshore wind farm trends indicate a shift towards larger turbine sizes and deeper water. Gravity based foundations have been applied for large turbines in deep water, but there are clear constructional limitations. In overcoming these limitations, GBF's are to be constructed on land which calls for an efficient method to 'launch' a GBF. Gravitational launches have been applied to steel ships and jacket structures but application for concrete caissons is rare. The GBF is very suitable for this kind of launching due to its large strength and stability. The idea to use gravitational launching techniques is proposed. For a feasibility study, a conceptual design is required. To make a conceptual design, the launching process is to be modelled, which is the main focus of this thesis. In the next chapter, the research approach is given, in which the main problem is stated along with the objective, scope and methodology. A reading guide for the report can be found at the end of the next chapter.

# Chapter 2

# Research approach

Based on the problem analysis and proposal in the previous chapter, this chapter presents the main problem statement, objective and scope for this research. The main research question is divided into sub-questions and a reading guide is presented to explain the structure of this report.

## 2.1 Problem statement

Based on the background information and prolem analysis, the main problem was formed:

**Traditional techniques for launching gravity based foundations for offshore wind turbines might be unnecessarily expensive. Low-cost gravitational launching methods have potential, but it is unknown whether they can be applied to GBF's.**

## 2.2 Objective

The goal of this thesis is to develop models that can be used in a conceptual design phase to easily determine the optimal shape and dimension of the slipway used to gravitationally launch GBF's. These models should describe the process sufficiently so that the launching requirements can be checked. Also, the aim is to make models that are quickly able to compare different slipway geometries and determine which is most favourable in terms of GBF dynamics. In order to model the process, the process must be understood so more insight into the dynamic behaviour of the GBF falling into and floating in the water is also to be developed.

## 2.3 Scope

This thesis will merely focus on the dynamics of a gravitational launch of gravity based foundations for offshore wind turbines as designed by BAM for the Blyth Offshore Demonstrator Project. More information on this project was given in Section 1.2.4. Several key features of the structure relevant for this research are listed below. The structures are:

1. large, the maximum draft is an important design parameter;
2. heavy, lifting with an on-land crane is not possible and loads on the structure and quay are substantial;
3. narrow, the width is small compared to height, affecting the hydrodynamic stability;
4. circular; significant 3-D effects

5. concrete;
6. floating;
7. self-righting; and
8. built on land and to be installed offshore.

The outcome of this research is not necessarily limited to the GBF as designed by BAM but might also be valid for other structures with similar features. Several activities surrounding the launch, such as moving the GBF from a horizontal to an inclined surface or 'picking-up' the GBF after the launch are not part of this research.

This thesis will only focus on the dynamic behaviour of the GBF itself. Analysing aspects that determine whether or not a launch is successful, such as the size of the generated wave, hydrodynamic pressures on the GBF, or the maximum depth reached during a launch is beyond the scope of this thesis. However, the goal is to create models that can be used to help estimate these aspects. A more detailed analysis of the launching requirements was presented in Section 1.4.3.

For the purpose of making a conceptual design, this thesis firstly focuses on simple mathematical models, which are defined as analytical or numerical models that can be solved instantly by hand or computer. For example, empirical formulas or equations of motion (that can be solved numerically using a computer) are considered simple mathematical models, but a full-scale Computational Fluid Dynamics program that takes hours, days or weeks to set up and calculate a solution is not considered 'simple'. Nonetheless, a CFD modelling strategy was also made to explore this modelling method and verify whether or not is it applicable in the conceptual design phase.

## 2.4 Research questions and methodology

Based on the above problem statement, objective, and scope, the main research question is:

**How can gravitational launches of gravity based foundations for offshore wind turbines for the Blyth Offshore Demonstrator Project by BAM be modelled using mathematical models?**

To arrive at an answer of the main research question, the main research question was split up into several sub-questions. Each sub-question is answered in the respective chapter and the method to obtain the answer is described below.

- Chapter 3: Which simple mathematical approaches can be used to describe the kinematics (motions) of a GBF during a launch?
    - For each phase of the launching process, mathematical models were derived that describe the motions of a GBF.
- Chapter 4 & 5: How do the mathematical models compare to reality?
    - Physical models were performed and used to calibrate and validate the mathematical models. The physical model set-up is described in Chapter 4 and the results are analysed and compared in Chapter 5.
- Chapter 6: Can a CFD model be used to model the launching process?
    - A CFD modelling strategy was proposed and used to compare to the physical models.

## 2.5 Reading guide

Chapter 1 presented the motivation of this thesis, contained background information and a problem analysis. The chapter was based on market demand, a literature review, and the Blyth Offshore Demonstrator project. The current chapter defines the main problem, objective and methodology of this research. In Chapter 3, mathematical models are presented for each discrete phase within a launch. Equations of motion and force balances are formulated and hydrodynamic components are determined analytically and numerically. The experiment set up for the tests that are used to calibrate and verify the mathematical models are described in Chapter 4. In Chapter 5, the mathematical models are calibration and validated using the scale model tests. Chapter 6 presents the CFD modelling strategy and compares results to the physical model tests. Chapter 7 concludes this thesis with a discussion, answers to the research question and recommendations design purposes and future research. References are made to the appendices to investigate unknowns, perform calculations, and present background or theoretical knowledge on the software used. Figure 2.1 shows the report structure in a flow chart.

**Figure 2.1:** A flowchart of the structure of this document with chapters and appendices.

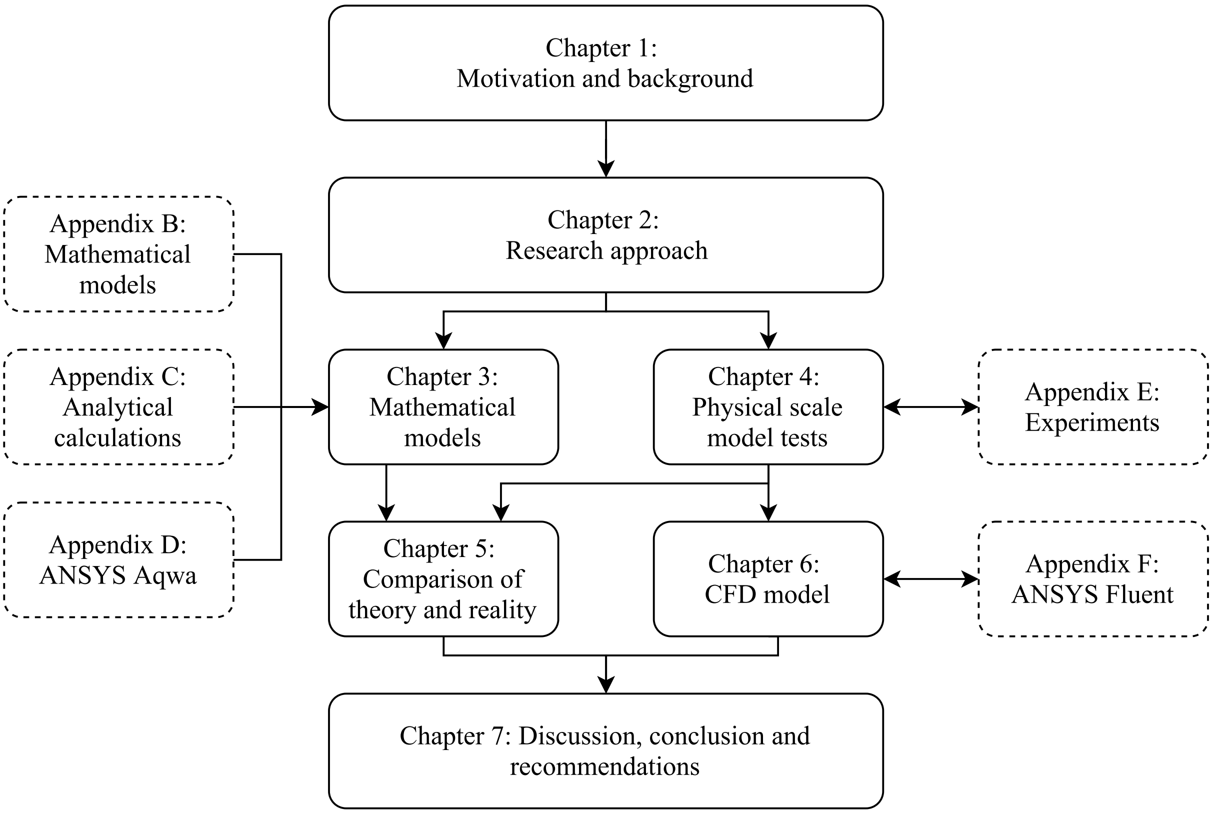

## 2.6 Software programs

Numerous software programs were used for this thesis. Python was used in a Spyder environment to construct graphs, for the video analysis in the physical scale model tests, to solve the force balances, and for curve fitting. Microsoft Powerpoint was used to draw diagrams and figures. Maple was used to solve the equations of motion and other mathematics. ANSYS Aqwa was used to calculate hydrodynamic coefficients and ANSYS Fluent was used for the CFD analysis. LaTeX was used in Overleaf to construct this report with Mendeley as a reference manager.

# Chapter 3

# Mathematical models

In this chapter, the dynamic response of the GBF to a gravitational launch is modelled using simple mathematical models. The aim of this chapter is to answer: "Which simple mathematical approaches can be used to describe the GBF motion during each phase of a gravitational launch?". This chapter starts by explaining the different phases of a gravitational launch and describing the mathematical model used for each phase. After stating some general simplifications, axis conventions and notations used in this thesis, mathematical models used to analyse different phases of the launching process are presented. The models will be explained in chronological order in which they occur during a launch. Software programs such as Maple or Python were used to solve the mathematical models, the input of which is shown in Appendix B.

## 3.1 Phases of gravitational launches

In short, there are 4 main phases that occur during the launch: sliding, tipping, plunging and floating. Depending on the slipway geometry, sliding and tipping can take place above, below or partially below the water line. These are the processes that were modelled to model the complete launch. For each of the slipway endings stated above, the distribution of the phases is shown in Figure 3.2, 3.3 and 3.1. For some phases, such as the GBF sliding over the slipway, a force balance was be used while for others, such as the GBF tipping over the edge or floating freely in the water, equations of motion were used. In addition to the models shown, a CFD model was used in Chapter 6 for the 'floating' phase of the launch.

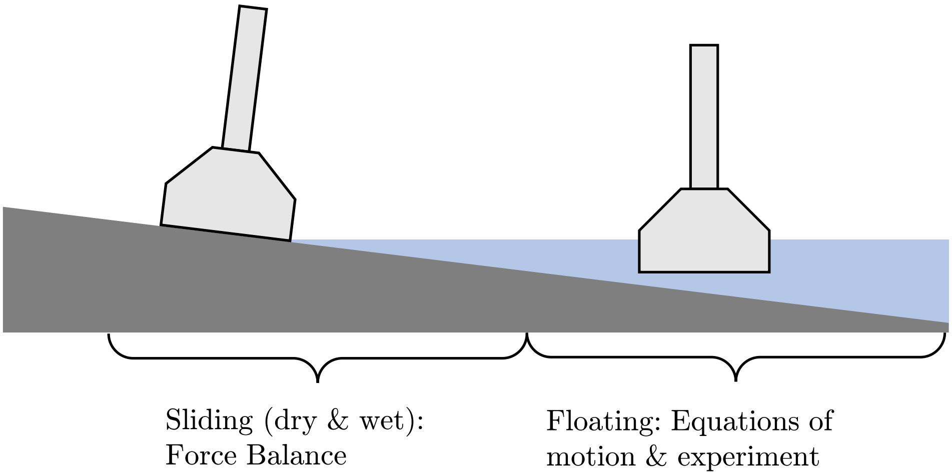

**Figure 3.1:** Phases in a launch where the slipway ends after the GBF starts to float. Two main phases are be distinguished and modelled: (1) sliding Section 3.3 and (2) floating.

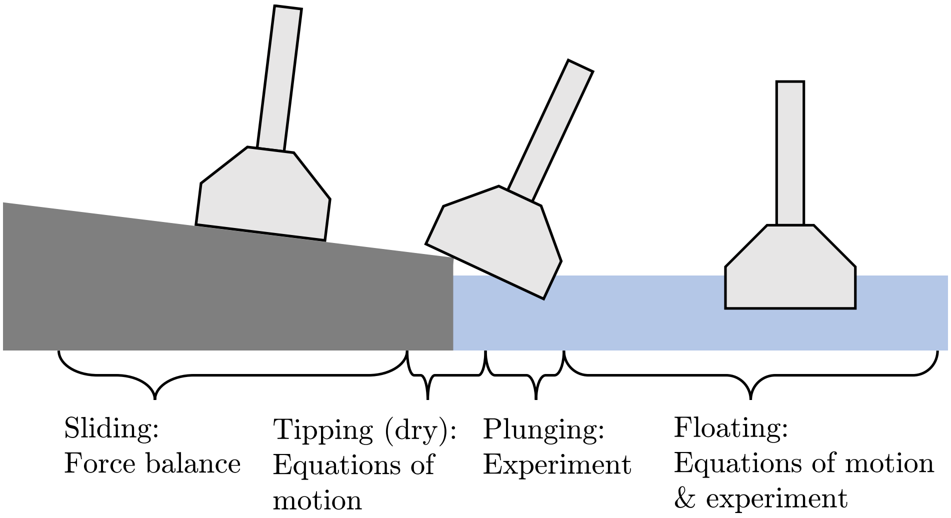

**Figure 3.2:** Phases of a launch for a slipway ending above the water surface. Four main phases were distinguished and modelled: (1) sliding in Section 3.3, (2) tipping in Section 3.4, (3) plunging using experiments in Chapter 5 and (4) floating in Section 3.5.

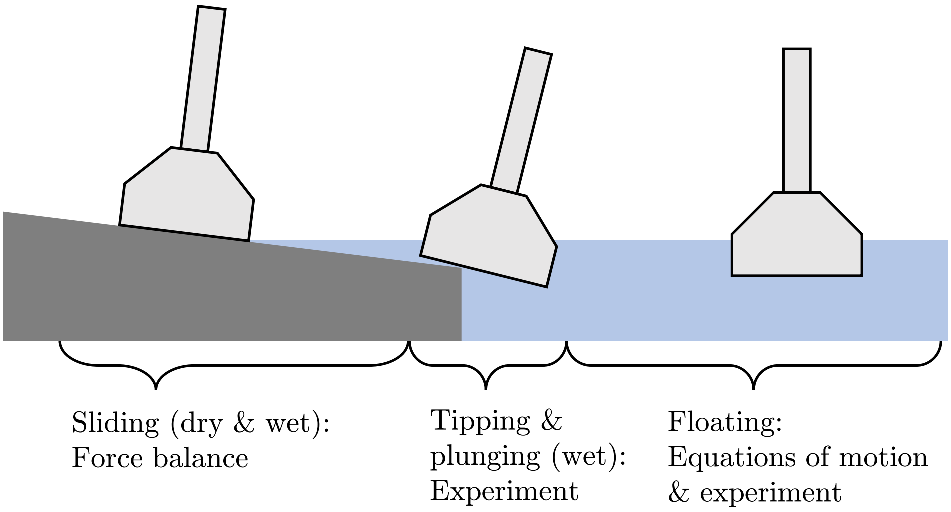

**Figure 3.3:** Phases of a launch in which the slipway ends below the water surface. Three main phases were distinguished and modelled: (1) sliding in Section 3.3, (2) tipping and plunging, now occurring at the same time in Chapter 5 and (3) floating in Section 3.5.

As described at the end of Section 1.4.2, the submerged slipway variant illustrated in Figure 3.1 was modelled, but not analysed in detail or compared to physical models because this variant is of less interest due to a considerably higher construction cost and large required harbour space. In addition, this variant was assumed to *always* be technically feasible because GBF motions can be restricted by means of winches.

## 3.2 General notations and simplifications

Certain notations and simplifications help to explain and simplify the problem. Notations and simplifications used in this thesis are explained below.

### 3.2.1 General notations

To describe the motion of a rigid body in a three dimensional space, six degrees of freedom are to be considered, three in translation and three in rotation, visualised in Figure 3.4.

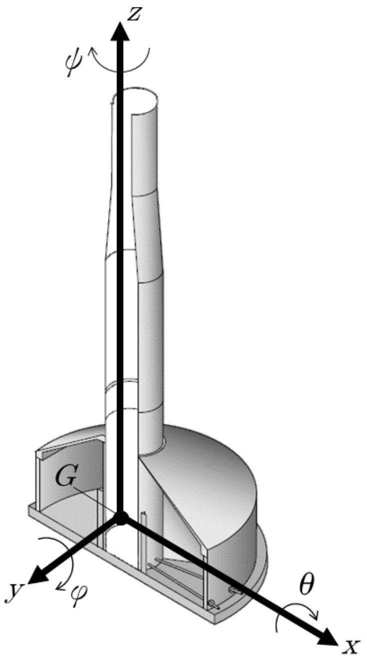

**Figure 3.4:** Directions of the $x$, $y$, $z$, $\theta$, $\varphi$, and $\psi$ axes in 3D.

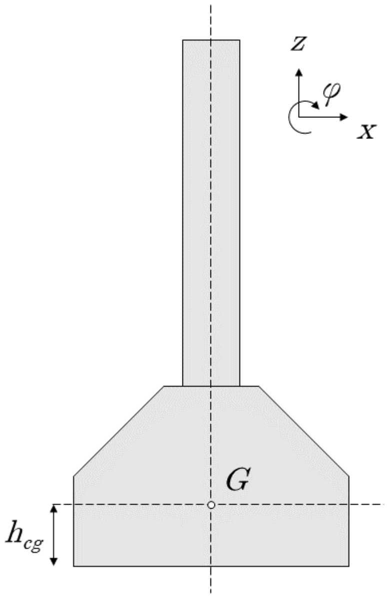

**Figure 3.5:** The center of gravity of the GBF, $G$. The height of the center of gravity, $h_{cg}$, measured from the base is equal to 6.54 m

The motions of floating structures are defined by:

- the translation of the center of gravity (G) in the direction of the $x$-, $y$-, and $z$-axes:
  - surge in the $x$-direction,
  - sway in the $y$-direction,
  - heave in the $z$-direction.
- the rotations about the axes:
  - roll about the $x$-axis, positive clockwise,
  - pitch about the $y$-axis, positive clockwise,
  - yaw about the $z$-axis, positive clockwise.

Since motions will mainly occur in a two dimensional plane (the $z, x$-plane) and the GBF is symmetric in the $x$- and $y$-direction, the problem is reduced to three degrees of freedom. The position, motion and acceleration of the GBF can therefore be described using three directions: translation in $x$- and $z$-direction and rotation around $y$-axis, $\varphi$, as visualised in Figure 3.5. The $z$-direction is defined straight upwards, the $x$-direction is to the right and the $\varphi$ rotation is clockwise around the $y$-axis. The rotation of the GBF is always measured as the centerline of the GBF with respect to the vertical $z$-axis. The origin of the coordinate system will depend on the phase of the launching process, but will often be taken as the initial position of the GBF on the slipway. The position, velocity and acceleration refer to the center of gravity, $G$. These definitions are visualized in Figure 3.5.

Velocities will be denoted by its direction with an over-dot i.e. $\dot{x}$ for horizontal velocity, $\dot{z}$ for vertical velocity and $\dot{\varphi}$ for rotational velocity around the $y$-axis. The same holds for accelerations, using a double over-dot i.e. $\ddot{x}$ for horizontal accelerations. The notation $v$ or $a$ is used in some cases to clarify the process by indicating the prevailing motion direction of the velocity or acceleration respectively.

Physical scale model tests were conducted in a 1:100 scale. To be able to make comparisons, some calculations were performed at the 1:100 scale, or were scaled to the 1:100 scale. These calculations can easily be done at a different by adjusting the input variables. Whenever results are presented or comparisons are made, the scale at which these calculations were made is mentioned.

### 3.2.2 Simplifications

To simplify the models in general:

- aerodynamic forces are ignored,
- the friction coefficient between the GBF and slipway is 0.1 and constant,
- and the GBF moves freely in the water, i.e. there are no external (wave) forces.

Simplifications and limitations of the software used to numerically determine the hydrodynamic components are presented in the respective section or chapter describing the software.
Some widely used symbols and value include:

$\rho = 1000$ = mass density of the fluid [kg/m$^3$]
$g = 9.81$ = gravity [m/s$^2$]

Although the GBF is ultimately to be launched in sea water, $\rho = 1000\ kg/m^3$ was used since a comparison was made to the physical scale model tests, which are performed in fresh water. The friction coefficient $\mu_c$ was used as the friction between the slipway and the GBF during the sliding phase as well as during the tipping phase.

**Transport system**

To facilitate the transport of the GBF over the slipway, a transportation system is required. The transportation system enables the GBF to move over the slipway. The system impacts the dynamics of the GBF because it determines the coefficient of friction. There are various heavy transportation systems that could be used to transport the GBF over the slipway. Different options are analysed in Appendix A.

The method that was chosen is to use a set of steel skidding beams and tracks that are lined with Polytetrafluoroethylene (PTFE), or more commonly known by its brand name: Teflon. This is the same sliding mechanism used to launch jacket structures. The coefficient of friction between this material and stainless steel depends on many aspects such as: temperature and pressure. Common values range between 0.01 and 0.1. More information can be found in Appendix A. A coefficient of friction $\mu_c$ of 0.05 was initially used in the mathematical models in this thesis. However, such small friction coefficient could not be obtained during the scale model tests, so a friction coefficient of 0.10 was used in all analyses. This is further explained in Section 4.2.3.

**GBF properties**

In the analysis of the motions, GBF properties are required. In addition to geometric properties given in 1.2.4, a summary of additional properties relevant for the dynamic response is given in Table 3.1. These numbers are approximated based on BAM project reports. The height of the center of gravity is measured from the base of the GBF, as illustrated in Figure 3.5. The draft of a floating GBF was calculated by dividing the mass by the base plate surface area and the density of water ($\rho$).

**Table 3.1:** Properties of the GBF relevant for the dynamic response analysis.

| Name | Symbol | Value | Unit |
|---|---|---|---|
| Moment of inertia pitch | $I_y$ | 1 500 000 | ton m$^2$ |
| Mass | $m$ | 7000 | ton |
| Radius of base plate | $R$ | 15.25 | m |
| Draft | $d$ | 9.58 | m |
| Height of the center of gravity | $h_{cg}$ | 6.54 | m |
| Metacentric height | $\overline{GM}$ | 4.27 | m |

## 3.3 Sliding: force balance

A force balance was used to model the less complicated processes. The first phase of every slipway variant consists of the GBF sliding over the slipway with or without the presence of water. A simple force balance was solved, which results in an acceleration of the GBF in time in the direction of the slipway. The force balance without the presence of water is presented first, after which water is introduced and buoyancy and drag forces are calculated.
The main forces are illustrated in Figure 3.6, in which:

$M$ = weight of the GBF acting along the z-axis
$N$ = normal force on the launching ways/GBF perpendicular to the slipway
$W$ = frictional force on the launching ways/GBF parallel to the slipway
$F$ = resulting force parallel to the launching ways, causing the GBF to accelerate

The weight of the GBF, $M = m\,g$ in which $m$ is the mass of the GBF and $g$ the gravitational constant. During this phase of the launching process, the frictional force $W = \mu_c\,N$. The normal force $N = M\,cos(\alpha)$. Setting up a force balance in the direction of the slipway results in:

$$F = M\,sin(\alpha) - W. \tag{3.1}$$

Using Newton's second law of motion, $F = ma$, the acceleration of the GBF on the slipway, $a = F/m$. Simplifying this equation results in the following acceleration along the slipway:

$$a_{dry} = g\,sin(\alpha) - \mu_c\,g\,cos(\alpha) \tag{3.2}$$

The acceleration can be used to calculate the velocity and position of the GBF at any moment. The velocity and rotation of the GBF are the two parameters that will be input for the analysis of the next phase. Three parameters in this phase influence the velocity, $v$ of the GBF when it reaches the end of the slipway: the friction coefficient, length, and inclination of the slipway. The rotation of the GBF, $\varphi$ when it reaches the end of the slipway is determined by one parameter: the inclination of the slipway. The minimum inclination at which the structure starts moving can be determined by: $\varphi_{min} = \arctan\mu_c$. With a coefficient of friction of 0.05, $\varphi_{min} = 2.86°$,

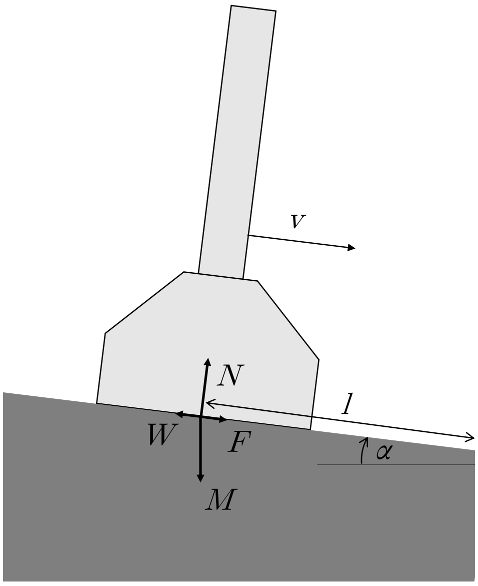

**Figure 3.6:** First phase of the launching process, the sliding phase illustrated with relevant forces.

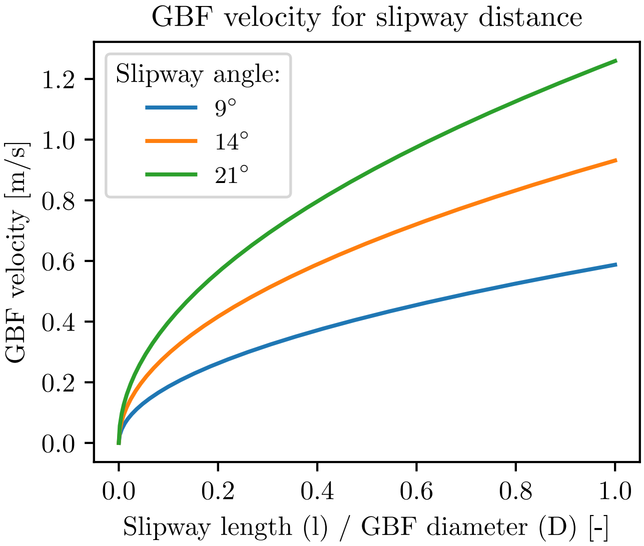

**Figure 3.7:** The sliding speed of the GBF scale model (1:100 scale) for varying slipway length and inclination for $\mu_c = 0.1$. GBF velocity at 0.50*D was used as initial conditions for the equations of motion in Table 5.4 when comparing the mathematical to the physical models.

while for $\mu_c = 0.1$, $\varphi_{min} = 5.71°$. GBF velocity for varying slipway length for three slipway inclinations is shown in Figure 3.7.

When the GBF reaches the water surface, hydrodynamic forces need to be considered. As the GBF moves down the slipway, drag and buoyancy forces cause the acceleration in the direction of the slipway to decrease. When the GBF loses contact with the slipway, the driving force disappears completely and the GBF floats freely in water. A partially submerged GBF with respective forces is shown in Figure 3.8, in which the additional forces with respect to the previous phase are:

$F_d$ = drag force
$F_b$ = buoyant force

In contrast to other forces that act on the center of gravity of the GBF, these forces act on the center of buoyancy. The drag force is given by:

$$F_d = \frac{1}{2}\rho v^2 C_d A \tag{3.3}$$

in which:

$v$ = velocity of the object moving though the fluid [m/s]
$C_d = 0.6$ = drag coefficient [-]
$A = h * 2R$ = projection of area subject to drag [m$^2$]

For a (partially) submerged base slab, a drag coefficient of 0.60 was used. The surface area used to calculate the drag was calculated by multiplying height $h$ and width $2R$ of the submerged section of the GBF, which is a slight simplification until the full GBF width is submerged. The

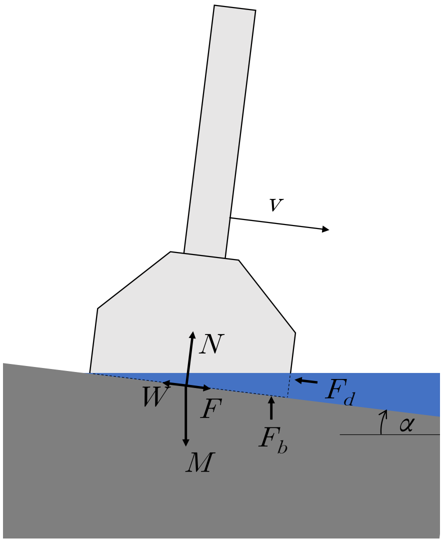

**Figure 3.8:** The GBF continues to slide down the slipway while being resisted by an increasing water column. In addition to the forces from the previous phase illustrated in Figure 3.6, a buoyant force $F_b$ and a drag force $F_d$ act on the GBF.

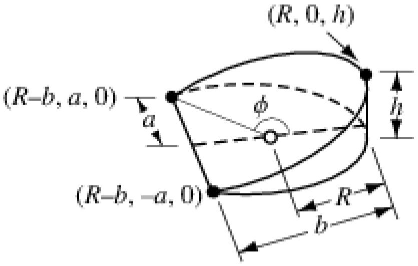

**Figure 3.9:** The volume of a cylindrical wedge. Image is from: (Weisstein, n.d.).

buoyant force was calculated using the weight of the submerged volume of the GBF, which is:

$$F_b = V\rho g, \tag{3.4}$$

where V is the submerged volume. Since the GBF moves into the water with an inclination, the volume that generates the buoyant force has the shape of a cylindrical wedge until the complete base plate is submerged. The volume of this wedge was calculated using the following formula:

$$V = \frac{hR^2}{3}\left(\frac{3\sin\phi - 3\phi\cos\phi - \sin^3\phi}{1-\cos\phi}\right) \tag{3.5}$$

in which the variables are according to Figure 3.9, and for $b < R$:

$$\phi = \cos^{-1}\left(\frac{R-b}{R}\right) \tag{3.6}$$

while for $b > R$:

$$\phi = \cos^{-1}\left(\frac{b-R}{R}\right) \tag{3.7}$$

To find the structure's acceleration, which can be used to determine its velocity and position, the force balance was solved. Since the drag force depends on the velocity and both the drag and buoyant force depend on the location of the GBF, the force balance was solved numerically in time using numerical integration. At each time step, the forces $M, N, W, F_b$, and $F_d$ were calculated and the resultant force $F$ was given by the sum of all forces in the direction of the slipway. The acceleration of the partially submerged GBF on the slipway is given by: $a_{wet} = \frac{F_{res}}{m}$, in which:

$$\begin{aligned} F_{res} &= F - W\ , \\ F &= (M - F_b)\sin\alpha, \\ W &= \mu_c N + F_d\ , \\ N &= (M - F_b)\cos\alpha. \end{aligned}$$

Filling in the above formulas yields:

$$a_{wet} = \frac{(M - F_b)\sin\alpha - (\mu_c(M - F_b)\cos\alpha + F_d)}{m} \tag{3.8}$$

for the total acceleration of the GBF on the slipway. After solving the force balance, accelerations and therefore velocity and positions were determined. For each iteration, velocity and location from the previous time step are used to calculate buoyancy and drag, which results in a new acceleration which was then used to calculate the next velocity and location. The trapezoidal rule was used to solve for velocity and position numerically, according to the formulas below:

$$v(t) = v(t-k) + 0.5 \cdot (a(t-k) + a(t)) \cdot k, \tag{3.9}$$

$$x(t) = x(t-k) + 0.5 \cdot (v(t-k) + v(t)) \cdot k, \tag{3.10}$$

where $k$ is the time step and $t$ is time.

Figure 3.10 shows the results for three slipway inclinations 9°, 14° and 21°, using a time step of 0.05 s. The GBF has no initial velocity, i.e. the simulation starts when the GBF base has first contact to the water. For an inclination of 9°, the GBF reaches a maximum velocity of 5.28 m/s and for 14°, the maximum velocity is 7.54 m/s and for 21°, the maximum velocity is 9.26 m/s before being slowed down by the water and lifted from the slipway.

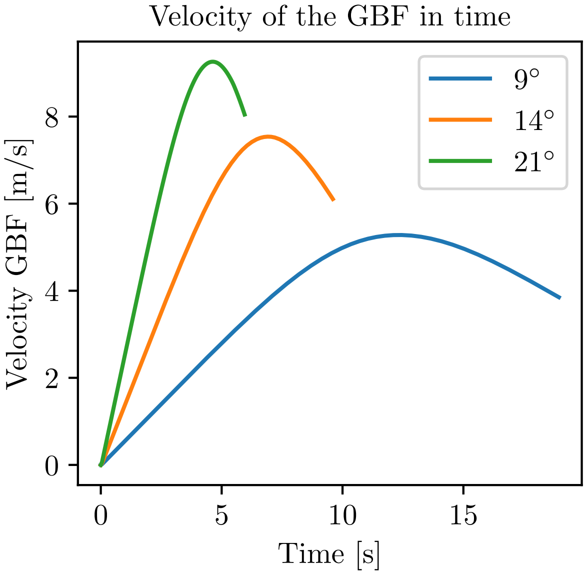

**Figure 3.10:** The velocity of the GBF in time as it slides down the slipway for three slipway inclinations, 9°, 14° and 21°. The graphs end when the buoyant forces exceed the weight, and the GBF starts floating.

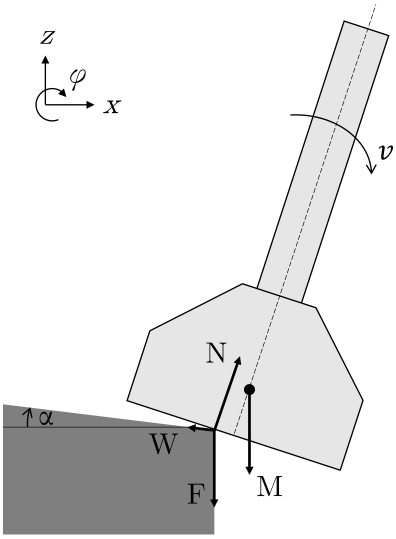

**Figure 3.11:** In the case of a dry slipway ending, the GBF tilts over the edge of the slipway as soon as the center of gravity passes the edge of the slipway.

## 3.4 Tipping: equations of motion

Equations of motion were used to model more complicated motions. The GBF tipping over the edge of the slipway (dry) is a process that was modelled by equations of motion. The main limitation of equations of motion is that including fluid-structure interaction is very complicated. In this section, the equations of motions for a GBF tipping over the slipway end are given.

If the slipway ends above the water surface, as shown in Figure 3.11, the GBF will start tilting once the center of gravity passes over the slipway edge. Depending on the height of the freeboard, the GBF is given an additional rotational and transverse velocity to the already present velocity and inclination due to the sliding phase. A large point load, N in Figure 3.11, will move along the base of the GBF as it continues to slide over the contact point. Sliding is resisted by a frictional force, W.

GBF motions during the tipping phase were determined by solving a system of equations of motion. In these formulas, water reaction forces is not taken into account. These formulas are based on Hak (2005) and were converted to the axis conventions used in this thesis.

To shorten the formulas,

$$a = \sin(\varphi_G) - \mu_c \cos(\varphi_G) \tag{3.11}$$

$$b = \cos(\varphi_G) + \mu_c \sin(\varphi_G)\,. \tag{3.12}$$

The equations of motion during the tipping phase of the GBF then become:

$$m\ddot{x} = Na \tag{3.13}$$

$$m\ddot{z} = -M + Nb \tag{3.14}$$

$$I_y\ddot{\phi} = N\left(-ax(t) + bz(t)\right), \tag{3.15}$$

forming three equations with three unknowns $x(t)$, $z(t)$ and $\varphi(t)$. Finding the normal force $N$, required an extra relation. This relation follows from the boundary condition which states that the bottom of the GBF needs to be in contact with the slipway edge, which is described by the following geometric relation:

$$z(t) = -x(t)\tan(\varphi(t)) + \frac{h_{cg}}{\cos(\varphi(t))} \tag{3.16}$$

Solving these equations, which was done numerically, GBF kinematics (position, velocity and acceleration) in all three degrees of freedom is determined. The equations were solved in Maple, the code can be found in Appendix B. For the range of tested variables for freeboard height and slipway inclinations in the physical model tests, the GBF was often already in contact with the water before the tipping phase starts, which cannot be modeled by these equations of motion. In Figure 3.12 and Figure 3.13, an example of the output from these equations of motions is shown for the most extreme launching position that was tested in the physical models with a slipway inclination of 9°, and a freeboard height of +4 m (at a 1:1 scale). The point at which the GBF makes first contact with the water surface in this situation is marked by ‘x’ in the figures. GBF velocity at this point is 2.26 m/s and rotation is 14°.

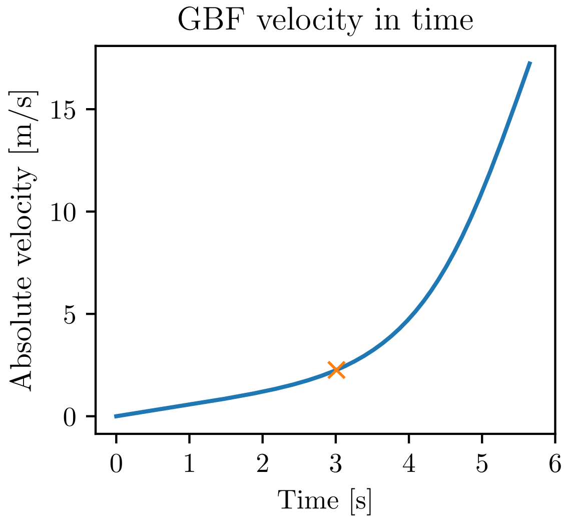

**Figure 3.12:** Absolute velocity of the GBF as it falls over an edge. The initial velocity is 0 m/s, slipway inclination is 9° and friction between the base and edge is 0.10.

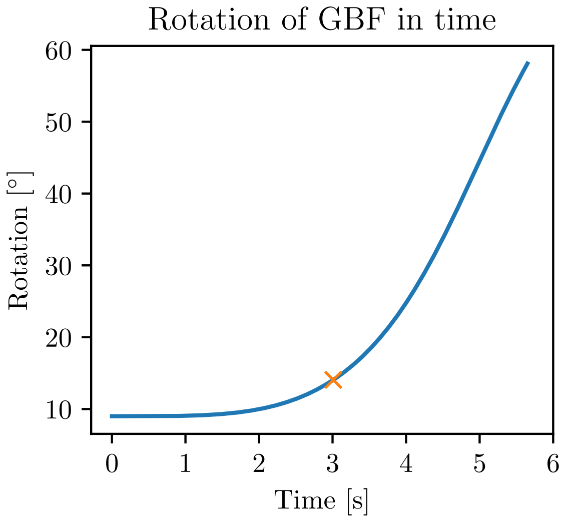

**Figure 3.13:** Rotation of the GBF as it falls over an edge. The initial velocity is 0 m/s, slipway inclination is 9° and friction between the base and edge is 0.10.

## 3.5 Floating: equations of motion

The dynamic response of the GBF to launching activities was determined by solving the governing equations of motions for floating structures. Several key components of the equations were determined, such as the hydrodynamic damping, added mass and radiation damping. This was done by performing hand calculations using (adapted) formulas from literature sources, using Ansys Aqwa diffraction software and finally by scale-model experiments. First, the equations of motion are presented, after which the calculation of the hydrodynamic coefficients is shown.

The submerged section of the GBF, shaped like a vertical and symmetric cylinder, was simplified to a three degree-of-freedom mass-spring-damper system, with the GBF modelled as a rigid body. Motions occur in three directions: vertically (heave), horizontally (surge) and rotationally (pitch), as visualised in Figure 3.14. Formulating the equations of motion is done by considering the sum of all forces on the floating cylinder, which results in:

$$M\ddot{X} = F_{hy} + F_R \tag{3.17}$$

in which $M$ is the mass matrix, $\ddot{X}$ is the acceleration vector, and $F_{hy}$ are the hydrostatic force components, depending linearly on the displacement vector $X$ in the form:

$$F_{hy} = -KX \tag{3.18}$$

in which K is the stiffness matrix. The structure is not moored, so the stiffness matrix consists of hydrostatic components only. $F_R$ is the resulting force of hydrodynamic components, split into an acceleration and a velocity phase:

$$F_R = -m\ddot{X} - C\dot{X} \tag{3.19}$$

in which $m$ is the added mass matrix, $C$ is the damping matrix and $\ddot{X}$ and $\dot{X}$ are the acceleration and displacement vectors. When the GBF moves in water, a body of water moves together with the GBF, effectively increasing its mass. This mass is referred to as added mass and should be taken into account for floating structures. Substituting (3.18) and (3.19) into (3.17) resulted in the system of equations of motion:

$$(M+m)\,\ddot{X}+C\dot{X}+KX=0. \tag{3.20}$$

No external forces are present in this equation of motion, which is due to the fact that only transient behaviour due to certain initial conditions is of interest. To further formulate the equations of motion, added mass, damping and stiffness matrices were determined. Since the structure is not moored, there is no restoring force for surge motions, indicating the absence of a restoring spring force in that direction. The simplified dynamical model of the floating GBF is visualised in Figure 3.15. Vertically and rotationally, motions are restricted by a spring and damper, horizontally by a damper only.

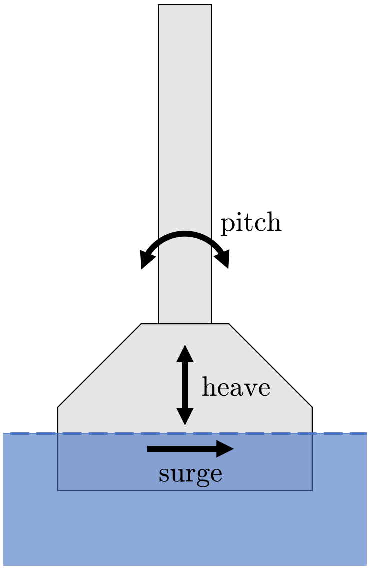

**Figure 3.14:** Motion directions of a floating GBF.

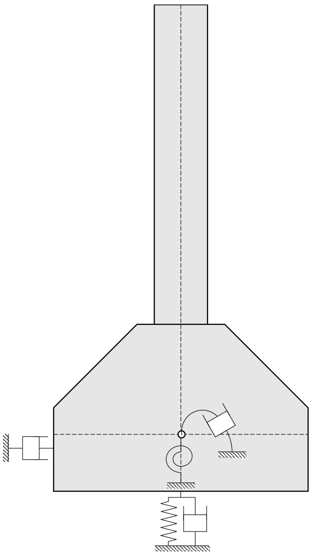

**Figure 3.15:** Dynamic mass-spring-damper model used to derive the equations of motion.

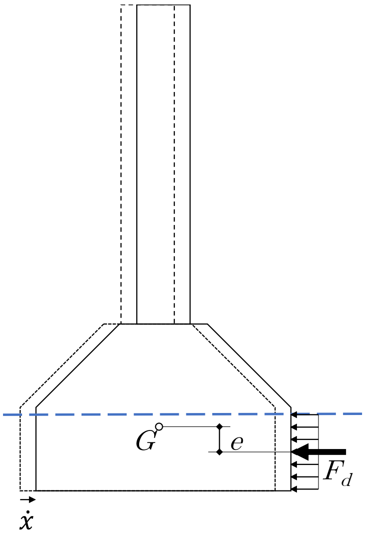

**Figure 3.16:** The eccentricity of the drag force with respect to the center of gravity.

With one exception, all matrices were assumed to be symmetric, i.e. there are no coupling terms. Only one coupling term was used, which relates the horizontal velocity of the GBF to its resulting rotation. The horizontal drag force acts in the middle of the submerged section of the GBF so the force acts eccentrically with respect to the center of gravity. This eccentricity is denoted by $e$ and causes a moment in the $\varphi$ direction. The eccentricity of this load depends on the vertical $(y(t))$ position of the GBF, as visualised in Figure 3.16. Damping in the horizontal direction is caused by drag, which depends on velocity *squared*. Therefore, the $x$ term in the $\dot{X}$ matrix is $x^2$. The matrices in Equation 3.20 are:

$$M=\begin{bmatrix} m+m_z & 0 & 0 \\ 0 & m+m_x & 0 \\ 0 & 0 & I_y+I_\varphi \end{bmatrix}, C=\begin{bmatrix} c_z & 0 & 0 \\ 0 & c_x & 0 \\ 0 & c_x\cdot e & c_\varphi \end{bmatrix}, K=\begin{bmatrix} k_z & 0 & 0 \\ 0 & k_x & 0 \\ 0 & 0 & k_\varphi \end{bmatrix},$$

and:

$$\ddot{X}=\begin{bmatrix} \ddot{z} \\ \ddot{x} \\ \ddot{\varphi} \end{bmatrix}, \dot{X}=\begin{bmatrix} \dot{z} \\ \dot{x}^2 \\ \dot{\varphi} \end{bmatrix}, X=\begin{bmatrix} z \\ x \\ \varphi \end{bmatrix}.$$

Writing the equations separately gives:

$$(m + m_z) \cdot \ddot{z} = -c_z \cdot \dot{z} - k_z \cdot z \tag{3.21}$$

$$(m + m_x) \cdot \ddot{x} = -c_x \cdot \dot{x}^2 \tag{3.22}$$

$$(I_y + I_\varphi) \cdot \ddot{\varphi} = -c_\varphi \cdot \dot{\varphi} - k_\varphi \cdot \varphi - c_x \cdot \dot{x}^2 \cdot e \tag{3.23}$$

## 3.6 Floating: Hydrodynamic components

First, the coefficients of the above matrices were determined analytically using existing (adapted) formulas. Then, the coefficients were determined using diffraction software ANSYS AQWA. It should be noted that many components are in fact frequency- or amplitude- dependent. During the floating stage of the launch, the structure moves at its natural frequency so when necessary, the (undamped) natural frequency was used to determine the frequency dependent coefficient. The analytical formulas are often based on experiments rather than being derived from theoretical mathematical formulations. The calculated hydrodynamic components were calibrated using the physical scale model tests, which is done in Chapter 5.

### 3.6.1 Analytical calculations

Analytically, three different hydrodynamic components were determined: added mass, damping and restoring spring coefficients for all degrees of freedom. For surge motions, there is no restoring spring force. Detailed calculations of the hydrodynamic components is done in Appendix C, most important aspects are summarized below.

According to Barltrop (1998), added mass can be approximated by spherical volumes around the submerged section of the floating structure. For example, added mass for heave motions is generated by a hemispherical volume under the GBF, with the same diameter as the GBF itself while for surge, added mass is generated by an ellipsoidal volume around the GBF. Pitch added inertia was calculated using a formula from a literature source (Ghadimi, Paselar Bandari, & Bankhshandeh Rostami, 2012).

The restoring spring terms for heave was determined using the displacement method. The GBF was displaced downward and the extra submerged volume causes a restoring upward force which results in a spring constant when dividing by the displacement. The vertical spring coefficient is therefore equal to:

$$k_z = \rho g \pi R^2 \tag{3.24}$$

According to Journée and Massie (2001), the righting moment of a floating structure due to a rotation is given by $\rho g \nabla \cdot \overline{GM} \cdot \varphi$ for small angles, which leads to a rotational spring constant of:

$$k_\varphi = \rho g \nabla \cdot \overline{GM} \tag{3.25}$$

for small angles. Damping of floating structures can be divided into two main components that differ greatly in their physics. Viscous damping is caused by viscous effects such as for example skin friction and vortices. In radiation damping, energy is dissipated by generated radiation waves of the moving structure. For heave motions, both damping components were expected to be significant while pitch damping was expected to be mainly viscous. In the rotational $\varphi$-direction, damping mainly consist of viscous damping according to (Jiang, Gou, & Teng, 2013) so radiation damping was neglected. Viscous damping is, however, non-linear and dependant on frequency and amplitude of the motion (Journée & Massie, 2001). Although non-linearity is no issue mathematically, linear damping components for heave and pitch were sought for to be able to simplify the models and to compare results easily. According to Journée and Massie (2001), linearization of the quadratic damping coefficient can be done by:

$$c_i^{lin} = \frac{8}{3\pi} \cdot \omega \cdot A_0 \cdot c_i^{vis} \tag{3.26}$$

in which:

$c_i^{lin}$ = linearized damping in the $i$ degree of freedom
$\omega$ = angular frequency [rad/s]
$A_0$ = motion amplitude [m or rad]
$c_i^{vis}$ = non-linear quadratic damping in the $i$ degree of freedom

Since the structure floats freely in the water, its natural frequency was used for $\omega$. The mathematical models were compared to the physical scale model tests so the amplitude of the average displacement in the physical scale model tests was used to calculate the linear damping coefficient.

Horizontal motions are damped by viscous drag on the GBF moving through the water. Drag on the GBF due to a horizontal velocity is given by:

$$F_d = \frac{1}{2}\rho v^2 C_d A \tag{3.27}$$

in which:

$\rho$ = mass density of the fluid [kg/m$^3$]
$v = \dot{x}$ = velocity of the object moving though the fluid [m/s]
$C_d = 0.6$ = drag coefficient [-]
$A$ = Surface area of the structure exposed to the water flow [m$^2$]

The drag coefficient of 0.60 was assumed for horizontal motions of the GBF. For certain processes, the draft changes in time, which was taken into account in the calculations for a fully submerged slipway.

### 3.6.2 ANSYS Aqwa

Determining added mass, radiation damping and hydrostatic spring coefficients was also done using ANSYS Aqwa. A detailed explanation of the model and results are presented in Appendix D. ANSYS Aqwa is a boundary element method hydrodynamics simulation and diffraction analysis software. The structure geometry was modelled by a finite amount of diffracting panels. The panels were defined by a boundary condition that states that no water can pass through. The floating body was excited by incident waves by applying wave pressures at different frequencies and directions. For each panel, a the pressure distribution was numerically calculated by Aqwa. The resulting added mass and radiation damping coefficients are frequency dependent.

Aqwa was run with one wave direction for 70 intermediate wave frequencies between 0.04 Hz (T=25 s) and 0.16 Hz (T=6.25 s). Since only natural frequencies in two degrees of freedom (heave and pitch) were of interest, a small frequency band was chosen that the two natural frequencies fall in this band. Frequency dependent coefficients were determined for the natural frequencies since the structure to be modelled is freely floating and therefore moves at its natural frequencies.

The calculated damping coefficient only accounts for radiation damping so an underestimation of the damping coefficient is expected. Viscous damping effects and aerodynamic drag of the superstructure are not taken into account by ANSYS Aqwa. It is therefore to be expected that Aqwa massively underestimated the pitch damping (which have been determined to be mainly viscous). The results are compared to the mathematical calculations of the hydrodynamic components in the next section.

### 3.6.3 Results

More details about the calculations of the hydrodynamic components can e found in Appendix C. The table below shows the results from the analytical calculations as well as the ANSYS Aqwa output.

**Table 3.2:** Heave hydrodynamic components. Aqwa results were calculated for a natural frequency of 0.119 Hz

| Parameter | Symbol | Analytical | Aqwa | Unit |
|---|---|---|---|---|
| Added mass | $m_z$ | 7.43E+06 | 5.57E+06 | kg |
| Hydrostatic stiffness | $k_z$ | 7.17E+06 | 7.16E+06 | N/m |
| Linear radiation damping | $c_z$ | 5.69E+05 | 1.08E+06 | Ns/m |
| Linearized viscous damping | $c_z^{lin}$ | 1.44E+06 | 0 | Ns/m |

**Table 3.3:** Pitch hydrodynamic components. Aqwa calculations were performed at a natural frequency of 0.067 Hz

| Parameter | Symbol | Analytical | Aqwa | Unit |
|---|---|---|---|---|
| Added mass | $m_\varphi$ | 4.06E+08 | 1.78E+08 | kg m$^2$ |
| Hydrostatic stiffness | $k_\varphi$ | 2.93E+08 | 2.96E+08 | Nm/rad |
| Linear radiation damping | $c_\varphi$ | 0 | 6.86E+05 | Nm/(rad/s) |
| Linearized viscous damping | $c_\varphi^{lin}$ | 1.50E+08 | 0 | Nm/(rad/s) |

**Table 3.4:** Surge hydrodynamic components.

| Parameter | Symbol | Analytical | Unit |
|---|---|---|---|
| Added mass | $m_x$ | 3.5E+06 | Nm$^2$/rad |
| Damping | $c_x$ | 1.50E+08 | Nm/(rad/s) |

## 3.7 Concluding remarks

The aim of this chapter was to answer the subquestion: “Which mathematical approaches can be used to describe the GBF motion during each phase of a gravitational launch?”. Translational movements when the GBF is in full contact with the slipway were described using a simple force balance, both for a dry and a partially submerged slipway. For the kinematics as it tips over the slipway edge, equations of motion were derived and solved. The main limitation of this set of equations of motion is that hydrodynamic forces are not included. For the kinematics of the freely floating structure, equations of motions were solved and hydrodynamic components such as added mass and radiation damping were determined analytically and numerically using diffraction software Ansys AQWA. The presented mathematical models are sufficiently accurate to make a conceptual design, which will be shown in the last chapter of this thesis, but first, the hydrodynamic coefficients need to be calibrated and the models need to be validated. This was done using physical scale model tests, which are described in the next chapter. A calibration of the results based on physical scale model tests is made in Chapter 5.

# Chapter 4

# Physical scale model tests

In Chapter 3, mathematical models describing the phases of a gravitational launch were derived. To check whether the models are valid and compare well to reality, they were compared to physical scale model tests. Physical models are performed to represent a physical process at another (smaller) scale such that it becomes easier (i.e. less costs, time, space) to study the phenomenon. In a physical scale model test, it is possible to model the full launching process, naturally including all hydrodynamic, aerodynamic and other (unknown) components. Experiments were performed at a 1:100 scale to calibrate and validate the mathematical models, and to get more insight into the behaviour of the GBF when it is launched gravitationally. This chapter merely describes the experiment set-up and presents the results, so no research question is answered yet. First, a comprehensive description of the experiment set-up is presented, containing key information on how the experiments were performed. Then, information on the data collection and processing is given and finally, the measured data is shown. An analysis of the results and comparison to theory is presented in Chapter 5, answering the second research question.

## 4.1 Test Objective

The experiments had three test objectives: (1) to calibrate the hydrodynamic components (2) to model a gravitational launch for different slipway set-ups and (3) to visually and quantitatively observe the impact of the freeboard height, GBF velocity, and slipway inclination on the GBF dynamics. Two sets of experiments were performed: (1) free decay tests and (2) launch tests. The free decay tests were used to calibrate and validate the hydrodynamic components used in the mathematical model for a floating GBF, which is done in the next chapter. Launch tests were performed to validate the mathematical models and to get more insight into the launching process and dynamic behaviour. Two sets of launch tests were preformed, tests with an abruptly ending slipway and test with a fully submerged slipway.

To quantitatively determine the impact of slipway geometry on GBF dynamics, a parameter that represents the severity of the GBF dynamics was required. The maximum rotation of the GBF ($\varphi_{max}$) reached during the launching process was used as this parameter because it was assumed to represent the severity of the dynamics well and it could be measured relatively easily. With this parameter, an objective comparison can be made between the different slipway geometries.

## 4.2 Experiment set-up

This section contains key information on the experiment approach by describing the test facility, model scaling and lay-out.

### 4.2.1 Description of test facility

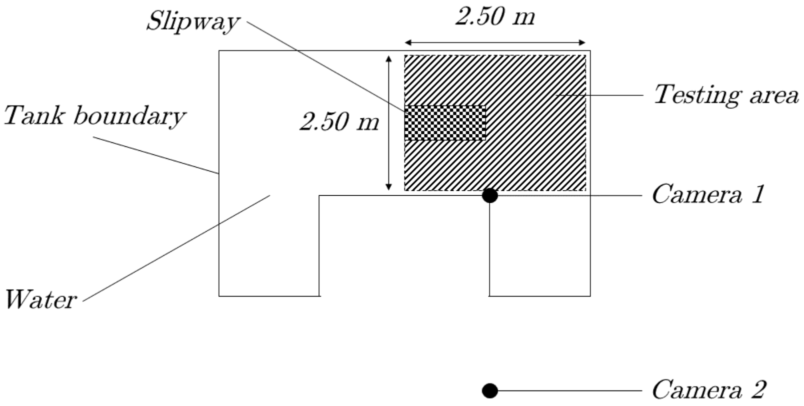

**Figure 4.1:** Top view sketch of the basin. The basin section used for the tests is shaded diagonally and the location of the slipway is checkered.

The scale model tests were carried out in the temporary 3D basin at BAM Infraconsult in Utrecht. This basin consists of a large rectangular tank which was built outside and covered with a tent. The basin is 5 m wide and 8 m long and has a height of 0.5 m. At the time of the experiments, another experiment set up was also present in the tank so a smaller section of 2.50 m by 2.50 m was used for this experiment. It is important that reflected waves generated by the moving floating structure do not reach and excite the structure during the experiment. That is the main reason why the experiments were not performed in the wave flume, the narrow width would result in large excitation due to reflected waves. Water depth varies between 0.31 and 0.33 m, depending on the experiment set up. A picture of the tank is shown in Figure 4.2.

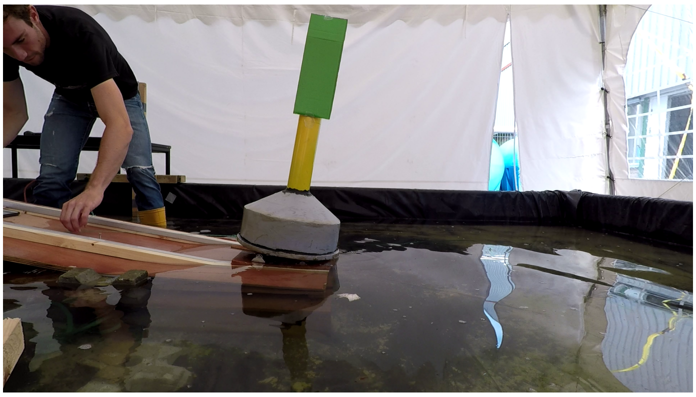

**Figure 4.2:** Overview image (camera 1) of the testing facility with the inclined slipway and the GBF scale model. The space on the right was used for the free decay tests.

**Figure 4.3:** Image of the GBF on the slipway inclined at 14°, with a +4 cm freeboard height and released from the low position.

### 4.2.2 Model scaling

The scale for this experiment was chosen based on:

- the size of the available scale model;
- the size and available depth of the 3D basin and wave flume;
- and the range of motion that can be accurately measured.

Froude scaling rules were used for these experiments, which means the Froude number was be kept constant. The Froude number is a dimensionless number that describes the ratio between inertia and gravity forces, which are the most important for this experiment. The Froude number is given by:

$$Fr = \frac{u}{\sqrt{gD}}, \tag{4.1}$$

where $u$ is the velocity, $g$ is gravitational acceleration and $D$ is the characteristic length of the structure. Due to Froude scaling, turbulence effects are not scaled properly. Turbulence has an effect on damping and is therefore also relevant for these experiments. For proper turbulence scaling, the Reynolds number should be kept constant, which describes the ratio between inertia forces and viscous forces. The Reynolds number is given by:

$$\mathrm{Re} = \frac{uL}{\nu}, \tag{4.2}$$

in which $u$ is the velocity of the fluid or structure, $L$ is a length scale of the structure and $\nu$ is the kinematic viscosity ($10^{-6}$ m$^2$/s) of water. Scaling requirements by Froude and Reynolds cannot be satisfied simultaneously. Froude scaling was preferred because gravitational forces are expected to be dominant over viscous forces. Furthermore, for large enough Reynolds numbers ($> 3500$), flow is always turbulent and damping coefficients are expected to be constant. The experiments were be performed with a Froude scale factor $\lambda$ of 100. Time is then scaled with the square root of the scaling factor and will be equal to: $\sqrt{100} = 10$. All relevant physical parameters are scaled by a factor according to Table 4.1. Since the kinematic viscosity of water is the same in the scale model and real life, the difference in Reynolds number between the scale model and real size can be calculated by $\frac{\sqrt{\lambda}\lambda}{1} = 1000$. Using order of magnitude of $u = 10^0$ m/s and $L = 1$ m, $\mathrm{Re}_{scale} = 10^5$ and $\mathrm{Re}_{real} = 10^8$. Turbulent flow occurs in both situations and drag was expected to be of the same order of magnitude but slightly larger in the 1:100 scale than in the 1:1 scale (Panton, 2013).

**Table 4.1:** The scale factor for relevant physical parameters according to Froude scaling.

| Physical Parameter | Units | Scale factor | Physical Parameter | Units | Scale factor |
|---|---|---|---|---|---|
| Length | m | $\lambda$ | Force | N | $\lambda^3$ |
| Time | s | $\sqrt{\lambda}$ | Moment | Nm | $\lambda^4$ |
| Mass | kg | $\lambda^3$ | Linear damping | N/m/s | $\lambda^{2.5}$ |
| Linear velocity | m/s | $\sqrt{\lambda}$ | Linear spring | N/m | $\lambda^2$ |
| Linear acceleration | m/s$^2$ | $\lambda^0$ | Moment of inertia | kg m$^2$ | $\lambda^5$ |
| Angular velocity | rad/s | $\lambda^{-0.5}$ | Angular damping | Nm/rad/s | $\lambda^{4.5}$ |
| Angular acceleration | rad/s$^2$ | $\lambda^{-1}$ | Angular spring | Nm/rad | $\lambda^4$ |

To given an idea of the scale model dimensions, for a 1:100 scale, the base of the GBF has a diameter of 30 cm. The scale model was constructed by Erik ten Oever and is an exact replica of an actual GBF, including inner walls and correct wall thicknesses (Ten Oever, 2019). Although the weight, center of gravity and draft have been validated, the moment of inertia was not. Since the scale model was assumed to be an exact replica, the moment of inertia was also assumed to be correct.

### 4.2.3 Model lay-out

For the free decay tests, no special structures other than the GBF scale model were used. The GBF was placed in the center of the testing area to maximise the distance to the boundaries.

For the slipway tests, two wooden 'skidding beams' were attached to the bottom of the GBF, and a wooden ramp was constructed as a slipway. Although the initial idea was to slide the GBF down the slipway, the choice was made to roll it over a set of wheels. Obtaining a sufficiently small friction coefficient using (metal) sliders, grease, oil or soap proved to be extremely difficult due to practical limitations (scale effects) in finished surfaces, which was also experienced by Rodriguez, Moura, Esperança, and Raigorodsky (2014) during their jacket launch tests. The friction coefficient of the wheel system was calculated to be approximately 0.10 instead of the desired 0.05. The objectives of the tests was not to verify one specific design but to generate knowledge on the effect of certain parameters, so this was not considered to be a problem.

For the abruptly ending launches, the set of wheels were attached to the inclined slipway, with one wheel acting as the point around which the GBF tips, as shown in Figure 4.4a and 4.3. To capture a large range of varying inclinations, freeboard heights and velocities, the choice was made to perform the experiments for three different slipway inclinations (9°, 14°, and 21°), three different freeboard heights (-2 cm, 0 cm and +4 cm) and two different velocities (high or low). A full list of the experiments performed is also shown in Table 4.2. The velocity was adjusted by simply releasing the GBF from a larger distance up the slipway. For a 'high' initial velocity, the edge of the GBF was positioned approximately 13 cm over the last wheel. For a 'low' velocity, the center of gravity was positioned 2 cm over the last wheel so that the GBF starts tipping with almost no initial velocity.

For the submerged slipway launches, where the GBF rolls down the ramp until it floats, the wheels were attached to the GBF. The GBF was released from the position where it just touches the water for three different slipway inclinations (9°, 14°, and 21°). A detailed view of this structure can be seen in Figure 4.9 and a sketch in Figure 4.4b.

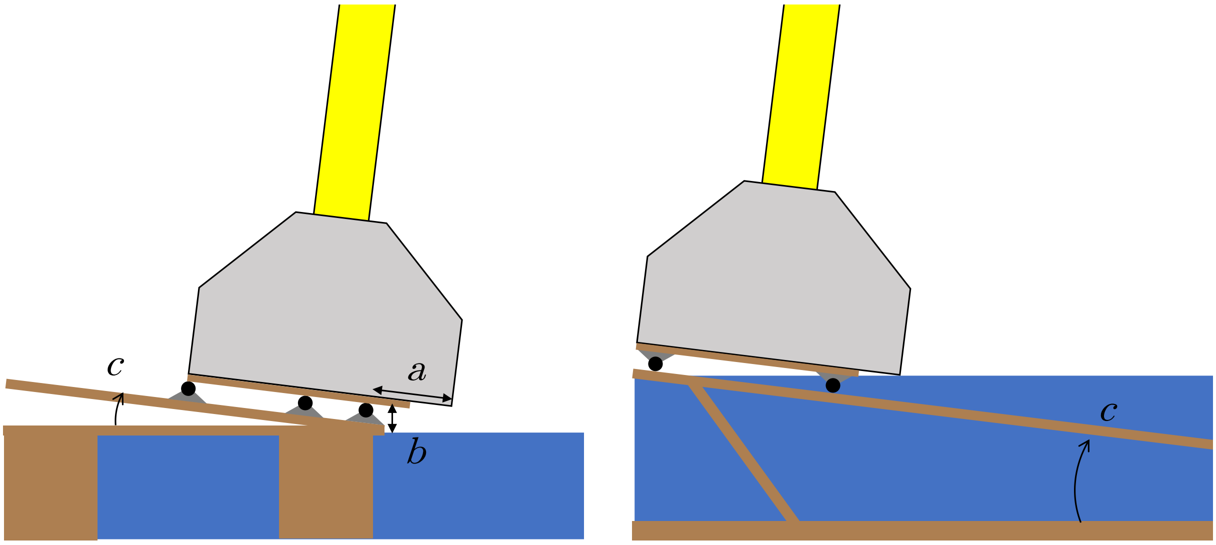

**(a)** Abruptly ending slipway launch test set up.

**(b)** Submerged slipway launch test set up.

**Figure 4.4:** Sketches of the experiment set up. The inclination of the slipway (c) used were: 21°, 14° and 9°. Freeboard heights for an abruptly ending slipway (b) were: -2 cm, 0 cm and 4 cm. The freeboard height in this figure is positive. The positions of the GBF on the slipway (a) was approximately 2 cm (low) and 13 cm (high). Note that for some combinations, the base of the GBF was (partially) submerged.

### 4.2.4 Experiment program and protocol

For the free decay tests, the GBF was displaced rotationally or vertically, and released. Cameras recorded a video of the moving structure, which was used to collect the data. Releasing the structure was done ‘by hand’ so the experiment was re-performed a few times. The best test was chosen based on (1) minimal motions of the structure in the direction other than the direction of interest and (2) minimal extra velocity generated by the release. The initial conditions of the free decay tests was determined from the video analysis.

For the submerged slipway test, the ramp was placed in the basin and the GBF was placed so that the GBF just touches the water surface. For the abruptly ending slipway tests, the water height was checked and adjusted until the required freeboard had been reached. The slipway inclination was also checked and adjusted to an accuracy of ±0.5°. The GBF was placed on the slipway and held in place by a string in the ‘high’ or ‘low’ position. After starting the camera, the GBF was released, slides down the slipway and tips over the edge into the water. After the motions have dissipated, it was retrieved and placed back on the slipway and the video was stopped. A more detailed protocol can be found in Appendix E.

## 4.3 Data collection and processing

Since a large section of the model was be above the water surface and motions primarily occured in a 2D plane, motion tracking software was used. To enable motion tracking software to track GBF motions, a green rectangle was attached to the GBF, which can also be seen in Figure 4.2. Two cameras were used to collect data. Due to obstructions in the wave tank, a wide-angle video recorder (GOPRO), referred to as camera 1 in Figure 4.1, was used to record the full launching sequence, as is shown in Figure 4.5. This video captured the full launch and was used in the analysis to detect errors, observe a ‘splash’ and verify the initial conditions. Wide angle videos result in distortion of the frame near the edges resulting in incorrect position and inclination measurements. This camera was therefore only used to verify the set-up of the experiments and to visually observe the overall behaviour of the GBF. For recording the inclination and position of the GBF, another camera was placed further away (camera 2 in Figure 4.1), zooming in (optically) on the area of interest, resulting in less distortion near the edges of the frame and therefore higher data accuracy. The video for motion tracking was recorded 50 frames per second, with a size of 1920 x 1080 pixels. Therefore, the sampling rate of the measured data is also 50 measurements per second. An example shot of the frame captured by this camera is shown in Figure 4.6.

Inclination of the GBF was determined in each frame by a computer program. In more detail, the OpenCV library was used in Python. More information about the OpenCV library and how this can be used to perform motion tracking are described by Rosebrock (2015). Large sections of the code originates from the above reference. In short, video was analysed frame-by-frame and a range of colors was detected in each frame. The color to be tracked was in high contrast to other colors in the frame. The frame was resized (which is optional), slightly blurred to soften edges, and converted to the HSV color space. This frame was then used to actually find the contours of the object to be tracked. Rosebrock (2015) presents an example for tracking a ball, but in this experiment a rectangle was used because the inclination of the object is also of interest, which cannot be measured from a circle.

The recorded video from camera 2 (the ‘far’ camera) was cut so that it starts just before every release and ends when the GBF either reaches the side of the frame or was retrieved by the observer. The videos were then merged for each individual slipway inclination, freeboard height and release position. Since each set-up was performed three times, each edited video consists of 3 releases in total, each using the same set-up. An example of this is shown in Figure 4.11.

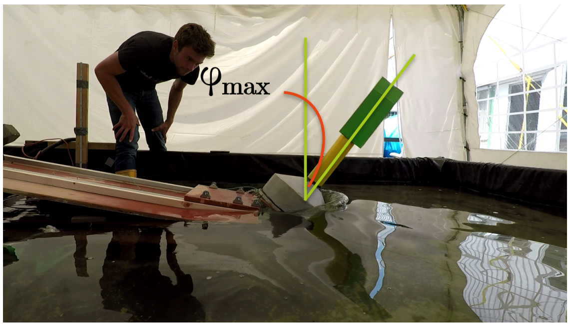

**Figure 4.5:** A frame from the video shot by the wide-angle camera (GOPRO), camera 1 in Figure 4.1. $\varphi_{max}$ is the maximum GBF rotation that was measured in the launch tests.

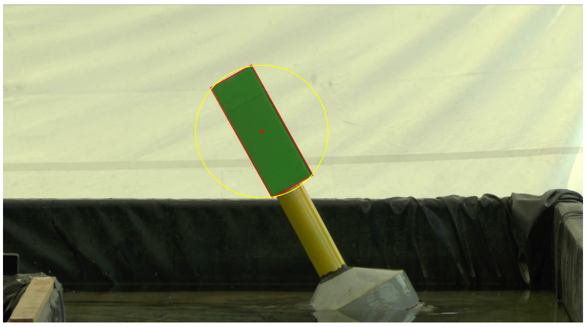

**Figure 4.6:** Screenshot of the motion tracking software processing the frame from camera 2. The red box around the green rectangle represents the object that is being tracked.

## 4.4 Results and observations

Two sets of experiments were performed: free decay tests and launches. For the free decay tests, GBF rotation and vertical displacement were measured. For the launches, GBF rotation was measured. These data are presented in this section, first for the free decay tests and second for the launch tests.

### 4.4.1 Free Decay tests

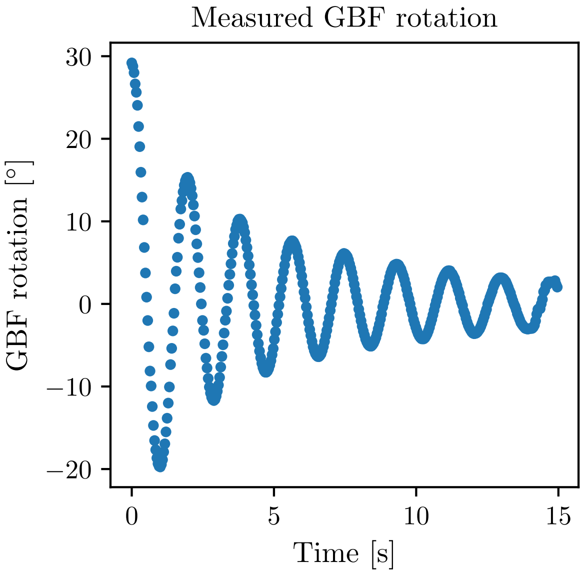

**Figure 4.7:** Data collected from the free decay test for pitch. Each data point represents the measured angle of the GBF in a frame. The data was collected 50 times per second.

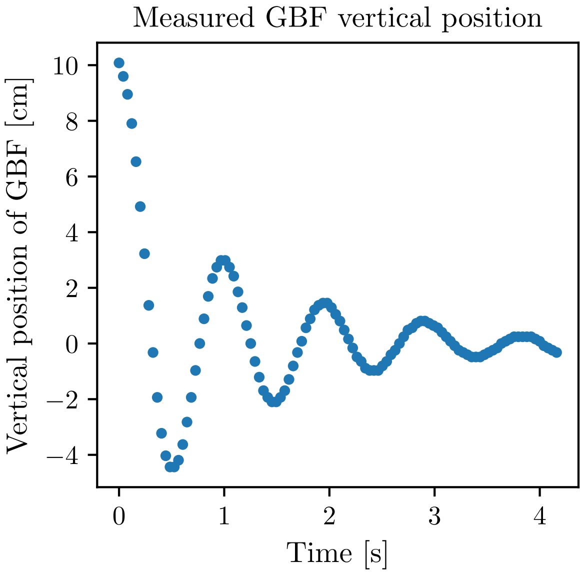

**Figure 4.8:** Data collected from the free decay test for heave. Each data point represents the vertical location of the GBF. The data was corrected to decay towards zero.

Data collected from the free decay tests consist of two data sets containing vertical position and inclination of the GBF per video frame. Results are shown in Figures 4.7 and 4.8. The figures clearly show transient harmonic motions that decay in time. The initial conditions were measured using the initial frame. Initial rotation was 29° and the initial vertical displacement was 10.1 cm.

### 4.4.2 Submerged slipway launch

For the submerged slipway launches, the GBF velocity in time was required to make comparisons to the results of the force balance. Therefore, pixels were transformed to length dimension by measuring a known distance in the video frame. The collected data then contained positions (in centimeters) in time and is converted to a velocity by dividing the distance between two positions and dividing by the frame duration, which is 1/59 second for the applied frame rate of 59 FPS. The results are shown in Figures 5.6 to 5.8.

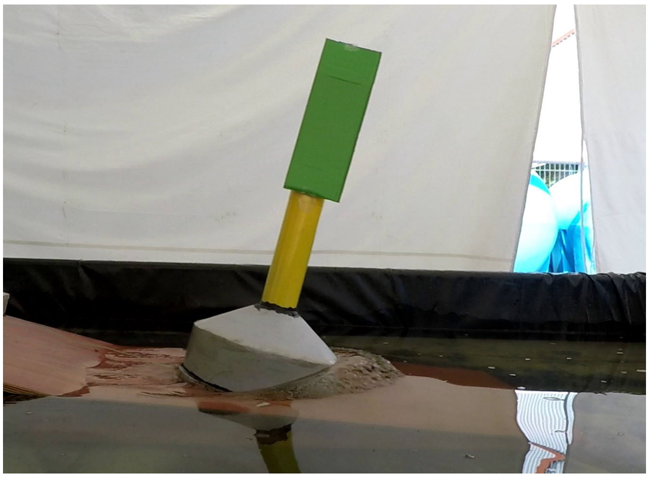

**Figure 4.9:** GBF slides down the slipway for a submerged slipway launch test.

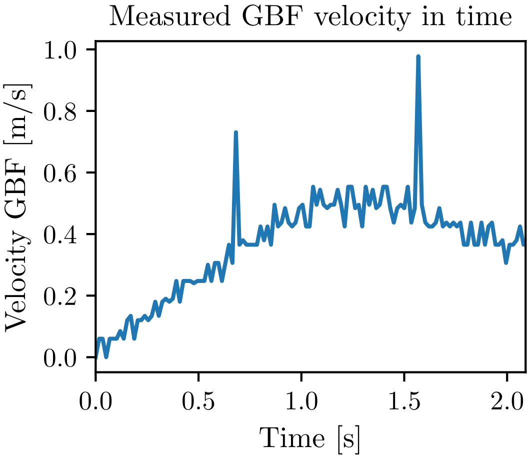

**Figure 4.10:** The measured GBF velocity for a 9° slipway.

### 4.4.3 Abruptly ending slipway launch

From the experiments, the rotation of the GBF in time was recorded. Figure 4.11 shown an example of the recorded dataset for a slipway inclination of 21°, a freeboard of 0 cm and a low velocity. This test was performed three times and three peak rotations were measured. The measured rotation at the beginning of each test is the inclination of the slipway since the GBF rests on the slipway. After the maximum rotation was reached, there were no more excitation forces and the GBF behaviour depicts that of the free decay test. The measured maximum rotations show a slight deviation. The results from all experiments are given in Appendix E. Table 4.2 shows the average (of three) maximum GBF rotations ($\varphi_{max}$) for each set-up. This data was used to observe the impact of the slipway properties on the maximum GBF rotation in Chapter 5.

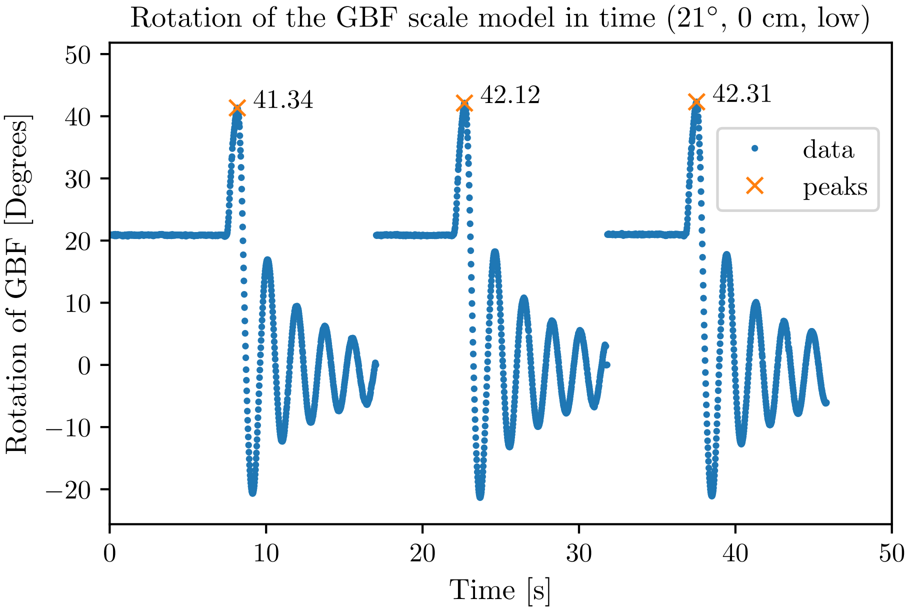

**Figure 4.11:** Example of the data collected from the experiments. The plot shows rotation of the GBF scale model in time for a slipway inclination of 21°, a freeboard height of 0 m, released from the low position. These results were obtained from the edited video file (cut and merged), and represent three tests performed for the same slipway set up. The peaks measured from this dataset are: 41.3°, 42.1°and 42.3°, the average of which is 41.9°, which can also be found in Table 4.2.

**Table 4.2:** Maximum rotation reached during the launch for all performed experiments. Each experiment is performed three times so the maximum angle shown represents the mean value of three. Two tests performed at 14°, released from the low position with a freeboard height of -2 cm were incorrectly released from the high position, so this maximum rotation is the results from *one* test only. The result of 14°, released from the high position with a freeboard height of -2 cm is therefore the average of *five* tests.

**(a)** released from the 'low' position

| | | Freeboard [cm] | | |
|---|---|---|---|---|
| | | -2 | 0 | 4 |
| Angle | 9° | 38.8° | 53.9° | 62.3° |
| | 14° | 36.4° | 48.0° | 59.7° |
| | 21° | 29.2° | 41.9° | 56.7° |

**(b)** released from the 'high' position

| | | Freeboard [cm] | | |
|---|---|---|---|---|
| | | -2 | 0 | 4 |
| Angle | 9° | 40.4° | 52.4° | 58.7° |
| | 14° | 35.6° | 45.0° | 56.9° |
| | 21° | 36.5° | 47.1° | 54.9° |

### 4.4.4 Visual observations

Visual observations were used to (1) verify the experiment set-up and look for errors and (2) identify a 'splash' and (3) estimate the depth reached of the lowest point of the GBF. Using the video from the close camera, it was found that two tests were performed with incorrect conditions, which has also been indicated in Table 4.2.

Each video was analysed to identify a 'splash'. A splash was defined by two criteria: (1) GBF moves anti-clockwise and (2) the back of the base plate is above the water line. If both criteria occur simultaneously, a splash occurs at the back side of the GBF. This is shown in Figures 4.12 and 4.13. In all but one test, a splash was observed. No splash only occurred with the following conditions: 21 °, -2 cm freeboard, released from the low position.

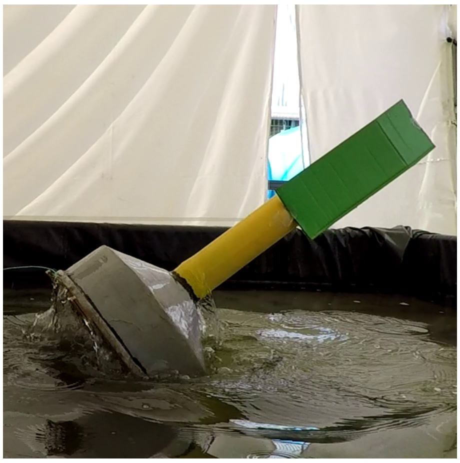

**Figure 4.12:** Just before the splash, the base slab of the GBF is immersed and the GBF starts returning to its upright position.

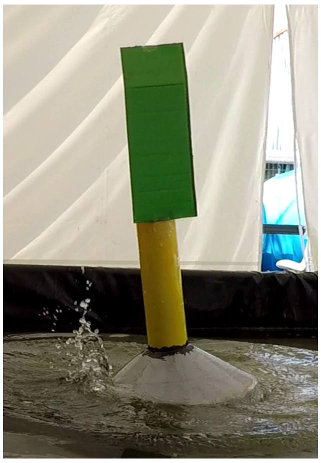

**Figure 4.13:** The GBF returns to its upright position and causes a splash at the back.

Based on the water level with respect to the shaft and the inclination of the GBF, the maximum draft of the GBF was estimated. For the most favourable slipway set-up (21 °, -2 cm freeboard and released from the low position), the maximum draft was approximately 17 cm. For less favourable launching conditions, a draft of more than 20 cm was reached.

## 4.5 Concluding remarks

First of all, the physical scale model tests have proven to be very valuable. Not only by reaching the test objectives mentioned in 4.1, but also by getting a better ‘feeling’ for the dynamic behaviour of a floating GBF. The selected parameter to objectively asses the impact of slipway geometry on the GBF dynamics, the GBF rotation, proved to be well chosen based on visual observations. For large GBF rotations, motion amplitudes and the maximum depth reached by the GBF were large, and the splash was big.

This chapter presented the approach, data collection and results for physical scale model tests that can be used to calibrate and validate the mathematical models. Two sets of experiments, (1) free decay tests, and (2) slipway launches were used to calibrate the mathematical models which is done in the next chapter. Also, the slipway launches are analysed and most favourable slipway aspects are determined.

# Chapter 5

# Comparison of theory and reality

Chapter chapter 4 described the experiments performed for calibrating and validating the mathematical models. GBF position and rotation in time was collected from the free decay tests and launch tests, using a submerged and an abruptly ending slipway. For the abruptly ending slipway, the maximum GBF rotation was measured observe the effect of changing freeboard, slipway inclination and initial velocity on GBF dynamics. In this chapter, the mathematical models presented in Chapter 3 are calibrated and validated by comparing them to the physical scale model tests. This chapter aims to answer the subquestion: "How do the mathematical models compare to reality?". This chapter first calibrates the floating equations of motion using the free decay tests. Then, the submerged sliding model is calibrated and last, the full launch process analysed and modelled by combining all mathematical models. To improve the models, an empirical relation is described that relates maximum GBF rotation to slipway properties.

## 5.1 Floating models: free decay models

Using the free decay tests, the damping coefficient was determined. In the tests, the rigid body was displaced in one axis direction with an initial displacement, and suddenly released. The damping from the free decay tests was considered to be most realistic despite scale effects because they consist of both radiation and viscous damping, where the formulas from literature or software programs are often limited to one of the two. More information about the scale model and the testing facility was presented in Chapter 4.

### 5.1.1 Non-linear damping

The transient behaviour of the moving structure was recorded and the damping coefficient and natural period was calculated from the resulting data. Vibrations in a free decay test with linear damping are mathematically given by:

$$z(t) = z_a e^{-\nu t} \cos \omega_n t \tag{5.1}$$

Comparing the measured data to the above equation, which is done in Figure 5.1 and 5.2 gives more insight into non-linearity of damping. The above equation assumes linear damping, as was done in the mathematical models (i.e. the equations of motion for a floating GBF). From the free decay test, the non-dimensional damping coefficient $\kappa$ is given by (Journée & Massie, 2001):

$$\kappa = \frac{1}{2\pi} \ln \left\{ \frac{z(t)}{z\left(t + T_z\right)} \right\} = c \cdot \frac{\omega_n}{2k} \tag{5.2}$$

in which $z(t)$ and $z(t + T_z)$ are two successive peaks, $T_z$ is the natural period, $c$ is the damping coefficient that can be used in the equations of motion, $\omega_n$ is the measured natural frequency and $k$ is the spring coefficient. The damping coefficient used in Equation 5.1, $\nu = \kappa\omega_n$ in which $\omega_n = \frac{2\pi}{T_z}$. Calibration of the natural period can be done by adjusting the spring coefficient or the added mass (added inertia for pitch). For no particular reason, the spring coefficient calculated mathematically is chosen to be fixed so the added mass was calibrated using:

$$m_a = \frac{k}{\omega_0^2} - m, \tag{5.3}$$

in which $m_a$ is added mass or inertia, $k$ is the calculated spring stiffness and $m$ is the structure's own mass or moment of inertia. In Figures 5.1 and 5.2, damping seems to be non-linear, since it appears to depend on the amplitude of the oscillations. The peaks of the theoretical solution, which were plotted using the average damping value over all the peaks, do not match the measured results for very large or small amplitudes. This is an indication of non-linear damping. Damping does not only depend on velocity only (as is the case in linear damping), but also on the amplitude of the oscillations. De Silva (2005) defined amplitude-dependent damping as a "nonlinear form of damping where its value depends on the amplitude but not on the frequency of motion." This can be caused by quadratic behaviour of viscous damping (Avci, 2016).

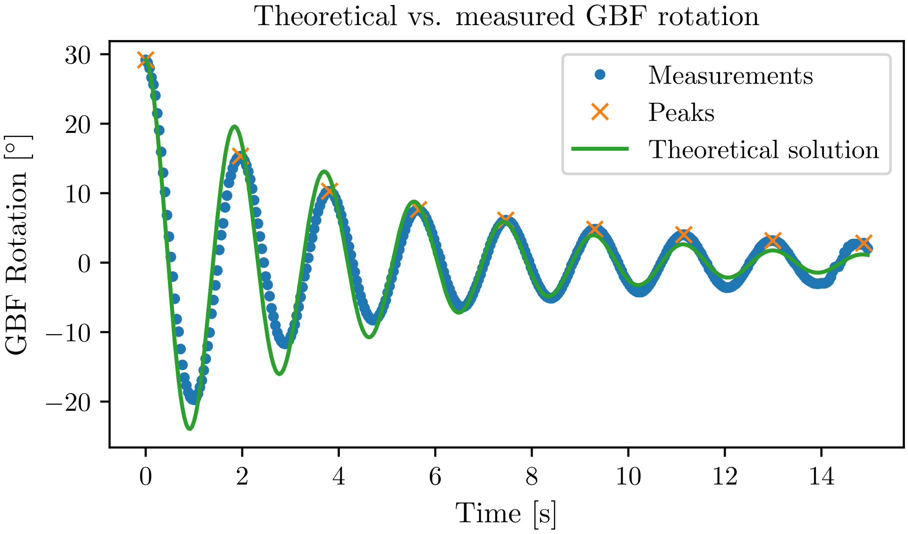

**Figure 5.1:** Measured data compared to the theoretical solution plotted using Equation 5.1 with the mean period ($\omega_{n,\varphi} = 3.38$ rad/s) and mean damping coefficient ($\kappa_\varphi = 0.06$) calculated using the peaks.

**Table 5.1:** The non-dimensional damping coefficient, $\kappa$, natural period, and natural frequency measured from the free decay test for pitch motions. The values were measured between each of the successive peaks (n=8). The damping coefficient $c_\varphi$ is determined using Equation 5.2 and scaled to the 1:1 dimensions of the GBF with a scaling factor of $\lambda^{4.5}$

| $\kappa_\varphi$ [-] | $T_{n,\varphi}$ [s] | $\omega_{n,\varphi}$ [rad/s] | $c_\varphi$ (scaled) [Nm/rad/s] |
|---|---|---|---|
| 0.102 | 1.965 | 3.197 | 1.88E+08 |
| 0.064 | 1.845 | 3.406 | 1.10E+08 |
| 0.047 | 1.845 | 3.406 | 8.12E+07 |
| 0.035 | 1.805 | 3.481 | 5.97E+07 |
| 0.038 | 1.845 | 3.406 | 6.53E+07 |
| 0.028 | 1.845 | 3.406 | 4.89E+07 |
| 0.038 | 1.845 | 3.406 | 6.60E+07 |
| 0.019 | 1.885 | 3.333 | 3.33E+07 |

The damping coefficients measured in the free decay tests can be found in Table 5.1 and Table 5.2. Since the damping coefficient was calculated based on two successive peaks, eight damping coefficients were calculated based on the pitch free decay test. In Table 5.1, it can be seen that the damping decreases significantly as the amplitudes get smaller. The same procedure was applied for heave and a similar non-linear damping pattern can be seen in Figure 5.2. In Table 5.2, the calculated damping coefficients for heave can be found.

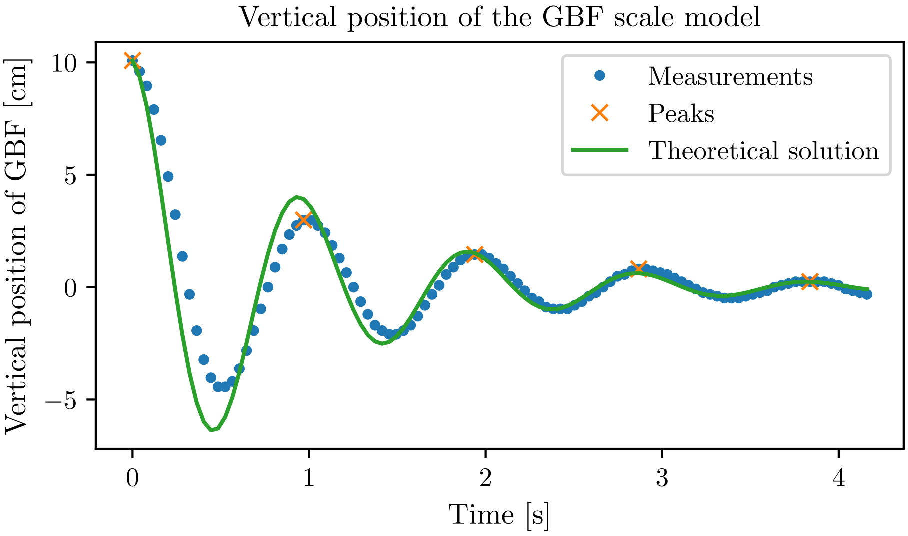

**Figure 5.2:** Measured data compared to the theoretical solution plotted using Equation 5.1 with the mean period ($\omega_{n,z} = 6.55$ rad/s) and mean damping coefficient ($\kappa_z = 0.148$), which was calculated using the peaks.

**Table 5.2:** The non-dimensional damping coefficient, $\kappa$, natural period, and natural frequency measured from the free decay test for heave motions. The values were measured between each of the successive peaks (n=4). The damping coefficient $c_z$ is determined using Equation 5.2 and scaled to the 1:1 dimensions of the GBF with a scaling factor of $\lambda^{2.5}$.

| $\kappa_z$ | $T_{n,z}$ [s] | $\omega_{n,z}$ [rad/s] | $c_z$ (scaled) [N/m/s] |
|---|---|---|---|
| 0.194 | 0.969 | 6.482 | 4.29E+06 |
| 0.115 | 0.969 | 6.482 | 2.53E+06 |
| 0.094 | 0.929 | 6.764 | 1.98E+06 |
| 0.192 | 0.969 | 6.482 | 4.24E+06 |

### 5.1.2 Comparison of results and coefficient calibration

The hydrodynamic coefficients in the equations of motion were computed analytically and numerically (using ANSYS Aqwa) in Chapter 3. In Section 5.1, the hydrodynamic components were computed based on the free decay tests. These three sets of hydrodynamic components were compared to one another by using them in the equations of motion describing a floating GBF derived in 3.17. Using the same initial conditions as in the free decay tests ($\varphi_0 = 29°$ and $z_0 = 10.1$ cm), the results were compared to the measured data from the free decay tests. These comparisons give insight into the validity of the methods used to determine the hydrodynamic components, and into the validity of the derived equations of motion. The equations of motion were solved numerically using 4th order Runge-Kutta method in a mathematical software program called Maple, the input of which can be found in Appendix E.

To analyse the results, the solutions were plotted in Figure 5.3 and Figure 5.4 for pitch and heave respectively. In Section 5.1, it was determined that damping of the system is non-linear. Since the equations of motion derived in Section 3.17 contain linear damping coefficients, a linear damping coefficient needs to be chosen from Table 5.1 and 5.2. Looking at the overall launching process, initial (rotational) displacement is of greatest importance so the damping coefficient for large amplitudes (*first two* peaks in the free decay tests) was used for further analysis.

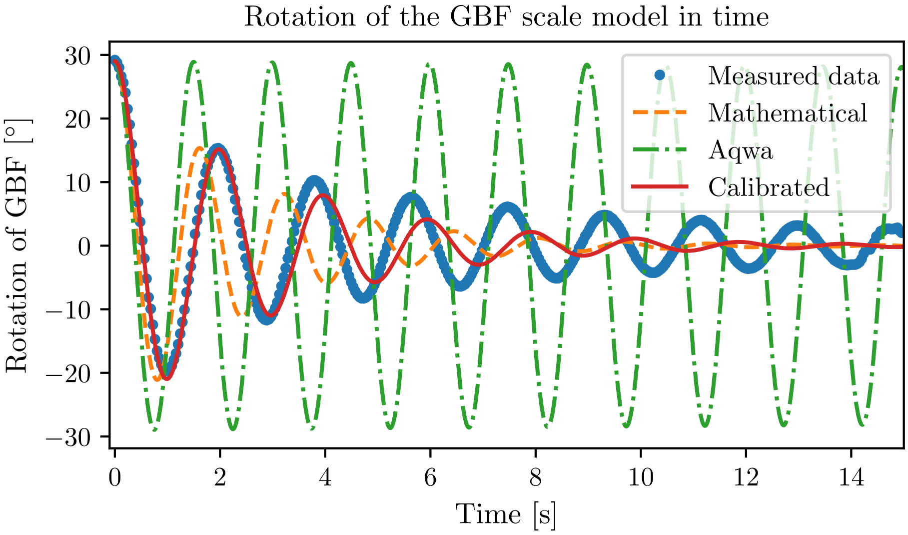

**Figure 5.3:** Results for pitch motions for an initial displacement of 29° plotted using the equations of motion using the hydrodynamic components from Table 3.3 (mathematical and Aqwa) and 5.1 (calibrated). All computed results are compared to the measured data from the free decay tests. The calibrated damping coefficient was determined using the first two peaks, which is why damping is modelled accurately in the first oscillation.

As mentioned in Section 3.6.2, pitch damping is mainly viscous, which was not modelled by ANSYS Aqwa. Looking at Figure 5.3, it can be seen that Aqwa underestimated the damping significantly, agreeing to expectations. The natural frequency from the numerical solution is too high ($\omega_{n,z,sol}$)=3.98 rad/s compared to the measured natural frequency ($\omega_{n,z,sol}$)=3.38 rad/s. This could be due to an overestimation of the spring constant or an underestimation of the added mass. Damping and natural period for calibrated results were modelled accurately for the first oscillation because those were used to determine the damping coefficient. A good match to the calculated results mean that the equations of motions describing pitch motions are correct (at least for the first oscillation).

In contrast to pitch, radiation damping plays an important role in heave motions. Aqwa was able to calculate radiation damping and therefore estimated the heave damping more accurately as can be seen in Figure 5.4. Analytically calculated hydrodynamic components do not differ much from the Aqwa calculations. In comparison to the measured data, damping is underestimated by both models. The natural frequency from the mathematical solution ($\omega_{n,z,sol}$)=6.78 rad/s compares well with the measured natural frequency ($\omega_{n,z,meas}$)=6.55 rad/s. The small difference is caused by an overestimation of the spring constant or an underestimation of the added mass in the mathematical models.

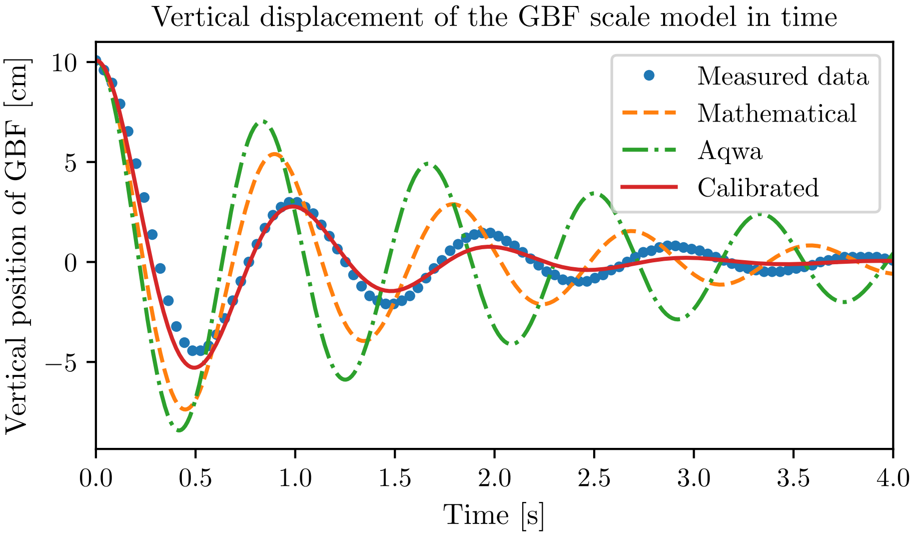

**Figure 5.4:** Results for heave motions for an initial displacement of 10.1 cm plotted using the equations of motion using the hydrodynamic components from Table 3.2 (mathematical and Aqwa) and 5.2 (calibrated). All computed results are compared to the measured data from the free decay tests. The calibrated damping coefficient was determined using the first two peaks, which is why damping is modelled accurately in the first oscillation.

Non-linearity of pitch motions is further analysed here because pitch motions are going to be analysed in the launching tests. In Section 5.1, it was determined that the damping is non-linear when compared to the theoretical solution of a linear spring-damper system. Adjusting the damping coefficient in the equations of motion to a non-linear variable with a dependency on the amplitude improved the model significantly. The damping term in the equation of motion for pitch depends on the amplitude of rotation by: $\varphi(t)^{0.6}$. The exponent of the amplitude was determined simply by a trial-and-error curve fitting exercise. It was not based on any physical process but probably contains many physical phenomenon such as drag on the shaft and other effects related to viscous damping. The results plotted in Figure 5.5 seem to match measured data almost perfectly.

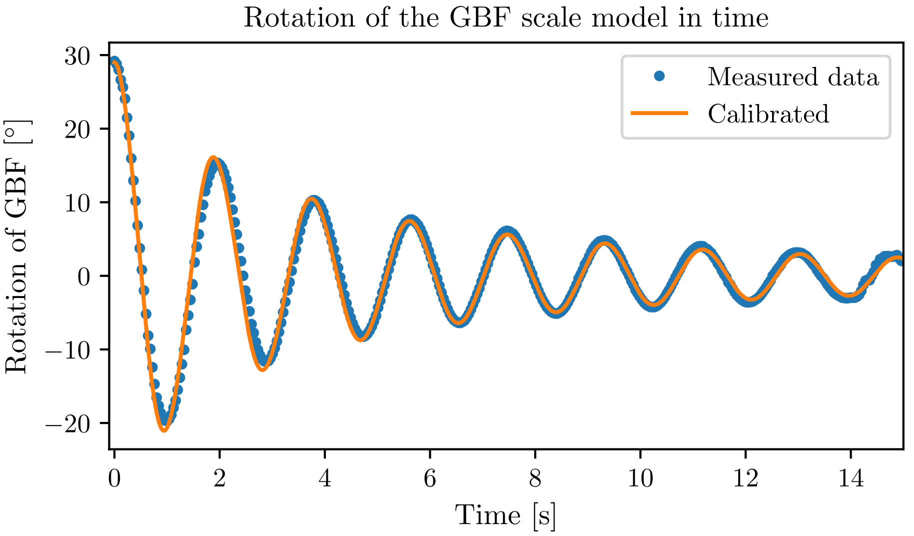

**Figure 5.5:** Results from the free decay tests for pitch compared to the solution of the equations of motion using coefficients calibrated using the experiment and including non-linear damping.

## 5.2 Submerged sliding model

The variant of a submerged slipway was not been studied in detail because it is of less interest. Nonetheless, a model was developed (force balance) that determines GBF motions for this variant. This section compares the mathematical model which was presented in Section 3.3 to the experiments, which were performed using the scale model, testing facility and slipway set up described in Chapter 4.

GBF velocity in time was used to compare the mathematical results to the experiments. Output of the mathematical model is acceleration, which was converted to velocity by integrating with respect to time. The mathematical model stops when the GBF starts floating, defined when the buoyancy force exceeds the weight of the GBF. Output of the experiments was a dataset of positions of the GBF, one position for each frame in the video file. Pixels were transformed to length measurements using known distances from the video frame (the length of the shaft in this case). Using the difference in the position between two frames, along with the known frame rate, the GBF velocity between all frames was determined.

The results were compared in Figures 5.6 to 5.8. Experimental results show large variation around the actual velocity. This is due to imperfections in the video analysis, since the frame rate in combination with the frame dimension in pixels was not sufficient. For this analysis, a frame dimension of 2704x1520 pixels was used in combination with a frame rate of 59 frames per second. Peaks in the figures occur when the video analysis 'skips' a frame, which might have been caused by editing the video, or when the motion tracking software temporarily failed to find the object to be tracked.

Two parameters in the mathematical models were calibrated: the slipway friction coefficient and the GBF drag coefficient. The slipway friction in the experiment was calculated to be around 0.1. When comparing the mathematical model to the experiments, a drag coefficient of 0.85 instead of 0.6 shows better agreement, which was determined by trial and error. This increase is likely to be caused by the wheels attached to the bottom and imperfections in the surface finishing of the scale model.

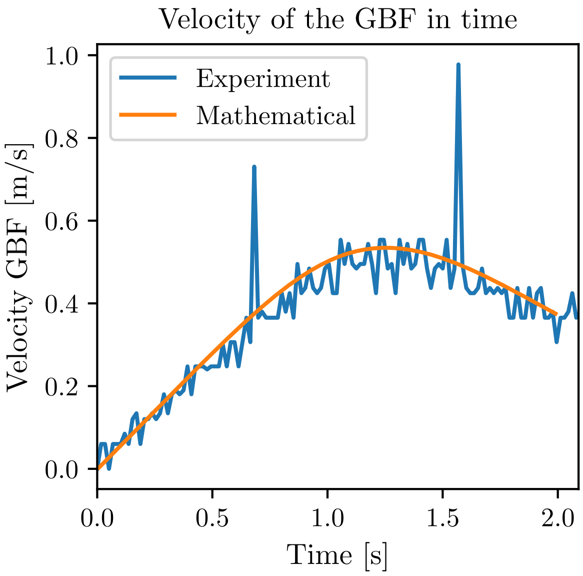

**Figure 5.6:** GBF velocity in time as it slides down a submerged slipway at 9°.

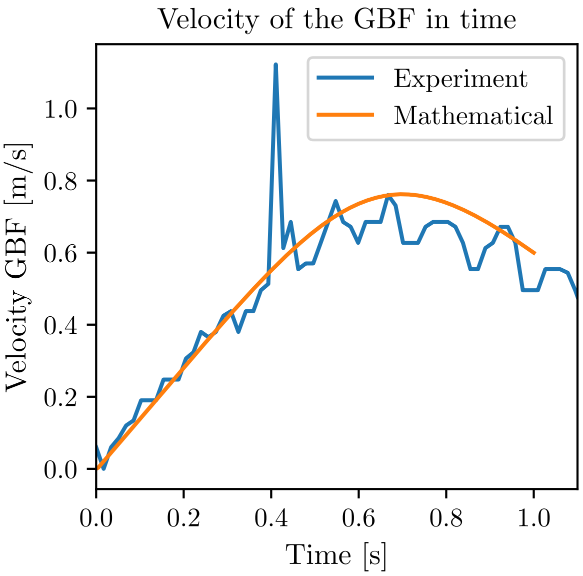

**Figure 5.7:** GBF velocity in time as it slides down a submerged slipway at 14°.

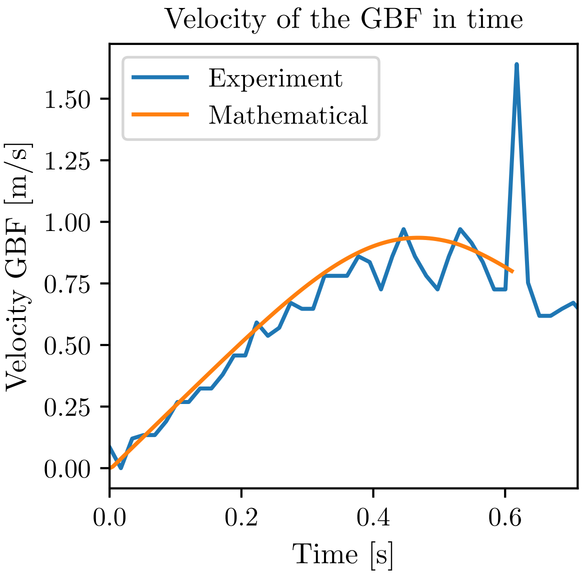

**Figure 5.8:** GBF velocity in time as it slides down a submerged slipway at 21°.

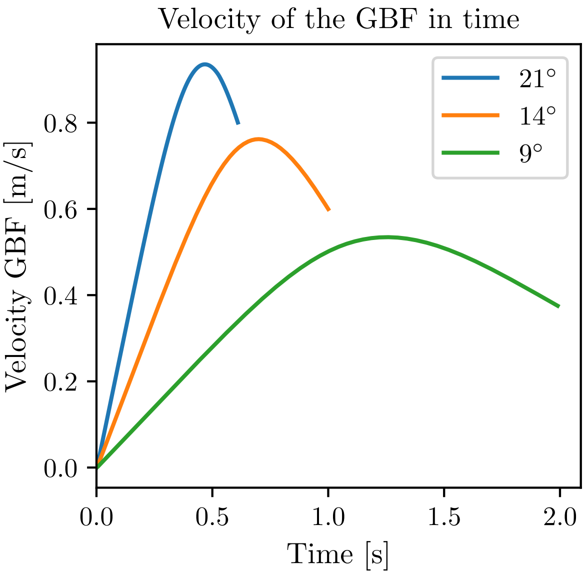

**Figure 5.9:** All calibrated mathematical results plotted in one figure to be able to compare maximum velocities for different slipway inclinations at the 1:100 scale.

Despite inaccuracies in the experiment measurements, calculated velocities compare well to the (averages of the) measured results. For the submerged slipway variant, the maximum GBF velocity was determined for all slipway inclinations, which is shown in Figure 5.9. The mathematical model can also be used to determine GBF accelerations or positions in time.

## 5.3 Full launching process

This section starts with a short analysis of the measured maximum rotations and provides a physical explanation of the results. Then, three mathematical models (sliding, tipping and floating) are combined to reproduce the full launching process. Sliding and floating mathematical models were verified and calibrated separately in the previous section. The equations of motion for tipping connect the two and the full combination of models is compared to launch tests for an abruptly ending slipway in this section. Then, an empirical relation is presented which calculates the maximum GBF rotation for a large range of slipway geometries.

### 5.3.1 Experiment data analysis

In the scale model tests, the maximum rotation reached by a GBF for different slipway endings was determined. This parameter was decided to be a well representation of the severity of the GBF motions during a launch. In Figure 5.10, measured data is plotted to observe general trends. Although a clear general trend can be observed, results differ slightly for different freeboard heights. A low freeboard as well as a steep slipway inclination always resulted in a lower GBF rotation for all set-ups. A high or low velocity does not generate such a general trend, but seems to depend on other factors as well.

For a negative freeboard, a low initial velocity is favourable. Due to the negative freeboard, the GBF was partially submerged when it was released from the low position. For zero freeboard, the results depend on the angle of the slipway. For low angles (9° and 14°), a high velocity was more favourable. The GBF will have less time to rotate during the tipping before it hits the water. At a slipway inclination of 21°, this trend was not observed and a high velocity resulted in a higher GBF rotation. For this slipway inclination, a larger section of the GBF was submerged when it was released. A high velocity resulted in a lower GBF rotation for all experiments performed with a positive freeboard. With a larger distance from the slipway edge to the water, the GBF had more time to rotate before it hits the water, resulting in a larger rotation. A high velocity reduces the time a GBF has to rotate before it hits the water, and therefore performs better in combination with steep slipway inclinations.

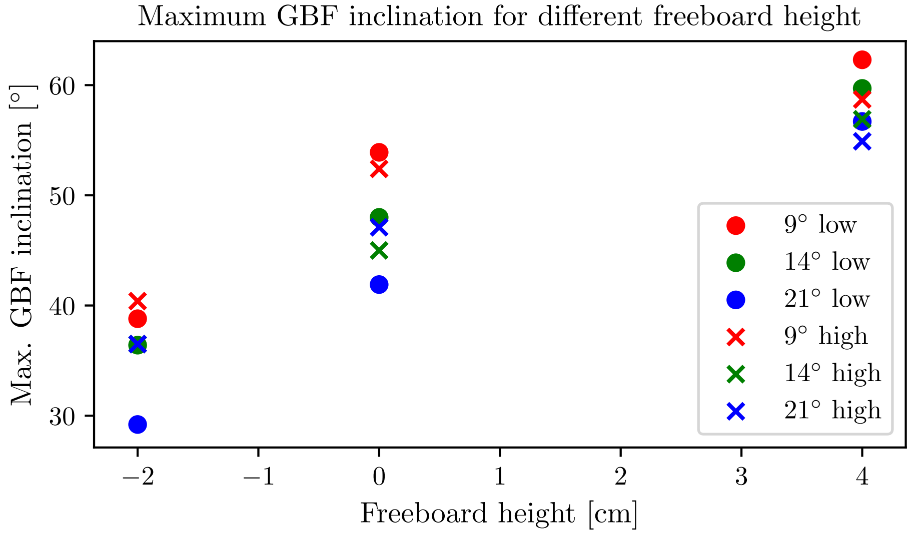

**Figure 5.10:** Maximum rotation for different freeboard heights measured in the launch tests with a slipway inclination of 9°, 14°and 21°, for a high and low velocity. This figure contains the same data as Table 4.2.

In conclusion, it seems that tipping time can be governing (time the GBF has to rotate), in which case a high velocity and a negative freeboard (reducing the tipping time) is better. Otherwise, when tipping time is not governing, the GBF should have a relatively large submerged section (negative freeboard and a steep slipway inclination) and a low velocity performs better since less energy is given to the GBF.

### 5.3.2 Mathematical model

Using the calibrates equations of motion of a floating GBF, the rotation of the GBF measured in the launch experiments was modelled. Together with the slipway force balance, the equations of motions that describe the tipping process were used to determine the rotation and rotational velocity of the GBF without the influence of water. Important to note is that the experiments performed at +4 cm freeboard height were used for comparisons because in these tests, the mathematical models show most agreement physically to the physical models. The tipping equations of motion do not take hydrodynamic forces into consideration, while the floating equations of motion assume a fully floating GBF. Therefore, the tipping equations of motions were used up to the point where the GBF loses contact with the slipway. These (initial) conditions were then used in the floating equations of motion. The experiments were reproduced by the following steps:

1. Solve the force balance for a GBF sliding on the slipway for the high and low position.
    - Input: Slipway inclination, distance GBF center to edge.
    - Output: Velocity parallel to the slipway for (1) high position. This is denoted as $v(0)$ in Table 5.4.

2. Solve equations of motion for the GBF tipping over the edge.
    - Input: GBF properties, slipway inclination, initial velocity (from step 1).
    - Output: Rotational velocity and rotation when the GBF loses contact with the slipway, denoted as $\varphi(0)$ and $\dot{\varphi}(0)$ in Table 5.3 and 5.4.
3. Solve the equations of motion for a freely floating GBF (using calibrated hydrodynamic coefficients and non-linear rotation damping).
    - Input: GBF properties, initial rotational velocity and initial rotation (from step 2).
    - Output: Maximum rotational reached during launch & transient GBF behaviour (similar to scale model measurements for launch tests), denoted as $\varphi_{max}$ in Table 5.3 and 5.4.

As can be seen in Table 5.3 and 5.4, it was found that the general trend of the relationship between slipway inclination, freeboard height and initial velocity can be reproduced using the mathematical model but exact values do not compare well. This is due to the fact that in the experiments, the GBF was already partially submerged during the tipping phase, while the tipping equations of motions did not take water into account. When comparing results from the above procedure to the experiments, as is done in Figure 5.11, it can be seen that for this specific slipway set-up, the mathematical approach was capable of reproducing the experiments quite accurately. However, this was the only set-up at which the maximum GBF rotation was accurately estimated so a further analysis of the experiment data is required to develop an empiric relation between the independent (slipway inclination, freeboard height and initial velocity) and dependent variables (maximum GBF rotation).

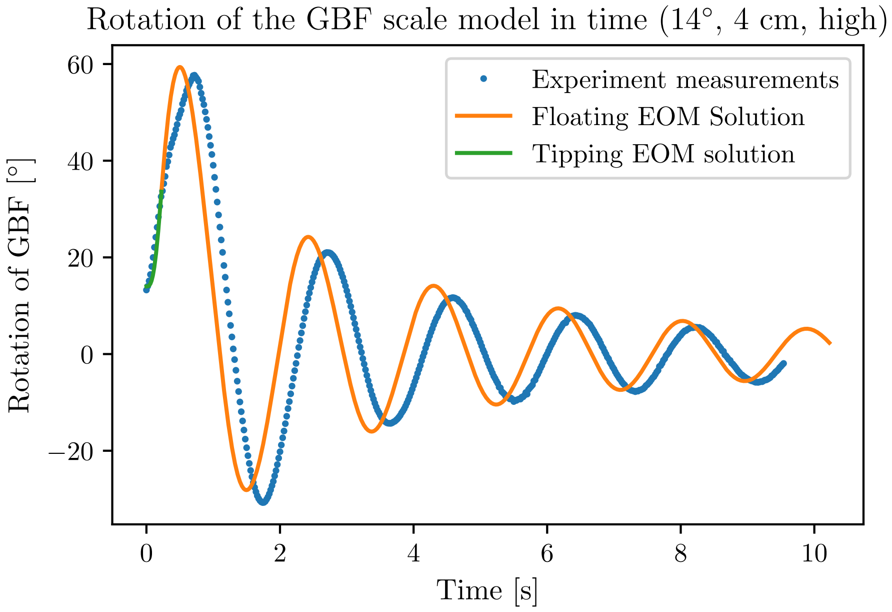

**Figure 5.11:** Combined force balance and equations of motion results compared to experiment measurements for a slipway inclination of 14°, released from the high position with a freeboard of +4 cm.

**Table 5.3:** Mathematical results of the maximum GBF rotations for the low launching position.

| | | Maximum GBF rotation, $\varphi_{max}$ | |
|---|---|---|---|
| Slipway inclination | Initial conditions | Measured | Computed |
| 9° | $\varphi(0) = 1.01$ rad<br>$\dot{\varphi}(0) = 3.17$ rad/s | 62.3° | 74.1° |
| 14° | $\varphi(0) = 0.91$ rad<br>$\dot{\varphi}(0) = 3.24$ rad/s | 59.7° | 70.2° |
| 21° | $\varphi(0) = 0.85$ rad<br>$\dot{\varphi}(0) = 2.96$ rad/s | 56.7° | 65.2° |

**Table 5.4:** Mathematical results of the maximum GBF rotations for the high launching position.

| | | Maximum GBF rotation, $\varphi_{max}$ | |
|---|---|---|---|
| Slipway inclination | Initial conditions | Measured | Computed |
| 9° | $v(0) = 0.384$ m/s<br>$\varphi(0) = 0.77$ rad<br>$\dot{\varphi}(0) = 3.70$ rad/s | 58.7° | 70.1° |
| 14° | $v(0) = 0.608$ m/s<br>$\varphi(0) = 0.59$ rad<br>$\dot{\varphi}(0) = 3.13$ rad/s | 56.9° | 59.4° |
| 21° | $v(0) = 0.822$ m/s<br>$\varphi(0) = 0.57$ rad<br>$\dot{\varphi}(0) = 2.45$ rad/s | 54.9° | 51.3° |

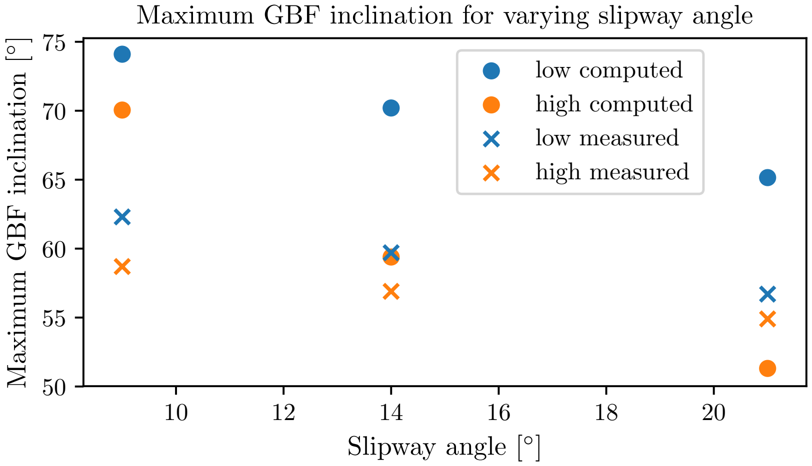

**Figure 5.12:** Predicted and real (measured) maximum GBF rotation for different slipway inclinations. Positive freeboard (+4 cm) set-ups were used for comparison to reduce the impact of hydrodynamics.

In most cases, maximum GBF rotation was overestimated by the mathematical models. The mathematical model is a combination of two models. At the end of the tipping phase, the GBF is still assumed to be moving freely in air. Then, at the next time-step, the GBF is instantly assumed to be fully floating and subject to all hydrodynamic forces. In reality, both processes occur at the same time and the hydrodynamic forces gradually appear as the GBF moves into the water. Therefore, actual rotations are expected to be lower than what is computed. However, in Figure 5.12, it can be seen that for a 21° slipway with a high initial velocity, GBF rotation is underestimated. This happens because in real life, the velocity is damped by the water and since the GBF is slowed down, it rotates further. The mathematical models overestimate the effect of the GBF velocity on the rotation.

### 5.3.3 Empirical fit

Due to the significant difference between the calculated maximum rotation and the measured maximum rotation in the experiments, an empirical formula was derived that relates the GBF angle to freeboard height, slipway inclination, and initial velocity. This was done by plotting the maximum GBF rotation ($\varphi_{max}$) against one of the variables one by one, each time eliminating the dependency on one of the variables. Curves used to fit the data are exponential ($y = a * x^b$) because these types of functions are easy to combine into a clear expression.

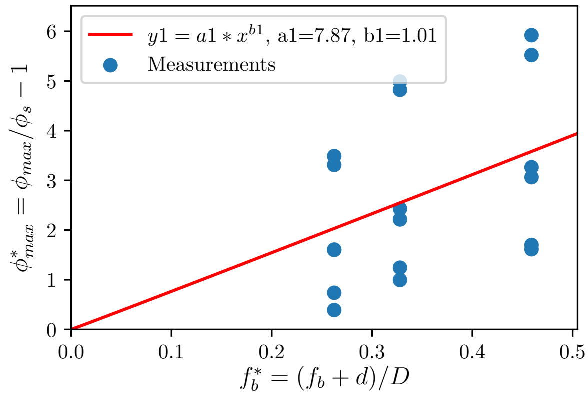

**Figure 5.13:** Measured data plotted against dimensionless freeboard height and fitted by a linear relation.

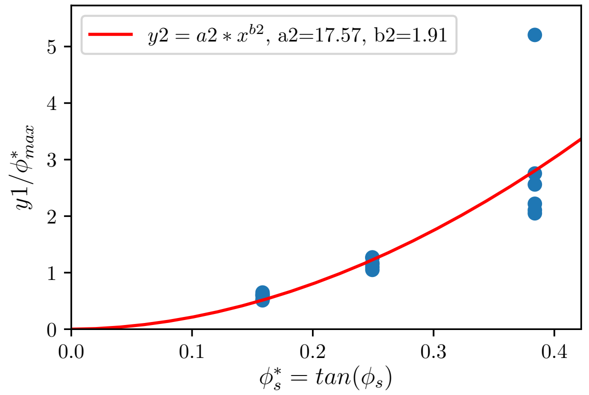

**Figure 5.14:** The inverse of $\varphi_{max}/y1$ plotted against slipway inclination. The relation seems to be linear.

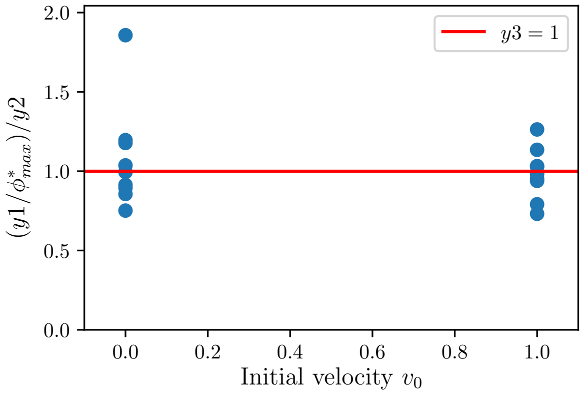

**Figure 5.15:** Plotting the dependency on initial velocity. The impact of the velocity depends on the other slipway properties so no general dependency can be observed.

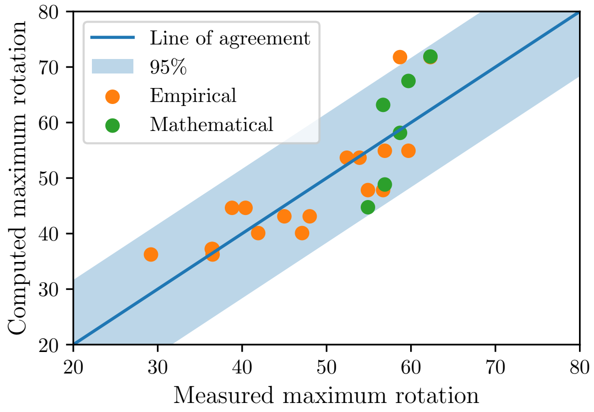

**Figure 5.16:** Computed values using the empirical relation (5.6) and the mathematical models for $\varphi_{max}$ (Section 5.3.2) compared to measured results.

The dependency on freeboard height ($f_b$) was determined first. The data was shifted to the first quadrant and the freeboard height was made dimensionless by:

$$f^*_b = \frac{f_b + d}{D}, \tag{5.4}$$

in which $d$ is the draft and $D$ is the diameter of the GBF base. Draft is added to the freeboard height because aim was to make all values positive and freeboard can never be smaller than the draft because the GBF would float before being released. The freeboard was divided by the GBF diameter to make it dimensionless and physically, $f_b/D$ determines how long the GBF rotates in the air before it hits the water. Next, the maximum GBF rotation was made dimensionless by dividing it by the slipway inclination $\varphi_s$:

$$\varphi^*_{max} = \frac{\varphi_{max}}{\varphi_s} - 1, \tag{5.5}$$

in which $\varphi_s$ is the slipway inclination. A shift was applied (1 was subtracted) to receive a value of zero when the GBF is given no extra rotation with respect to the slipway inclination ($\varphi_{max} = \varphi_s$). Negative values are not possible since the GBF will always have at least the inclination of the slipway. The result of plotting $\varphi^*_{max}$ against $f^*_b$ is shown in Figure 5.13. The data was fitted using $y1 = a1 * x^{b1}$ and the *curve_fit* function from the *scipy.optimize* package in Python, which calculates the values for the coefficients in a specified range to obtain the best fit based on the least squares method. Next, the relation between $\varphi^*_{max}$ and slipway inclination ($\varphi_s$) was determined. The slipway inclination was made dimensionless by using $\tan(\varphi_s)$. To eliminate the dependency on $f^*_b$, $\varphi^*_{max}$ was divided by $y1$, and the inverse was taken since a large slipway inclination results in a *lower* GBF rotation. As seen in Figure 5.14, a trend was fitted using $y2 = a2 * x^{b2}$. Next, This dependency was again eliminated by dividing the y-axis in Figure 5.14 by $y2$ and plotting against GBF velocity $v$ (0 for low, 1 for high). The result in Figure 5.15 shows there is almost no dependency left on initial velocity, so it was fitted using $y3 = 1$. Combining all relations, the maximum GBF rotation can be calculated using four variables; $f^*_b$, $\varphi^*_s$, $v_0$, and $\varphi^*_{max}$. This relation is, after some mathematics:

$$\varphi^*_{max} = \frac{\mathit{a1}\, f_b^{*\,\mathit{b1}}}{\mathit{a2}\, \phi_s^{*\,\mathit{b2}}} \tag{5.6}$$

Using Equation 5.6, the maximum GBF rotation for the range of tested slipway geometries was computed and compared to experiment results in Figure 5.16. Although there is clear scatter around the line of perfect agreement, general trends show good agreement. Although the empirical formula is not necessarily more accurate than the results from the mathematical models, it is applicable for a larger range of input variable and therefore more useful.

## 5.4 Concluding remarks

This chapter aimed answer the subquestion: “How do the mathematical models compare to reality?”. The mathematical models used for the floating phase of the launch seemed to correspond well to experiments after calibration of the hydrodynamic components. The introduction of a non-linear damping coefficient has improved the model and GBF rotations during the free decay tests can be modelled very accurately. The submerged sliding phase was modelled accurately, after a calibration of the hydrodynamic drag coefficient. When simulating a full launch including sliding, tipping and floating phases, the mathematical models have clear shortcomings, which is mainly due to the fact that the equations of motion modelling the tipping phase did not include hydrodynamic forces. An empirical formula was therefore derived that relates the slipway geometry to the maximum GBF rotation. In the last chapter of this thesis in Section 7.3.2, an explanation of how the mathematical models in this chapter can be used to perform a feasibility study, with the help of some exampled. The simple models are useful for making conceptual design but for a more detailed design, more advanced models are needed, such as a Computational Fluid Dynamics model. The next chapter explains the modelling strategy that was used to set up a CFD model, and compares results to the free decay tests.

# Chapter 6

# Computational fluid dynamics

This chapter contains the modelling strategy to develop a CFD model, which was compared to the free decay tests to answer the subquestion: “Can a CFD model be used to model the launching process?”. The feasibility of a CFD program was explored by describing the 3D CFD model strategy and by running it using the same initial conditions used in the physical models (i.e. the free decay tests). The CFD program was run on three different scales to asses scale effects: full-scale (1:1), in model-scale (1:100) and in between (1:10) to verify that it corresponds to expectations qualitatively. The CFD model was made using a coarse mesh with insufficient resolution to accurately calculate forces and motions. Creating a more detailed model would be a study on its own and is outside the scope of this thesis. After a description of the model settings and input data, the output is presented and the chapter ends with a discussion of the results. In this thesis, the CFD software ANSYS Fluent was used. A detailed settings report can be found in Appendix F and more knowledge on the theory behind the CFD program can be found in the ANSYS Fluent Theory Guide (ANSYS inc., 2019).

## 6.1 Computational fluid dynamics

Computational fluid dynamics aim to study details of a particular fluid dynamic phenomena in a controlled environment. CFD simulations provide unequaled insights into the dynamics of fluids (Hickel, 2018). CFD is the rapidly evolving science of numerically solving the equations of fluid motion to produce quantitative predictions and/or analyses of fluid flow phenomena. When used appropriately, CFD is often ideal for parametric studies or flow-physics investigations that would otherwise be impractical or impossible via theoretical or experimental efforts. CFD involves discretizing the spatial domain into a grid or mesh of elements or nodes, and marching the numerical solution forward in discrete time steps. (Kundu, Cohen, & Dowling, 2012)

One important aspect required for a CFD analysis of a 3D floating structure is a dynamic solver that computes the external forces and moments on an object due to the structure-water interaction to determine its motions. Next to that, a dynamic mesh is required for the mesh to move with the moving boundaries. Ansys Fluent is capable of handling both these aspects and was therefore used to perform this CFD analysis. This chapter is organized in same order as the workflow in ANSYS Fluent, which is:

1. draw geometry & generate the mesh;
2. load the mesh and set up Fluent models;
3. run calculations, and;
4. analyse output.

The GBF was modelled as a moving boundary with geometric, mass and moment of inertia properties. If certain models settings are not described in this chapter, then the default program settings or values were used.

## 6.2 Geometry and mesh

The structure was drawn in 3D in DesignModeler, a geometry drawing program available in the ANSYS workbench. The geometry was loaded into a meshing program which generates a mesh around the structure according to the settings provided by the user. Two main considerations were made in this step: mesh quality and the number of nodes and elements. The mesh quality has a direct impact on the quality of the output of Fluent and its ability to accurately model turbulence and other phenomenon and the number of elements and nodes impacts the calculation time significantly. A high element quality in combination with a low number of nodes and elements was aimed for. Detailed information about element quality can be found in Appendix F.

In attempts to decrease the number of nodes and elements, the shaft section of the GBF was not modelled in Fluent. The shaft introduced a large number of elements with low quality due to its relatively small size and round geometry. Modelling a part of the shaft was considered less important than increasing the water basin size or increasing the number of elements around the submerged GBF section. The moment of inertia is a manual input in a later stage of the model set-up, and the moment of inertia of the shaft was included in this number. Removing the shaft in Fluent only impacts the way the geometry looks and the aerodynamic drag it would otherwise cause.

Face meshing was used to create a structured mesh on all outer boundaries as this improves the element quality. A maximum face size of 6 m (in 1:1 scale) was used in a curvature sizing model. This is relatively large but necessary to reduce the number of elements and nodes. It should be noted that the GBF wall boundary, the moving boundary, was meshed using smaller face sizes, large face sizes were only applied in the large volumes of water and air present in the model. The curvature size function examines curvature on edges and faces and computes element sizes on these entities such that the size will not violate the maximum size (defined by the user) or the curvature normal angle (automatically computed by the mesher)(ANSYS inc., 2019). The mesh quality metric was used to asses the mesh quality. Although a quality of 0.4 should at least be aimed for, this could not be reached. Mesh quality ranged from 0.33 in the larger scales to 0.29 in the smaller the scale.

Growth rate was set to 1.15 instead of the default value of 1.20. Although this increases the number of elements, it improved the mesh quality significantly. Growth Rate represents the increase in element edge length with each succeeding layer of elements. For example, a growth rate of 1.2 results in a 20% increase in element edge length with each succeeding layer of elements (ANSYS inc., 2019). The meshing application automatically defeatures small features and dirty geometry according to the default defeature size.

## 6.3 Fluent theory and model set-up

For all flow problems, ANSYS Fluent solves conservation equations for mass and momentum. Additional transport equations are also solved when the flow is turbulent. For this specific problem, certain models in Fluent were used to simulate certain physical processes. The next sections describe the models used in short. For a fully detailed explanation, see Appendix F.

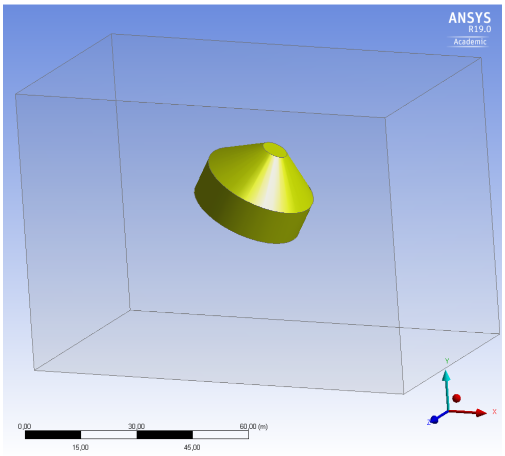

**Figure 6.1:** The geometry used for the CFD analysis of a floating GBF. The shaft was not included in the CFD analysis since this unnecessarily complicates the mesh.

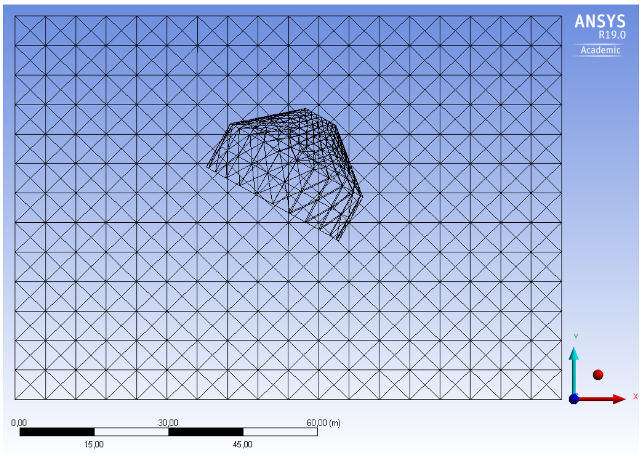

**Figure 6.2:** A side-view of the mesh used for the CFD analysis of a floating GBF. This mesh only shows the mesh on the boundary surfaces, not the internal volume mesh.

### 6.3.1 Models

In ANSYS Fluent, certain models can be switched on to model certain physical phenomenon. The models that were selected for this analysis are described here.

#### Turbulence

For modelling turbulence, the standard $\kappa - \epsilon$ model was used. In the derivation of the $\kappa - \epsilon$ model, the assumption is that the flow is fully turbulent. Standard wall functions were used, and a roughness of 0.05 m was given to all 'wall'-type boundaries.

#### Multiphase flow

Since the problem consisted of two phases (water and air), a multiphase flow model was used to resolve the free surface. The Volume of Fluid formulation in ANSYS Fluent is generally used to compute a time-dependent solution and this formulation was therefore applied with 2 Eulerian phases. Formulation was set to explicit (by default for transient problems), which results in better numerical accuracy compared to the implicit formulation. The time-step size was however limited by a Courant-based stability criterion (ANSYS Inc., 2019). Implicit body force formulation was enabled to calculate forces on the moving body.

### 6.3.2 Boundary conditions

The fluid domain was defined as a rectangular box with 5 'wall'-type boundaries and one pressure outlet (the top boundary). A wall type boundary is automatically identified by Fluent as boundaries through which the fluid transport is resisted. All wall boundary roughness was set to 0.05 m. The moving zone (the GBF) was also defined by 'wall' boundary conditions.

### 6.3.3 Dynamic mesh

The dynamic mesh model in ANSYS Fluent was used to model flows where the shape of the domain is changing with time due to motion on the domain boundaries. The dynamic mesh model allows movement of boundaries of a cell zone (the GBF) relative to other boundaries of the zone (the outer walls), and adjusts the mesh accordingly. The mesh motion was determined based on the solution at the current time (for example, the linear and angular velocities are calculated from the force balance on a solid body), as is done by the six degree of freedom solver in Fluent (ANSYS Inc., 2019).

### Dynamic mesh update settings

Smoothing and remeshing dynamic mesh update methods were used. On zones with a triangular or tetrahedral mesh, the spring-based smoothing method is normally used. When smoothing is used to adjust the mesh of a zone with a moving and/or deforming boundary, the interior nodes of the mesh move, but the number of nodes and their connectivity does not change. In this way, the interior nodes "absorb" the movement of the boundary like a spring. When the boundary displacement is large compared to the local cell sizes, the cell quality can deteriorate or the cells can become degenerate. This will invalidate the mesh (for example, result in negative cell volumes) and consequently, will lead to convergence problems when the solution is updated to the next time step (ANSYS Inc., 2019). To avoid this problem, local cell remeshing was also used. In local cell remeshing, ANSYS Fluent identifies cells based on skewness and size and locally remeshes the cells or faces. The maximum cell skewness is set to 0.9 by default for 3D simulations. Cells with skewness above the maximum skewness are remeshed. Maximum cell skewness was set to 0.7. Parameters for remeshing (minimum and maximum length scale) were defined by parameters of the initial mesh.

### Implicit update

When implicit update is selected, the dynamic mesh is updated during a time step (as opposed to just at the beginning). This capability is beneficial only for applications in which the mesh motion depends on the flow field (for example, cases that use the six degree of freedom solver or involve fluid-structure interaction). For such applications, having the mesh motion updated within the time step based on the converging flow solution results in a stronger coupling between the flow solution and the mesh motion, and leads to a more robust solver run. Implicit mesh updating allows to run simulations that otherwise could not be solved or would require an unreasonably small time step (ANSYS Inc., 2019). A value of 0.9 was used for the motion relaxation, in order to define the relaxation of the motion (that is, displacement of the nodes) during the mesh update. The default value of 0.1 led to numerical instability. Larger values lead to numerical stability at the cost of increasing computational time to reach convergence. It should be noted that a higher value does not affect the solution itself (if converged) but only increases computational time.

### Six degree of freedom solver

ANSYS Fluent's six degree of freedom solver computes external forces and moments (such as hydrodynamic and gravitational forces and moments) on objects that undergo rigid body motion. The solver uses the object's forces and moments to compute the translational and angular motion of the center of gravity of an object (ANSYS Inc., 2019). These forces are computed by numerical integration of pressure and shear stress over the object's surfaces. As part of the solver settings, a set of properties for the moving object were provided to define its overall mass, and rotational inertia according to Table 3.1. The GBF wall boundary was defined as a rigid body with the six degree of freedom solver enabled (which is not done by default). At this stage, the initial conditions need to be provided by defining the center of gravity location with respect to the axis origin, as well as the rigid body orientation. The geometry was drawn as such that the center of gravity of the GBF was placed at the axis origins (0,0,0).

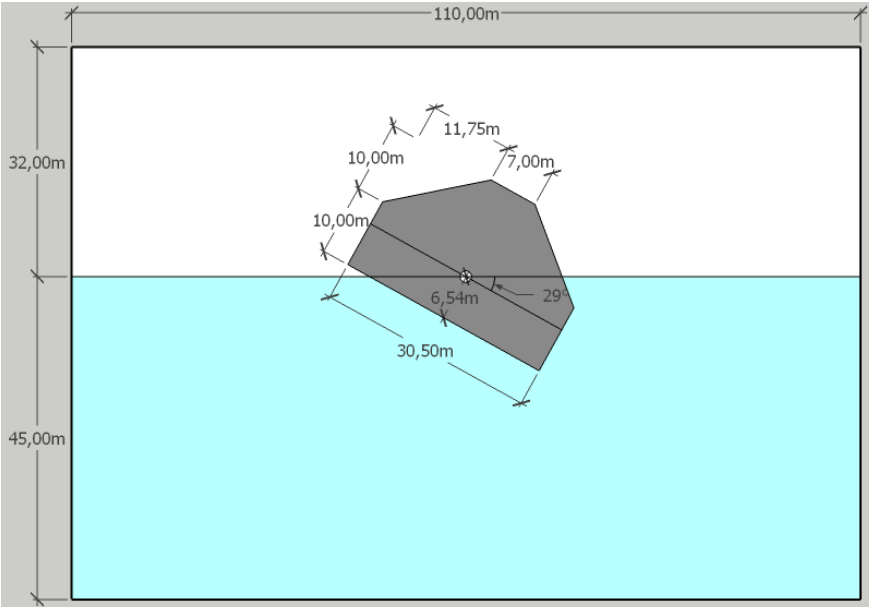

**Figure 6.3:** Geometry, initial conditions and domain size used for the CFD analysis.

## 6.4 Running the calculations

### 6.4.1 Initial conditions

To compare the CFD model to the free decay tests, similar initial conditions were used. For rotation, the initial inclination of the GBF was 29°. For heave, the vertical displacement at the second peak (3 cm in Figure 4.8) was chosen as an initial condition for the CFD model to reduce the size of the motion amplitude but still be able to make comparisons. This was done to be able to reduce the size of the domain (therefore decreasing computation time) and to decrease the impact of the bottom boundary without increasing the domain size. To reduce the amount of computations required, the initial conditions for heave and pitch were used simultaneously in the model. This creates the risk of coupling of pitch and heave motions, which will be discussed in Section 6.5. In ANSYS fluent, the water region must be ‘patched’. This was done by marking a cell region with certain input coordinates and subsequently patching water into it. The initial conditions of the 1:1 scale CFD model are schematized in Figure 6.3.

### 6.4.2 Calculation settings

The calculations were performed three times in three different scales. For each run, the geometry was adjusted according to the required scale. The mesh was recreated using scaled mesh sizes and the mesh was then loaded into the Fluent model. In the fluent model, the dynamic mesh sizing rules and the time-step were scaled. The number of time-steps was the same and therefore, the computation time was approximately equal. The time-step of the calculations was $0.005/\sqrt{\lambda}$ and the maximum number of iterations per time-step was 15. When ANSYS Fluent solves the time-dependent equations using the implicit formulation, multiple iterations may be necessary at each time step. This parameter sets a maximum for the number of iterations per time step. If the convergence criteria are met before this number of iterations is performed, the solution will advance to the next time step (ANSYS Inc., 2019). At 15 iterations per time step, the mesh motion convergence criteria (1E-05) was sometimes (it changes in time) not met, but it came close. When the convergence criteria was set to 1E-04, convergence was reached.

## 6.5 Output and analysis

Positions and rotation of the center of gravity of the six degree of freedom moving structure were used to analyse the behaviour and compare to the physical scale model tests. The same initial conditions for rotation were used in the free decay tests and the CFD model. As mentioned in subsection 4.2.2, less drag (and therefore damping) is expected for larger Reynolds numbers (smaller scales). In Figure 6.4 this trend can be observed for both heave and pitch motions. Damping is largest for a 1:100 scale. As the size of the GBF decreases, viscous and surface tension effects become more important. Although this trend can be explained by a changing Reynolds number, the damping seems to be massively overestimated at this small scale by the CFD model when compared to the physical scale model tests. This could be due to the mesh quality, which was lower for the smaller scales. A lower mesh quality has an impact on the accuracy of the solution. For the 1:1 scale, mesh quality was 0.34, while it was 0.29 for 1:10 and 0.266 for 1:100. The solution calculated at the 1:1 scale should therefore be considered most accurate and reliable.

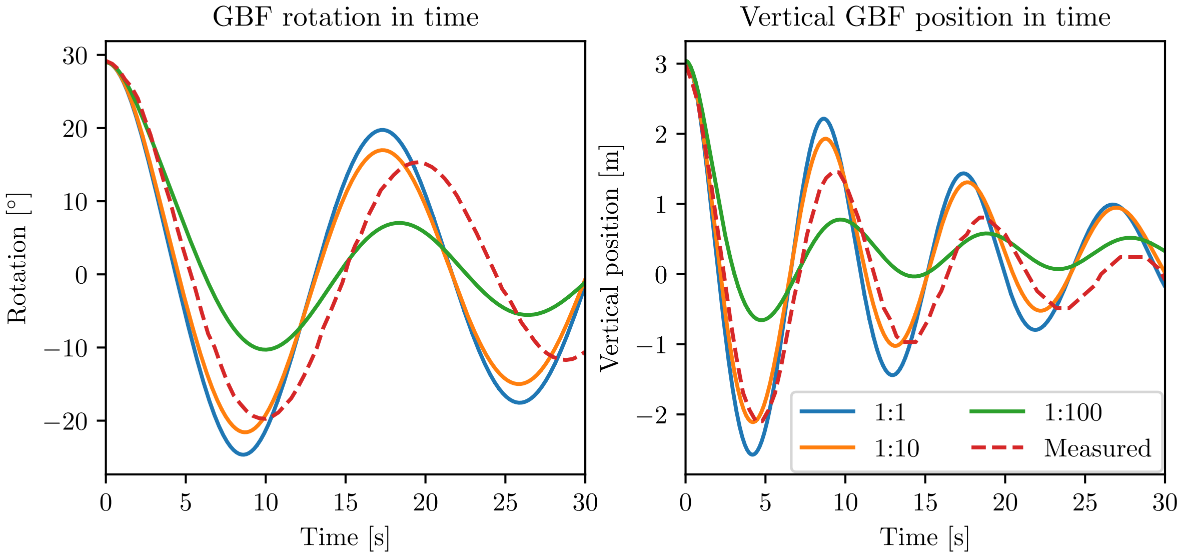

**Figure 6.4:** Vertical position and rotation of the GBF in time computed by the CFD analysis and measured in the free decay tests (real). The model was run at different scales and the results are scaled back to the 1:1 length and time scale to be able to make comparisons. The measured results originate from the physical scale models performed at 1:100 scale.

Comparing results of the CFD model to the free decay tests, motions computed in the CFD model at larger scales correspond well to the motions measured in the free decay tests. Although this is a good sign in terms of feasibility of CFD modelling for this problem, it is quite surprising considering the mesh resolution. Regarding coupling of pitch and heave motions, the natural period for heave is exactly half of the natural period for pitch. Although this would definitely have an impact on the motions, similar natural periods were observed in the physical model tests so coupling of the heave and pitch motions is considered coincidental rather than an effect of coupling.

## 6.6 Model stability and convergence

A test run with more extreme initial conditions was made to check for mesh motion convergence and numerical stability. The new set of initial conditions was based on motions as the GBF falls of the slipway with much larger initial vertical displacement and rotational and horizontal velocity. For this test, a horizontal velocity of 5 m/s was used together with a vertical velocity of -1 m/s, an initial rotation of 20 degrees, and an initial vertical displacement of +10 m. Furthermore, the shaft of the GBF is also included into the analysis. The observed motion displacements and velocity magnitudes are much larger but the model still converged and showed realistic output, a frame of the output video can be seen in Figure 6.5.

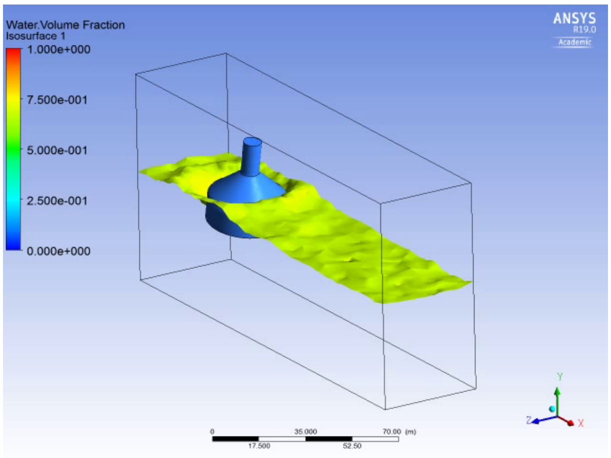

**Figure 6.5:** A frame of the output video produced by the CFD model used with initial conditions that reproduce a launch, i.e. the GBF is dropped from higher with large horizontal and rotational velocity.

## 6.7 Concluding remarks and improvements

This chapter aimed to answer the subquestion: “Can a CFD model be used to model the launching process?”. A practical modelling strategy was developed and tested by comparing it to the free decay tests. First of all, despite the coarse mesh with insufficient quality, the solution converged and showed numerical stability. Depending on the scale, the CFD model shows good quantitatively agreement to physical scale model tests. Large differences between the scales are concerning. A slight difference was expected based on the Reynolds numbers, as mentioned in Section 4.2.2, but the CFD program clearly overestimates the damping at the smallest scale (1:100) due to a low mesh quality. The current CFD model was therefore unable to asses scale effects. When run using more extreme initial conditions and large motion amplitudes, the CFD model was still stable, converged and produced seemingly realistic output.

The CFD model can be extremely valuable. When sufficiently detailed, it can be used to determine pressures on the complete GBF at every time-step. Furthermore, the trajectory can be determined and the accelerations, pressures and forces in all directions are known. The CFD model can therefore be used to asses most requirements related to a launch as described in Section 1.4.3.

The CFD model needs to be improved to be used in a more detailed design phase, but that is outside the scope of this thesis. Improving the CFD model is very time consuming. To be able to investigate effects of changes to the model, the model must be re-run (which takes several hours) for each change. In its current state, the model runs for approximately 10 hours on a standard computer to develop 30 seconds of data (on a 1:1 scale). Nonetheless, four suggestions for the most important improvements are made below:

- The mesh size and quality was insufficient to model the water surface accurately and had a negative impact on the accuracy of the results. Due to limited computational power available, a finer mesh could not be obtained. In addition, a finer mesh leads to a further deterioration of the mesh quality which is unwanted. Most optimal would be the use of an overset mesh. A static background mesh could be used in combination with a moving (overset) component mesh that moves with the moving structure. The main advantage of an overset mesh is that the meh zones do not deform to accommodate moving boundaries, preserving initial mesh quality. Not only does this improve computation time, water surface and GBF motions can be modelled more accurately. This will also help to reach the mesh motion convergence criteria using fewer iterations.

- Since the problem is symmetric, symmetry boundary conditions can be used. Ansys assumes zero flux of all quantities across the boundary. The symmetry plane will essentially split the problem in half, halving the number of nodes and elements, which will decrease computation time.
- The model (in its current state) is not capable of modelling the interaction between the GBF and the slipway. Although this might be possible through User Defined Functions, this has not been implemented for this thesis. These functions can describe certain constraints to the motions of the GBF, which is basically what a slipway does. For now, GBF motions of a freely moving GBF can be modelled, and the initial conditions of the GBF (position, rotation, etc.) need to be defined by the user and can be determined by the simple mathematical models.
- A smaller time-step or more iterations per time step are required to meet convergence criteria based on the Courant Number, which is an input in the explicit multiphase Volume of Fluid model. Motion relaxation also impacts the time required for convergence so these 4 values (time-step, iterations per time step, Courant number and motion relation) should be adjusted to obtain the most efficient model. Many CFD programs have a standard set of recommended criteria, but users must often resort to trial-and-error adjustments to get good results (flow3d.com, 2019). Also, a reasonable number for mesh motion criteria should be used. For CFD, root-mean-square residual levels of 1E-4 are considered to be loosely converged, levels of 1E-5 are considered to be well converged, and levels of 1E-6 are considered to be tightly converged. For complicated problems, however, it's not always possible to achieve residual levels as low as 1E-6 or even 1E-5 so an optimal criteria should determined based on the problem to be modelled. (Kuron, 2015)

The CFD model shows great potential for analysing the gravitational launch of structures. After applying the above improvements, its use would be extremely valuable in the detailed design phase. The next chapter concludes this thesis and contains a discussion, conclusions. Also, recommendations for design purposes and recommendations for future research are given.

# Chapter 7

# Discussion, conclusions and recommendations

This is the last chapter of this thesis and contains a discussion, conclusions and recommendations for design purposes and future research. The method and work done in this thesis is reflected on and limitations are stated in the first section. Section 7.2 states the conclusions for this thesis, answering the research questions and sub-questions. Then, recommendations for design purposes are given to provide a starting point for future research, along with a manual for using the models and a first estimation of launch requirements in Section 7.3. Recommendations for future research are given in the last section, Section 7.4.

## 7.1 Discussion

This section shortly reflects on the used methodology and states the main limitations of this thesis. Reflecting on this thesis, the chosen method was effective to understand and model the process of gravitationally launching GBF's for offshore wind turbines. Although the mathematical models were least accurate (in comparison to the physical and CFD model), they required a thorough the understanding of physical phenomenon that occur during a launch. That knowledge is not necessarily required when performing physical model tests or setting up the CFD model. For setting up the CFD model, knowledge on the software that was used proved to be a lot more valuable.

Limitations of this study are explained below and is split into four subjects: mathematical models, physical models, the CFD model and some overall limitations.

Limitations of the mathematical models:

- Focus was placed on GBF rotation rather than translation. Heave, surge and pitch motions were analysed separately, coupling of motions was not taken into account.
- The mathematical models were not capable of modelling full launch process well. The most critical stage (plunging) was not modelled accurately and required the formulation of an empirical formula.
- The empirical relation does not capture any 'physics' of the process.
- Physical models were still required to verify and calibrate the mathematical models, especially the hydrodynamic components.

- Tipping equations of motion were not validated and calibrated using physical scale models. Tipping and sliding friction might differ and aerodynamic drag was not considered.
- Regarding the applicability of the models for structures of the same shape with different dimensions or for structures with different shapes, the submerged sliding model is valid for structures with the same shape but can be adjusted for different dimensions (diameter, draft, mass). For other structure shapes, the drag coefficients needs to be determined. The equations of motion for tipping are applicable for all other shapes of structures and also different dimensions. The equations of motion for the floating phase can be applied for structures with different shapes and dimensions, although the hydrodynamic coefficients need to be determined. The analytical equations for the hydrodynamic components can only be used for structures with the same shape but with different dimensions such as diameter, draft or metacentric height.

Limitations of physical models:

- The constructed scale model of the GBF showed some differences with the real GBF geometrically. The moment of inertia of the scale model was not verified. Although weight, location of the center of gravity and the size were in agreement with the values used in the mathematical models, this does not necessarily make the moment of inertia correct. Also, the surface of the GBF was uneven.
- The friction coefficient of the sliding mechanism was 0.1, while 0.05 was aimed for.
- Accelerations could not be measured accurately with the current frame rate and size. Positions were measured accurately, and positions can be used to calibrate the mathematical models which can be used to determine acceleration.
- Although the empirical relation is applicable outside the range of tested variables, this study is only based on values within the range of variables. The empirical relation is dimensionless and can be used for structures with different diameters, but this has not been checked. No effect of moment of inertia or metacentric height is included in this relation.

Limitations of the current CFD model:

- The mesh was very coarse and the model was quantitatively inaccurate at small scales.
- No slipway interaction is modelled in the current model.
- A long computation time limits the model's applicability in early design stages.
- Scale effects could not be assessed using the CFD model due to a low mesh quality at the 1:100 scale.

Overall limitations:

- No analysis was performed to investigate the structures with a different geometry (diameter, center of gravity, etc.).
- No analysis of practical issues related to the launching procedure was made.
- No investigation was done on the impact of a cradle and rocker arm on the launching process. For practical reasons, the use of a cradle or rocker arm might be desirable.

## 7.2 Conclusions

The main research question of this thesis is: “How can gravitational launches of gravity based foundations for offshore wind turbines for the Blyth Offshore Demonstrator Project by BAM be modelled using mathematical models?”. To answer this question, three sub-questions are answered:

- Which simple mathematical approaches can be used to describe the kinematics (motions) of a GBF during a launch?
  - The sliding (dry and submerged) phase of a launch was modelled using a force balance. This provided GBF accelerations parallel to the slipway. Tipping and floating phases were modelled using equations of motion. Due to symmetry, the phases were modelled in three degrees of freedom. For the floating equations of motion, hydrodynamic coefficients for added mass, restoring spring force and damping were determined analytically by hand calculations and numerically using the program ANSYS Aqwa.
- How do the mathematical models compare to reality?
  - The force balance for a submerged slipway compared well to the scale model tests after a slight correction of the damping coefficient. The equations of motion for a floating GBF were capable of providing very accurate results after a calibration of the hydrodynamic coefficients. This was not the case for a full launch including sliding, tipping and plunging. General trends of the results were correct but exact values did not compare well. Therefore, an empirical relation was developed that determines the maximum GBF rotation during a launch more accurately for a larger range of slipway variables. Physical models proved to be extremely valuable for developing more insight into the GBF behaviour and for calibrating and verifying the mathematical models.
- Can a CFD model be used to model the launching process?
  - A CFD modelling strategy was proposed and was capable of producing qualitatively correct results that compare well to the physical scale model tests despite a very coarse and low quality mesh. calculations performed at 1:1 showed good agreement to the physical model tests. For small scales, the mesh quality was quite low, which directly impacts the quality of the solution. The solution at large scales is therefore assumed to be more reliable. The current CFD model was only capable of modelling the floating phase of the launch. Convergence and numerical stability was also observed for large motion amplitudes. Significant improvements are required before it can be applied in the detailed design phase.

To answer the main research question, a gravitational launch of gravity based foundations for offshore wind turbine can be modelled by a force balance and equations of motions for the purpose of making a conceptual design. The simple mathematical models (force balance, equations of motion and empirical relations) are sufficient to analyse key differences between slipway alternatives and make choices regarding the conceptual design. Comparisons to scale model tests show good agreement in most cases after a calibration of the hydrodynamic components. Physical models proved to be extremely valuable for developing more insight into the GBF behaviour and for calibrating and verifying the mathematical models. A CFD modelling strategy was proposed and tested but it is not sufficiently simple to be applied in a conceptual design phase to compare many different variants. Improvements of the CFD model would significantly decrease computational time and therefore make a CFD model appropriate in a more detailed design phase to help test technical feasibility of the most optimal variant. The CFD model has the potential to be most flexible, reliable and useful since it can be run for all possible initial conditions and is capable of producing extensive amounts of data, including precise accelerations, GBF trajectory and pressure loads. The major drawback of the current model is a long computation time, the current mesh size and quality, and the lack of interaction with the slipway.

## 7.3 Recommendations for design purposes

When making a conceptual design, the several recommendations can be given based on the research done in this thesis. This section starts with recommendations for the most favourable slipway geometry. Then, recommendations for how the models can be used in the conceptual design phase. Last, a first estimate of the launch requirements is made to make a beginning on checking technical feasibility.

### 7.3.1 Most favourable slipway geometry

Based on the launch tests performed at a 1:100 scale and within the range of tested variables, the most favourable set up is a combination of a steep slipway inclination, low initial velocity and negative freeboard. That is, for a slipway with an abrupt slipway ending, the most favourable in terms of maximum GBF rotation. Most favourable slipway geometry tested had a slipway inclination of 21° and a freeboard of -2 cm, resulting in a maximum GBF rotation of 29°. This was the only variant that did not create a ‘splash’. Least favourable is a 9° slipway inclination in combination with a +4 cm freeboard released from the ‘low’ position, resulting in a maximum rotation of 62°. Although a low freeboard and steeper slipway is always favourable, no such general trend was observed for the initial velocity. For approximately half of the set-ups, a higher initial velocity was beneficial while the opposite is true for the other half. This dichotomy is mainly related to the time a GBF has before it hits the water. When the GBF is already partially submerged when released, a low initial velocity is favourable since the (hydrodynamic) righting moment is activated relatively quickly. Less energy is given to the system and therefore less energy is to be dissipated by GBF motions. When the GBF has more time to travel through the air above the water (as the GBF flies longer, rotation increases) a higher initial velocity is favourable since this reduces the time the GBF flies through the air before hitting the water, activating the righting moment earlier. This was, for example the case for a positive freeboard; a high velocity resulted in a lower GBF rotation for all experiments performed at +4 cm freeboard.

Most optimal would therefore be a submerged slipway ending with a low initial velocity. If a submerged slipway ending is not possible (for cost or constructional reasons), a slipway ending above the water surface (positive freeboard) can best be made with a steep inclination, and the GBF should be given some initial translational speed to reduce the maximum rotation. For a freeboard of 4 cm, most optimal slipway inclination is 21° with the GBF released from the high position, resulting in a maximum rotation of 55°. It should, however, be noted that the highest translational velocity when it hits the water, almost 1 m/s was measured for this variant, which is 10 m/s in 1:1 scale.

### 7.3.2 Using the models

In the initial problem analysis, it was stated that a conceptual design is required to investigate the technical and economic feasibility of a gravitational launch of gravity based foundations for offshore wind turbines. Requirements related to a launch mainly depend on the motions of the

GBF. This study presents models that describe the motions of a GBF subject to a gravitational launch. Figure 7.1 shows how the models can be used as a tool in determining slipway properties in a conceptual design phase. After creating different slipway variants, mainly focusing on varying geometry (slipway inclination, freeboard, etc.), the models can be used to determine the GBF motions, which are required to analyse the requirements for a successful launch. If the variant does not full-fill the requirements, the GBF or slipway can be adjusted and the process is repeated. For example, the decision can be made to make the GBF stronger. After a verification of the variants, they are evaluated based on certain criteria (construction time, risk, etc.) which has not been looked at in this thesis. A decision can then be made for a conceptual design which is used to verify economic feasibility by comparing it to other launching systems (such as immersion structures or submersible vessels). When economic feasibility is verified, the CFD model or physical scale model tests can be applied in a more detailed design loop.

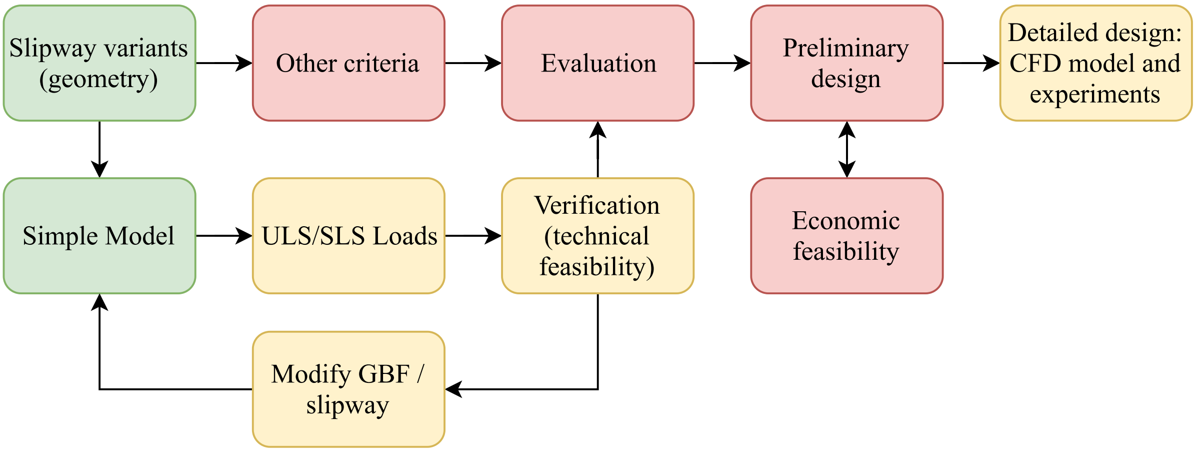

**Figure 7.1:** Steps to come to a slipway design. The color of the boxes indicate the work done in this thesis. Green boxes were investigated completely, orange boxes were touched upon but need expansions. Red boxes were not considered in this thesis.

To model the full launching process for an abruptly ending slipway, the force balance modelling the sliding phase can be used to determine the initial conditions for the equations of motion describing the tipping phase. The initial conditions for the floating phase are then determined by the end of the tipping phase. Equations of motion were used to model the tipping and floating phases separately. Therefore, the time-step at which the conditions are used as initial conditions for the floating phase needs to be determined manually and differ per set up. The plunging phase is modelled best by the scale model tests. To determine kinematics accurately, the sliding & tipping models need to be calibrated (by adjusting the time-step at which the tipping kinematics are transferred as initial conditions to the floating equations of motion) to produce the same maximum inclination measured in the model tests, which can be determined using the empirical formula for a large range of slipway geometries (beyond the range tested variables). The above procedure is summarised in Figure 7.2 and sufficiently accurate to make a first estimate of the requirements which is done in the sections below. All numbers are converted to the 1:1 scale using Table 4.1.

### 7.3.3 Bending moment in the shaft

Bending moment in the shaft can be calculated using the accelerations from the equations of motion. The maximum rotational acceleration of the GBF center of gravity during tipping is 0.217 rad/s$^2$, which is based on the equations of motion solved for Figure 5.11. The theoretical

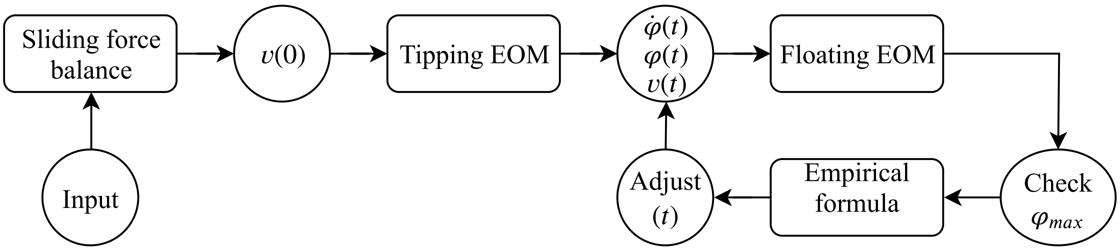

**Figure 7.2:** Manual for using the models. Required input contains GBF and slipway properties. Once the maximum rotation ($\varphi_{max}$) from the floating equations of motion corresponds to the empirical formula, the models can be used to check the requirements.

maximum rotational acceleration of a floating GBF is given by differentiating harmonic motions (not taking into account damping), resulting in:

$$\ddot{\varphi}_{max} = A_{\varphi}\ \omega_n^2, \tag{7.1}$$

in which $\omega_n = 0.338$ rad/s as measured in the free decay tests and $A_{\varphi}$ is the amplitude of the GBF rotation. For the maximum GBF rotation measured in the launch tests of 62° (1.08 rad), the maximum rotational acceleration of the center of gravity is 0.123 rad/s$^2$ for the GBF in the freely floating phase. It therefore seems that the maximum rotational acceleration during the tipping phase is governing. For a rotational acceleration of the center of gravity of 0.217 rad/s$^2$, the unity check for maximum bending moment in the shaft is in the order of magnitude of 0.2 (D. de Jong, 2016). The shaft therefore seems strong enough to resist maximum loads during a gravitational launch due to rotational accelerations.

### 7.3.4 Point load

The point load, $N$, on the slipway edge or GBF base slab in time is solved in the equations of motion for tipping. In combination with the position of the GBF in time, the point load motion over the GBF base slab can be determined. To decrease the point load size, one can increase the number of sliding ways, modify the GBF (attach a skidding beam to distribute the loads) or use rocker arms to create a line-load instead of a point load. During tipping, the point load on the GBF base slab is equal to the GBF self weight for quite some time before it starts decreasing. Although the point load is always equal to the self weight when the tipping phase starts, the slipway geometry can cause the point load to decay faster. Statically, a steep slipway inclination results in a lower point load (trigonometrical). Dynamically, if the GBF has a higher initial velocity, the point load decays much faster than when the GBF has no initial velocity.

### 7.3.5 Hydrodynamic pressures

A first estimate of the pressures on the concrete substructure can be made based on the GBF velocity. It is known that the GBF resists more than 40 m of hydrostatic water pressure during immersion, which equals roughly 400 kN/m$^2$. The maximum velocity at which the GBF hits the water is equal to 9.12 m/s which was the initial condition for a slipway inclination of 21°, with a freeboard of +4 m released from the high position (from Table 5.4). For the fully submerged slipway variant at 21°, the maximum velocity calculated and measured was 9.4 m/s, which is slightly higher. Using Equation 3.27 for drag force with the calibrated drag coefficient of 0.85, and dividing by the surface area, this velocity results in a maximum pressure of 40 kN/m$^2$ when assumed that the full the drag force is caused by positive pressures on the front of the GBF, which is conservative. The pressures on the GBF due to a velocity of 9.4 m/s through the water according to the drag force formula result in a unity check of order of magnitude

0.1 when compared to the GBF resistance to hydrostatic pressures. When using Bernoulli's equation relating velocity to water pressure, $p = \frac{1}{2}\rho v^2$, the unity check was in the same order of magnitude (Muttray, 2019).

### 7.3.6 Trajectory and maximum depth

A safe trajectory consist of two requirements: the GBF does not hit the quay when it returns upright and there is adequate bottom clearance. During none of the performed tests did the GBF hit the quay when returning upright. This would only occur for a very high friction coefficient or if the GBF somehow gets stuck during the launch procedure. The maximum draft can be calculated geometrically using the center of gravity position and GBF rotation during the floating stage. The maximum draft is likely to be reached exactly when the GBF reaches its maximum rotation, which can be determined using the empirical formula. The draft can then be calculated geometrically for a (static) rotation of the floating GBF around its center of gravity and showed good agreement to the draft observed in the scale model tests. For a submerged slipway, the maximum GBF rotation was approximately equal to the slipway inclination. From the physical models, the maximum depth reached by GBF (order of magnitude based on experiments) = 17 m for most favourable launching set-up and ±20 m for unfavourable conditions, with a maximum of around 27 m for the least favourable set-up.

### 7.3.7 Technical feasibility

For some parameters that were thought to be critical, a first estimate is given in the above sections. It seemed that the GBF is strong enough to resist the main forces that occur during a launch. Although no unity check for the point load was presented (this requires a detailed structural analysis of the GBF), the point load can be easily distributed using rocker arms or by increasing the number of sliding ways. Other requirements such as the maximum allowable radiation wave and maximum draft depend greatly on the harbour design, so a conceptual design for a specific harbour locations is required to perform those checks. Nonetheless, the order of magnitude of the expected maximum draft was given.

## 7.4 Recommendations for future research

Other than tackling the limitations stated in the discussions, recommendations for future research were made, which are presented in this section. This section starts with the recommendations for a study that should be conducted after this thesis. After that, recommendations for future research related to the mathematical models, the physical model tests, and the CFD model are given.

To further investigate technical and economical feasibility of gravitational launching methods for GBF's for offshore wind turbine, future research should focus on making a conceptual design for a specific location. By doing this, the impact of practical issues related to the launching procedure should be assessed such as tolerances for the sliding ways, the impact of a launching cradle and rocker arm on the launching process and methods to transfer the GBF from the horizontal position to the inclined slipway. In addition, GBF resistance to large point loads should be calculated to determine the size of the rocker arms and number of sliding ways. A CFD model should be used for a more detailed slipway design to determine all pressures and loads accurately, and loads should be transferred to structure analysis software to perform unity checks.

Recommendations for future research related to the mathematical models should aim to include hydrodynamics into the equations of motion for tipping, although turbulence and free surface effects can only be modelled in combination with a CFD model. Also, verification and calibration of the tipping equations of motion with scale model tests should be done.

Future research related to the physical model tests should be performed in the detailed design phase, by doing scale model tests using the most optimal design for a specific harbor location. It is recommended to calibrate the moment of inertia of the scale model with accurate surface finishing and slipway friction coefficients. Using cameras for data collection was very effective, but a higher frame rate and frame size should be used for calculating accelerations.

Future research on the CFD model should focus on optimising the mesh and analysing the impact of using an overset and background mesh, a symmetry axis, and User Defined Functions for slipway interaction. Time-step size, number of iterations per time-step and convergence criteria need to be optimized to achieve convergence at the largest possible time step.

# Appendices

# Appendix A

# GBF transportation system

In this appendix, a system for the transportation system of GBF's is chosen. This was done using the steps in the standard design approach consisting of an analysis of the problem, presenting different variants as a solution, evaluating the variants and deciding on the best solution.

## A.1 Analysis

In order to allow the GBF to move over the slipway, a transportation system is required. Although this might seem like a practical issue, it also impacts the design of the slipway through the friction coefficient and feasibility of the project as a whole.

The transportation system will be placed on a concrete slipway that might be partially submerged in sea water. It is estimated that the inclination will be between 4 and 15 degrees. The system should support the GBF as described in section 1.2.4. The velocity of the GBF will be in the order of magnitude of meters per second, which is quite fast for such large and heavy structures. Furthermore, the transportation system should take into account the launching process analysed in chapter 1.4.

## A.2 Variants

In this section, possible solutions (variants) are presented and explained.

### Skidding

Skidding systems are used to move extremely heavy loads. Steel skidding tracks need to be placed on the surface and are lined with Teflon pads, on which a skid shoe or skid beam travels. This system is often used for jacket launching as described in Section 1. It is capable of dealing with very large loads and has been proven to work with large and heavy jacket structures.

This is a similar that is used in the ship launching industry, but the process and terminology is a little different. The sliding ways are lined with grease instead of Teflon on which the cradles slide. The cradles are often wedge-shaped to make sure the ship remains horizontal on the slipway. This is mainly done for constructional reasons since ships constructed on top of the sliding ways. Loads are often a lot smaller than during jacket launches because the weight of the ship is distributed over many cradles.

When using this system, two skidding beams need to be cast to the bottom of the GBF. The bottom of the beam will need to be lined with steel. This can be done when casting the base plate in the first production activity. The system of skidding tracks and beams can then be used throughout the whole production process. A set of skidding tracks will need to be

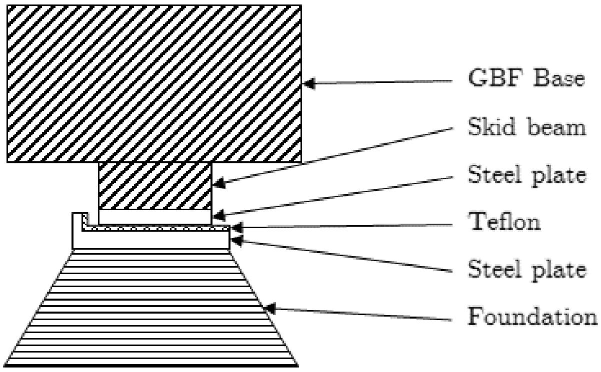

**Figure A.1:** Cross-section of the components needed to transport the GBF by skidding. A skid beam (steel or concrete) is cast in the base slab of the GBF. In case of a concrete skid beam, a steel plate needs to be attached to the bottom. The skidding tracks consist of a steel plate lined with Teflon, supported by a foundation.

constructed. The skidding tracks would consist of a concrete beam topped with steel plates on which Teflon plates are fixed. The concrete beams can be founded by large strip foundations or piles, depending on the soil conditions of the port.

### Steel rollers or skates

Steel rollers or skates are small ‘carts’ with wheels, rollers or a chain of rollers. These carts roll on steel surfaces and are not suitable for rolling on concrete. These carts can either be fixed to the GBF or to the ground. When fixed to the GBF, foundation tracks will need to be constructed on the ground, on which a steel beam or plate is attached. When fixed to the ground the rollers form a conveyor and steel tracks or beams need to be attached to the GBF.

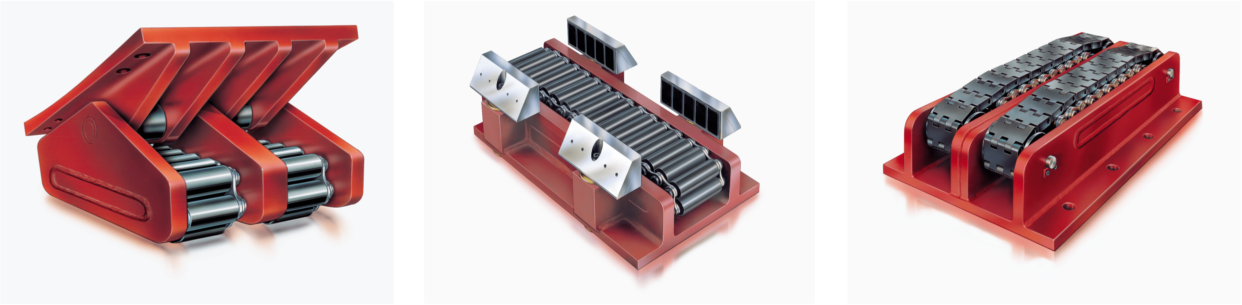

**(a)** Double roller with swiveling top plate.

**(b)** A roller with lateral guiders lined with Teflon pads. Alternatively, wheels can be used instead of Teflon pads.

**(c)** A roller with flat link chain for tracks with small resistance. The localized stresses due to contact between the wheel and tracks are distributed by the flat link chain.

**Figure A.2:** Rollers can be used to transport the GBF on the slipway. The rollers can either be attached to the GBF or to the slipway. Images are from: (Börkey GmbH, n.d.)

When using rollers, the most best solution would be to install rollers on the surface and beams lined with steel on the GBF (similarly to the skidding system).

### Airbags

Cylinder-shaped airbags can be used to transport heavy loads. Airbags have been used to transport ships into the water over a slipway and to transport concrete caissons. Experience with this technique is limited. Airbags are not a highly developed product and have mostly been used in China. Airbags are suitable for transporting structures with high strength and a wide bottom. Lifting capacity is approximately 300 - 500 tonnes per bag, with bag diameters ranging from 1 to 2.5 meters and a maximum length of 25 meters.

**(a)** Airbags transporting a round concrete structure

**(b)** Airbags used to transport a square concrete structure.

**Figure A.3:** Airbags can be used to transport heavy loads such as concrete caissons. Images are from: (Qingdao Eversafe Marine Engineering Co., n.d.).

## A.3 Evaluation

The transport systems are evaluated using a Multi Criteria Analysis (MCA), which is only possible if a low score on one or more criteria does not lead to subordination of a variant. All variants satisfy the requirements. The criteria, an explanation of the criteria weight of the criteria and argumentation for the weight are given in table in Table A.1. The actual MCA then follows in Table A.2.

**Table A.1:** Motivation for the weights of the criteria

| **Criteria** | **Weight** | **Argumentation** |
|---|---|---|
| **Workability** | | |
| Proven technology | **4** | It is advantageous if the transportation mechanism is used before, because it proves its feasibility. This is a very important aspect with regards to the complete research. |
| Risk | **3** | Damage to the GBF or delays in the construction process are regarded as important. Also, if the risk is too high, it might be difficult and expensive to find insurance. |
| **Structural/ design** | | |
| Friction coefficient | **3** | The friction coefficient has an impact on the dynamics of the GBF, low friction is favorable. The friction coefficient might need to be changed in a later stage of this research. Aspects impacting the dynamics of the GBF are important. |
| Engineering difficulty | **1** | A difficult design is more expensive and time consuming, but it is assumed that competent engineers can deal with the issue in later design stages. |
| **Interfaces** | | |
| Substructure | **2** | The magnitude and complexity of the required substructure is important to the overall feasibility of the project. |
| Modification to GBF | **2** | Modifications to the GBF are unwanted but minor modifications to the GBF are so the impact is small. |
| **Economy/sustainability** | | |
| Maintenance | **2** | Maintenance is not very important but needs to be considered. A lot of maintenance is time consuming. |
| Sacrificial elements | **1** | Sacrificial elements are not wanted, but a good variant that requires some sacrificial elements should not be rejected. |

Table A.2: MCA for the transportation system

| Criteria | | Weight | Transport system | | | | | | | | |
|---|---|---|---|---|---|---|---|---|---|---|---|
| | | | Rollers | Score | Value | Skid beam | Score | Value | Airbags | Score | Value |
| **Constructional/workability** | | | | | | | | | | | |
| Proven technology | Has the technology been used to transport structures of similar weight, size and speed? | **4** | Has not been used at high speeds. | -- | -8 | Yes, has been used on barges for jacket launches. | + | 4 | No, structures have been a lot smaller and lighter. | -- | -8 |
| Risk | How high is the risk of something going wrong when using this transportation technique? | **3** | Moderate risk, unevenly positioned rollers cause large vibrations and point loads. Rollers can get stuck. | - | 0 | Low risk, disturbances can be absorbed with by lining material. | + | 3 | According to one of the manufacturers, this technology has not been developed by the industry. | -- | -6 |
| **Structural/ design** | | | | | | | | | | | |
| Engineering difficulty | Is it difficult to design the transport mechanism? | **1** | The rollers cause point loads on the GBF, which | -- | -2 | The tracks and beams need to be even. | - | 0 | Airbags can be designed relatively easily. | ++ | 2 |
| Friction coefficient | Is the friction coefficient low and easily adjustable? | **3** | Not adjustable | - | 0 | Low friction coefficient, can be changed using different materials. | ++ | 6 | Low friction coefficient, but not easily adusted | + | 3 |
| **Interfaces** | | | | | | | | | | | |
| Substructure | What kind of substructure is required? | **2** | Two supporting beams and its foundations. | - | 0 | Two supporting beams and its foundations. | - | 0 | A slab that fully covers and supports the GBF and foundations | -- | -4 |
| Modification to GBF | Does the GBF need to be modified? | **2** | yes, a little | - | 0 | yes, a little | - | 0 | No | ++ | 4 |
| **Economy/sustainability** | | | | | | | | | | | |
| Maintenance | Does the transportation mechanism require a lot of maintenance? | **2** | Rollers require maintenance and many inspections, faulty rollers have serious consequences. | -- | -4 | Skid beam needs to be inspected regularly and regreased if grease is applied. | - | 0 | Bags need to be inspected after every launch for leakages. | + | 2 |
| Sacrificial elements | Are there sacrificial elements? | **1** | Beam under GBF | - | 0 | Beam under GBF | - | 0 | none | ++ | 2 |
| **Total Score** | | | | | **-14** | | | **13** | | | **-5** |
| **Legend** | **Score / risk** | | **Weight** | | | | | | | | |
| | (++) complies / beneficial / none | 2 | small impact | **1** | | | | | | | |
| | (+) just complies / neutral / small | 1 | impact | **2** | | | | | | | |
| | (-) just complies /unfavourable /medium | 0 | noticable impact | **3** | | | | | | | |
| | (--) doesn't comply / bad / large | -2 | very big impact | **4** | | | | | | | |

## A.4 Decision

Based on the MCA, a skidding system is the best transporting mechanism to transport the GBF over the slipway is a set of skidding tracks and beams. This variant scored 13 points, which is high compared to the rollers (-14 points) and airbags (-5 points). In terms of cost, the variants do not differ significantly. Airbags might be cheap in the transportation mechanism itself, but the required substructure is significantly bigger and therefore more expensive. Therefore, the choice is made to proceed the research using a set of skidding tracks and beams lined with Teflon.

### Friction Coefficient

According to Campbell, Kong, and Manning (1990), the friction coefficient between PTFE and steel depends on many factors, including:

- Contact pressure
- Speed of travel
- Roughness of the mating surface
- Length of the travel path
- Dimpling and lubrication
- Eccentric loading
- Temperature
- Creep
- Type of PTFE
- Attachment of the PTFE to the backing plate
- Surface contamination
- Load and travel history
- Specimen size
- Wear

In laboratory experiments, the friction coefficient was found to vary between 0.001 and 0.07, for tests done as 20°C for changing pressure, travel speed, and roughness of metallic (Campbell et al., 1990). The friction coefficient can easily be changed by changing the number of Teflon plates, which increases the pressure on the plates and decreases the coefficient of friction. Also, the steel roughness can be changed. Coefficient of friction claimed by manufacturers vary between the similar ranges.

# Appendix B

# Mathematical models

This appendix contains the Python and Maple code used to solve the mathematical models.

## B.1 Force Balance Dry

```
import numpy as np
import math as math
import matplotlib.pyplot as plt
import matplotlib

#s=scale, m=Mass [kg], D=GBF diameter, g=gravity, c=Friction coefficient
s=100
m=7000000/s**3
D=30.5/s
g=9.81
c=0.05

#radmin is the minimum angle for movement
radmin=math.degrees(np.arctan(c))
alphamin=math.ceil(radmin)
K=30
M=m*g
a=np.zeros(K)

#Determine acceleration for every degree of inclination (from 0 to 29 deg)
for i in range (K):
    alpha=math.radians(i)
    N=M*np.cos(alpha)
    W=c*N
    F=M*np.sin(alpha)
    Ftot=F-W
    a[i]=Ftot/m

#array a is now the GBF acceleration for 30 different slipway inclinations
```

## B.2 Partially submerged force balance

```
import csv
import numpy as np
import matplotlib
import matplotlib.pyplot as plt
from matplotlib import animation
from matplotlib.patches import Rectangle
from matplotlib.patches import Circle
from matplotlib.patches import Polygon
from matplotlib.lines import Line2D
import math as math

# m=Mass [kg], r=radius of base plate [m], g=gravity, c=Friction
    coefficient, D=drag coefficient,
# rho = density [kg/m3], alpha = angle of slipway, vzero = initial
    velocity,
# t=time step [s]
#S=SCALE
s=1
rho=1000
m=7000000/s**3
r=15.25/s
aw=np.pi*r**2
hcg=6.54/s        #height of COG w.r.t.bottom
q=np.sqrt(r**2+hcg**2)
hd=m/rho/aw       #draft
g=9.81
c=0.05
D=0.60
M=m*g
alpha=np.radians(5)

#initial velocity
vzero=0/np.sqrt(s)
xzero=0

#T is timestep
T=0.05/np.sqrt(s)
n=1000
z=-T
phi=np.zeros(n)
theta=np.zeros(n)
V=np.zeros(n)
C=np.zeros(n)
B=np.zeros(n)
t=np.zeros(n)
h=np.zeros(n)
x=np.zeros(n+1)
a=np.zeros(n+1)
```

```
v=np.zeros(n+1)
v[0]=vzero
xc=np.zeros(n)
yc=np.zeros(n)
a[0]=g*np.sin(alpha)-c*g*np.cos(alpha)

#Determine acceleration for every degree of inclination
for i in range(n):
    t[i]=(i*T)
    v[i+1]=v[i]+0.5*(a[i-1]+a[i])*T #TODO: check formulas
    x[i+1]=x[i]+0.5*(v[i]+v[i+1])*T #TODO:check if it should be v[i
        +1]*0.5*T
    h[i]=x[i]*np.tan(alpha)
    if (h[i]-r*np.sin(alpha))<hd:
        xc[i]=x[i]*np.cos(alpha)
        yc[i]=-x[i]*np.sin(alpha)
        if x[i]>2*r:
            V[i]=(np.pi*r**2)*(h[i]-r*np.sin(alpha))
        if x[i]<2*r:
            if x[i]<r:
                if i==0:
                    V[i]=0
                else:
                    theta[i]=np.arccos((r-x[i])/r)
                    V[i]=(h[i]*r**2)*(3*np.sin(theta[i])-3*theta[i]*
                        np.cos(theta[i])-np.sin(theta[i])**3)/(3*(1-np
                        .cos(theta[i])))
            if x[i]>r:
                theta[i]=np.pi-np.arccos((x[i]-r)/r)
                V[i]=(h[i]*r**2)*(3*np.sin(theta[i])-3*theta[i]*np.
                    cos(theta[i])-np.sin(theta[i])**3)/(3*(1-np.cos(
                    theta[i])))
        B[i]=V[i]*rho*g
        N=(M-B[i])*np.cos(alpha)
        W=c*N+0.5*rho*D*v[i]**2*h[i]*2*r
        F=(M-B[i])*np.sin(alpha)
        Ftot=F-W
        a[i+1]=Ftot/m
        phi[i]=alpha
        nick=t[i]
    else:
        yc=yc[:i-1]
        xc=xc[:i-1]
        v=v[:i-1]
        x=x[:i-1]
        phi=phi[:i-1]
        t=t[:i-1]
        end=i-1
        break
```

## B.3 Tipping Equations of Motion

```
> restart;
> s := 1 :
> with(plots) :
> kappa := phi(t) :
> a := sin(kappa) − w·cos(kappa) : b := cos(kappa) + w·sin(kappa) :
> EOM1 := m·diff(x(t), t, t) = N·a; EOM2 := m·diff(y(t), t, t) =−m·g + N·b; EOM3 := Ix
      ·diff(phi(t), t, t) = N·(−a·y(t) + b·x(t));
```

$$EOM1 := m\left(\frac{d^2}{dt^2}x(t)\right) = N\left(\sin(\phi(t)) - w\cos(\phi(t))\right)$$

$$EOM2 := m\left(\frac{d^2}{dt^2}y(t)\right) = N\left(\cos(\phi(t)) + w\sin(\phi(t))\right) - m\,g$$

$$EOM3 := Ix\left(\frac{d^2}{dt^2}\phi(t)\right) = N\left(-\left(\sin(\phi(t)) - w\cos(\phi(t))\right)y(t) + \left(\cos(\phi(t)) + w\sin(\phi(t))\right)x(t)\right) \quad \textbf{(1)}$$

```
> z(t) := −x(t)·tan(kappa) + (h[cg])/cos(kappa) :
> diff(y(t), t, t) = diff(z(t), t, t) :
> p(t) := solve(EOM2, N) :
> N := algsubs(diff(y(t), t, t) = diff(z(t), t, t), p(t)) :
> Ix := 1500000000/s^5 : g := 9.81 : m := 7000000/s^3 : h[cg] := 6.54/s : alpha :=
      convert(9 degrees, radians) : w := 0.05 : v := 0.0 :
> ics := x(0) = 0.0, phi(0) = alpha, y(0) = 0, D(x)(0) = v· cos(alpha), D(y)(0) =−v·sin(alpha),
      D(phi)(0) = 0 :
> with(ArrayTools) : Z := Array([ ]) :for i from 0 by 0.01/sqrt(s) to 5/sqrt(s) do Append(Z, i) end
      do: Z :
> dsn2 := dsolve([EOM1, EOM2, EOM3, ics], type = numeric, method = rkf45, output = Z) :
> SOL := dsn2[2, 1] :
>
> csvfile := FileTools :-JoinPath(["data2.csv"], base = homedir) :
> Export(csvfile, SOL) :

>
>
```

## B.4 Floating Equations of Motion

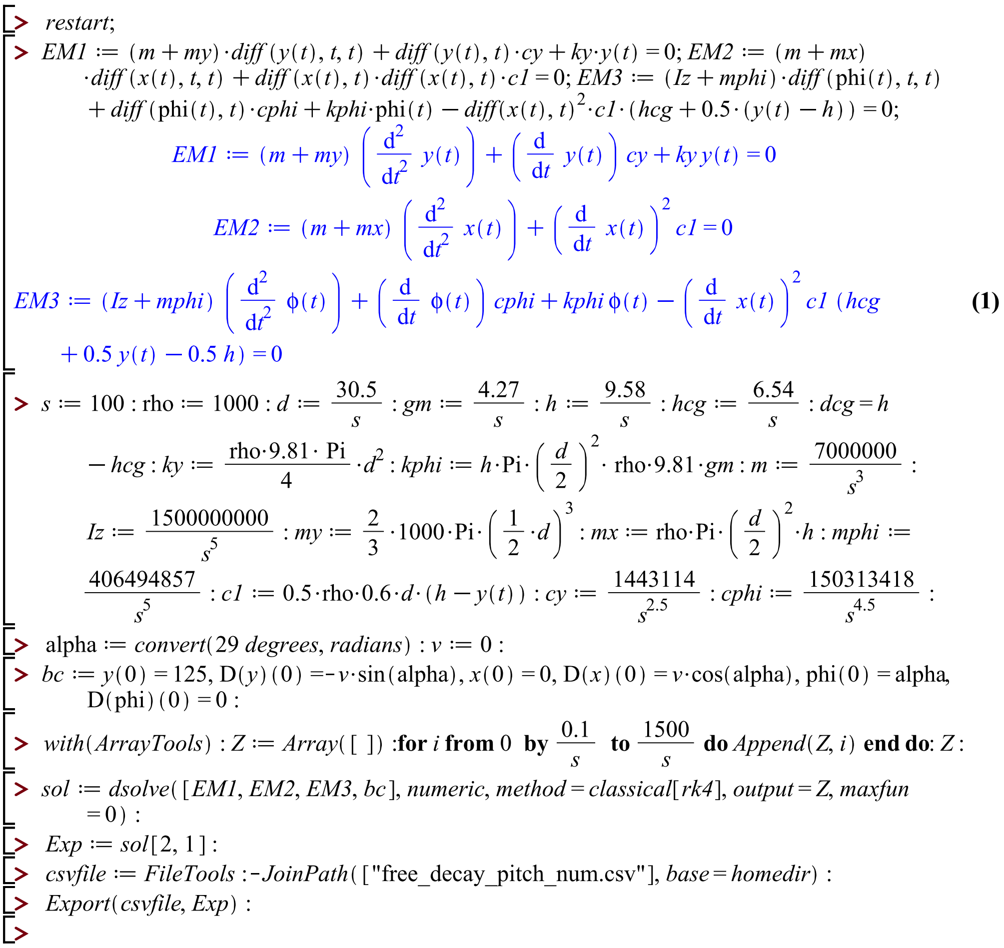

$$> \ restart;$$

$$> \ EM1 := (m+my)\cdot diff(y(t),t,t) + diff(y(t),t)\cdot cy + ky\cdot y(t) = 0;\ EM2 := (m+mx)\cdot diff(x(t),t,t) + diff(x(t),t)\cdot diff(x(t),t)\cdot c1 = 0;\ EM3 := (Iz+mphi)\cdot diff(\mathrm{phi}(t),t,t) + diff(\mathrm{phi}(t),t)\cdot cphi + kphi\cdot \mathrm{phi}(t) - diff(x(t),t)^2\cdot c1\cdot(hcg + 0.5\cdot(y(t)-h)) = 0;$$

$$EM1 := (m+my)\left(\frac{d^2}{dt^2}\,y(t)\right) + \left(\frac{d}{dt}\,y(t)\right) cy + ky\,y(t) = 0$$

$$EM2 := (m+mx)\left(\frac{d^2}{dt^2}\,x(t)\right) + \left(\frac{d}{dt}\,x(t)\right)^2 c1 = 0$$

$$EM3 := (Iz+mphi)\left(\frac{d^2}{dt^2}\,\phi(t)\right) + \left(\frac{d}{dt}\,\phi(t)\right) cphi + kphi\,\phi(t) - \left(\frac{d}{dt}\,x(t)\right)^2 c1\,(hcg + 0.5\,y(t) - 0.5\,h) = 0 \qquad \mathbf{(1)}$$

$$> \ s := 100 : \mathrm{rho} := 1000 : d := \frac{30.5}{s} : gm := \frac{4.27}{s} : h := \frac{9.58}{s} : hcg := \frac{6.54}{s} : dcg = h - hcg : ky := \frac{\mathrm{rho}\cdot 9.81\cdot \mathrm{Pi}}{4}\cdot d^2 : kphi := h\cdot\mathrm{Pi}\cdot\left(\frac{d}{2}\right)^2\cdot \mathrm{rho}\cdot 9.81\cdot gm : m := \frac{7000000}{s^3} : Iz := \frac{1500000000}{s^5} : my := \frac{2}{3}\cdot 1000\cdot\mathrm{Pi}\cdot\left(\frac{1}{2}\cdot d\right)^3 : mx := \mathrm{rho}\cdot\mathrm{Pi}\cdot\left(\frac{d}{2}\right)^2\cdot h : mphi := \frac{406494857}{s^5} : c1 := 0.5\cdot\mathrm{rho}\cdot 0.6\cdot d\cdot(h - y(t)) : cy := \frac{1443114}{s^{2.5}} : cphi := \frac{150313418}{s^{4.5}} :$$

$$> \ \mathrm{alpha} := convert(29\ degrees, radians) : v := 0 :$$

$$> \ bc := y(0) = 125, \mathrm{D}(y)(0) = -v\cdot\sin(\mathrm{alpha}), x(0) = 0, \mathrm{D}(x)(0) = v\cdot\cos(\mathrm{alpha}), \mathrm{phi}(0) = \mathrm{alpha}, \mathrm{D}(\mathrm{phi})(0) = 0 :$$

$$> \ with(ArrayTools) : Z := Array([\ ]) : \mathbf{for}\ i\ \mathbf{from}\ 0\ \mathbf{by}\ \frac{0.1}{s}\ \mathbf{to}\ \frac{1500}{s}\ \mathbf{do}\ Append(Z, i)\ \mathbf{end\ do} : Z :$$

$$> \ sol := dsolve([EM1, EM2, EM3, bc], numeric, method = classical[rk4], output = Z, maxfun = 0) :$$

$$> \ Exp := sol[2, 1] :$$

```
> csvfile := FileTools:-JoinPath(["free_decay_pitch_num.csv"], base = homedir) :
> Export(csvfile, Exp) :
>
```

## Appendix C

# Analytical calculation of hydrodynamic components

This appendix explains how the hydrodynamic components for the equations of motion describing the floating phase were calculated analytically based on literature. The coefficients of the matrices were determined analytically using existing (adapted) formulas. It should be noted that many components are in fact frequency- or amplitude- dependent. During the floating stage of the launch, the structure moves at its natural frequency so when necessary, the (undamped) natural frequency was used to determine the frequency dependent coefficient. The analytical formulas from literature sources are often based on experiments rather than being derived from theoretical mathematical formulations.

## C.1 Mass and added mass

The mass and moment of inertia of the GBF itself were defined in Section1.2.4. The added mass is different in each degree of freedom. According to Barltrop (1998), added mass can be approximated by spherical volumes around the submerged section of the floating structure, as visualised in Figure C.1.

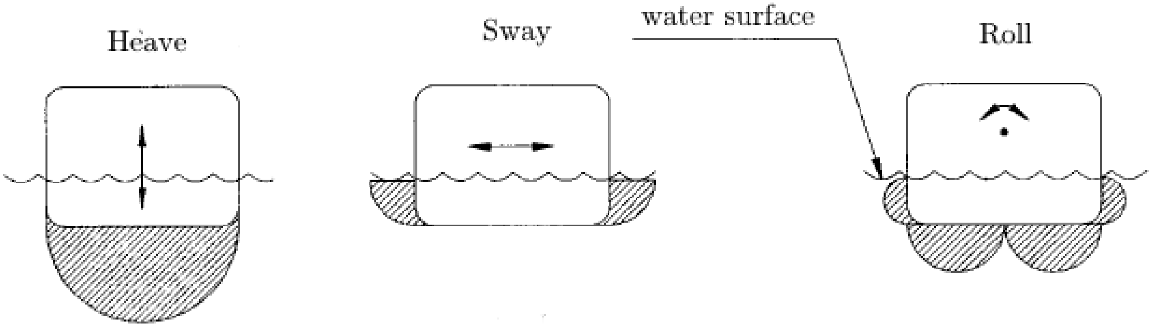

**Figure C.1:** A rough estimate of the added mass around floating structures in 2D, moving in three directions: heave, surge and pitch (Barltrop, 1998).

Added mass for heave was estimated by a hemisphere with the base at the bottom of the GBF, given by:

$$m_z = \rho \frac{2}{3} \pi r^3. \tag{C.1}$$

For surge motions, the added mass consists of an ellipse around the GBF, as stated by Barltrop (1998), which is given by:

$$m_x = \rho \pi r^2 d, \tag{C.2}$$

in which $d$ is the draft of the GBF. Added mass for pitch was more difficult to determine.

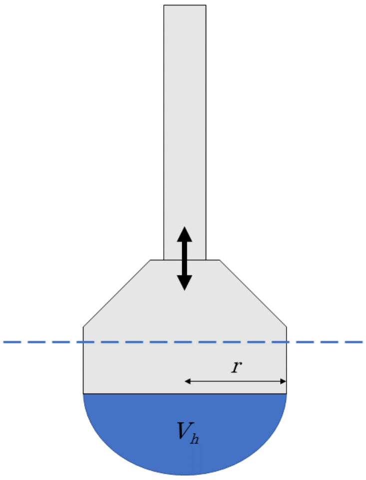

**Figure C.2:** Heave added mass as the shaded area in a side view of the GBF

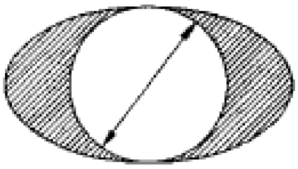

**Figure C.3:** surge added mass as the shaded area in a top view of the GBF

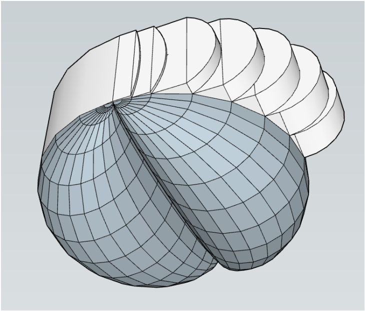

**Figure C.4:** Pitch added mass as seen in 3D from the bottom of the GBF.

In 3D, pitch added mass on the bottom of the GBF was estimated to have a shape of a 'croissant'. Added mass on the sides of the GBF was estimated to have the shape of a 'banana', with a decreasing radius of the semi-circle while moving towards the ends of the GBF. These shapes are based on the idea that added mass volumes consist of semicircles on submerged structure sections, as in Figure C.1 for pitch, which decrease in area when moving to the sides of the structure, as in Figure C.3. The added mass for pitch is visualised in Figure C.4. For these volumes of water, moment of inertia with respect to the center of gravity was calculated.

Pitch added mass, $I_\varphi$ was determined using numerical integration of the volumes and was calculated to be 7.57E08 kg m$^2$. Although the heave and surge added mass have been based on clear literature sources, pitch added mass was estimated based on assumptions. Pitch added inertia for a vertical floating cylinder was also calculated by Ghadimi et al. (2012), using:

$$m_z = C_m \rho \pi r^2 \left( \frac{(d)^3}{3} + \overline{KG}^2 (d) + \overline{KG} (d)^2 \right), \tag{C.3}$$

in which $C_m$ is the added mass coefficient for surge (3500000/7000000 = 0.50) and $d$ is the draft. This equations results in a pitch added inertia of 4.06E+08 kg m$^2$. This value of the pitch added inertia was used as the final result of the mathematical calculations. The pitch added inertia determined by Ghadimi et al. was used instead of the mathematical approach discussed.

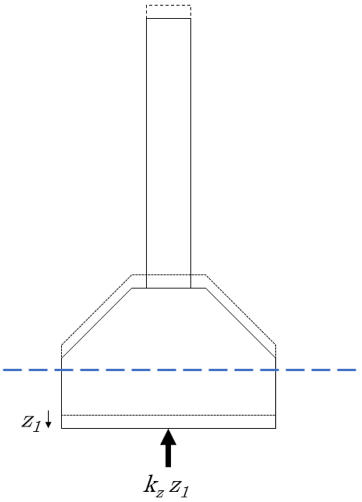

**Figure C.5:** Vertical displacement $z_1$

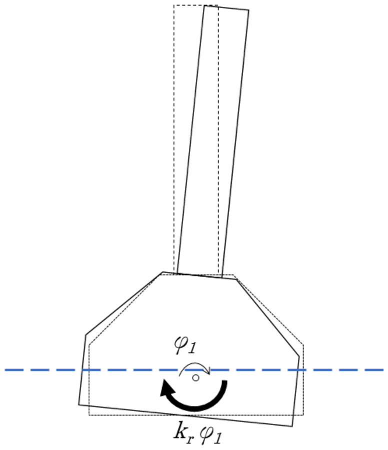

**Figure C.6:** Rotation $\varphi_1$

## C.2 Restoring spring terms

In the vertical direction, a downward displacement is restored by a vertical hydrostatic force. This force can be calculated using Archimedes's principle. A downward displacement of $z_1$ results in a displaced volume of water of $z_1 \pi R^2$, with a corresponding upward (restoring) force of $z_1 \rho g \pi R^2$. The vertical spring coefficient is therefore equal to:

$$k_z = \rho g \pi R^2 \tag{C.4}$$

According to Journée and Massie (2001), the righting moment of a floating structure due to a rotation is given by:

$$M_\varphi = \rho g \nabla \cdot \overline{GM} \cdot \sin \varphi, \tag{C.5}$$

in which $\nabla$ is the submerged volume of the floating structure. For small angles, $\sin \varphi \approx \varphi$ and the restoring rotational spring coefficient is then given by:

$$k_\varphi = \rho g \nabla \cdot \overline{GM} \tag{C.6}$$

## C.3 Damping

Damping of floating structures can be divided into two main components that differ greatly in their physics. Viscous damping is caused by viscous effects such as for example skin friction and vortices. In radiation damping, energy is dissipated by generated radiation waves of the moving structure. For heave motions, both damping components were expected to be significant while for pitch motions, it was expected that damping is mainly viscous. Viscous damping is, however, non-linear and dependant on frequency and amplitude of the motion (Journée & Massie, 2001). Although non-linearity is no issue mathematically, linear damping components for heave and pitch were sought for to be able to simplify the models and to compare results easily. According to Journée and Massie (2001), linearization of the quadratic damping coefficient can be done by:

$$c_i^{lin} = \frac{8}{3\pi} \cdot \omega \cdot A_0 \cdot c_i^{vis} \tag{C.7}$$

in which:

$c_i^{lin}$ = linearized damping in the $i$ degree of freedom
$\omega$ = angular frequency [rad/s]
$A_0$ = motion amplitude [m or rad]
$c_i^{vis}$ = non-linear quadratic damping in the $i$ degree of freedom

Since the structure floats freely in the water, its natural frequency was used for $\omega$. The mathematical models were compared to the physical scale model so the amplitude of the average displacement in the physical scale model tests was used to calculate the linear damping coefficient.

Horizontal motions are damped by viscous drag on the GBF moving through the water. Drag on the GBF due to a horizontal velocity is given by:

$$F_d = \frac{1}{2}\rho v^2 C_d A \tag{C.8}$$

in which:

$\rho$ = mass density of the fluid [kg/m$^3$]
$v = \dot{x}$ = velocity of the object moving though the fluid [m/s]
$C_d = 0.6$ = drag coefficient [-]
$A = 2R \cdot d(t)$ = Surface area of the structure exposed to the water flow [m$^2$]
$d(t) = d_0 - z(t)$ = draft [m]

The drag coefficient of 0.60 is assumed for horizontal motions of the GBF. The non linear damping component in the governing matrices (dependent on $\dot{x}^2$) is then equal to:

$$c_x = \frac{1}{2}C_d\rho 2R(d_0 - z(t)). \tag{C.9}$$

(Jiang et al., 2013) calculated non-dimensional radiation damping for submerged vertical cylinders in heave and pitch motions. Their calculation of radiation damping is frequency dependent so an estimation of the natural frequency is required before the coefficients can be determined. For now, the natural frequency in heave will be estimated by $\omega_z = \sqrt{\frac{k_z}{m+m_z}}$, and for pitch $\omega_\varphi = \sqrt{\frac{k_\varphi}{I_y+m_\varphi}}$. Using the values from Tables 3.2 and 3.3 which were calculated using the formula's described above, resulting in $\omega_\varphi = 0.430$ rad/s and $\omega_z = 0.705$ rad/s.

In the rotational $\varphi$-direction, damping mainly consist of viscous damping according to (Jiang et al., 2013) so radiation damping is neglected. Viscous damping of vertical floating cylinders for pitch was determined by (Mansouri & Hadidi, 2009), using the formula (which was modified):

$$c_\varphi = c_{11}\left(\frac{(d)^3}{4} + \overline{KG}(d)^2 + \frac{3}{2}\overline{KG}^2(d) + \overline{KG}^3\right), \tag{C.10}$$

in which:

$c_{11} = C_D\rho Rd$ = damping coefficient of surge motion [kg/m]
$C_D = 0.6$ = surge drag coefficient [-]
$\overline{KG}$ = distance from base to the center of gravity [m]
$d = d_0$ = draft [m]

Heave motions are mainly subject to radiation damping. Heave (radiation) damping is given by (Jiang et al., 2013):

$$c_z^{rad} = 0.2\rho R^2(gR)^{1/2} \tag{C.11}$$

Heave viscous damping can also be approximated by (Mansouri & Hadidi, 2009):

$$c_z^{vis} = 0.5 C_D^P \rho \pi R^2, \tag{C.12}$$

in which $C_D^p = 2$ according to (Mansouri & Hadidi, 2009). Linearization is done according to Equation C.7 with a value of $\phi_z = 3.3$ m for the amplitude (this corresponds to the average amplitude of the harmonics measured used during the experiments, see Figure 5.1) and $\omega_z$ as stated above. The total damping is given by $c_z = c_z^{rad} + c_z^{lin}$.

## C.4 Results

Using the formulas described in the above sections, values for the hydrodynamic components of the matrices were determined. The table below shows the results from the analytical calculations as well as the ANSYS Aqwa output. A calibration of the results based on physical scale model tests is made in Chapter 5.

**Table C.1:** Heave hydrodynamic components. Aqwa results were calculated for a natural frequency of 0.119 Hz

| Parameter | Symbol | Analytical | Aqwa | Unit |
|---|---|---|---|---|
| Added mass | $m_z$ | 7.43E+06 | 5.57E+06 | kg |
| Hydrostatic stiffness | $k_z$ | 7.17E+06 | 7.16E+06 | N/m |
| Linear radiation damping | $c_z$ | 5.69E+05 | 1.08E+06 | Ns/m |
| Linearized viscous damping | $c_z^{lin}$ | 1.44E+06 | 0 | Ns/m |

**Table C.2:** Pitch hydrodynamic components. Aqwa calculations were performed at a natural frequency of 0.067 Hz

| Parameter | Symbol | Analytical | Aqwa | Unit |
|---|---|---|---|---|
| Added mass | $m_\varphi$ | 4.06E+08 | 1.78E+08 | kg m$^2$ |
| Hydrostatic stiffness | $k_\varphi$ | 2.93E+08 | 2.96E+08 | Nm/rad |
| Linear radiation damping | $c_\varphi$ | 0 | 6.86E+05 | Nm/(rad/s) |
| Linearized viscous damping | $c_\varphi^{lin}$ | 1.50E+08 | 0 | Nm/(rad/s) |

**Table C.3:** Surge hydrodynamic components.

| Parameter | Symbol | Analytical | Unit |
|---|---|---|---|
| Added mass | $m_x$ | 3.5E+06 | Nm$^2$/rad |
| Damping | $c_x$ | 1.50E+08 | Nm/(rad/s) |

# Appendix D

# ANSYS Aqwa

This appendix briefly describes the theory and output of the ANSYS Aqwa model used to determine the hydrodynamic coefficients in the equations of motion for a floating GBF.

## D.1 Theory and Model

The structure is exited through a Froude-Krylov force and a diffraction force caused by the response of the floating body itself. The response to these forces is (numerically) evaluated and radiation forces due to body oscillations are computed. For complex geometries in the three-dimensional space, the problem is solved using the fluid potential theory in which the structure is formed by a series of diffracting panels. For each diffracting panel, the boundary conditions and governing differential equations are solved. The fluid is assumed to be inviscid, incompressible and irrotational. Fluid potential theory describes the mechanics of fluids and is based on mass and momentum conservation. In his thesis, Kelkitli (2018) gives a clear and concise explanation of ANSYS Aqwa theory:

“In the case of relatively small amplitude waves, the incident wave forcing is defined by the the linear (first order) Froude-Krylov force corrected by a diffraction force which is induced by the disturbance wave because of the existence of an oscillating body. Firstly, AQWA solves the diffraction and Froude-Krylov forcing for complex geometry systems. In some other cases, like larger or severe seas, the second order waves and transient forces may also be interesting to consider. Although AQWA solves these, they will not be included in this report because they do not fall within the scope of this work. Secondly, the radiation forces due to the disturbance waves caused by the oscillation of a considered body are also computed by AQWA. This problem for complex geometries is generally solved using three dimensional panel methods based on the fluid potential theory, representing the surface of the structure or structures by a series of wave diffracting panels. Fluid potential theory is the description of the mechanics of fluids that satisfy the basic laws of fluid mechanics, namely the conservation of mass and momentum. This theory assumes that the fluid is incompressible, inviscid and irrotational, similar to the linear wave theory. A fine explanation of the fluid potential theory can be found in the Offshore Hydromechanics lecture notes by Journée and Massie (2001). AQWA also can compute the Morison drag forces on slender bodies, but this is not relevant to this research and is therefore omitted. As the surface of the structure is split into multiple panels, the differential equations and boundary conditions governing the fluid motion around the structure can be solved. This solution method is referred to as a boundary integration approach, where the fluid velocity potential is solved by input conditions. This integration occurs with the use of the Greene’s function, which simply put, states that each panel contains a source term that with the use of the hull wetted surface boundary condition can be solved. Solving these source terms will yield the solution to the diffraction and radiation problem. The AQWA Theory manual chapter 4 gives a more comprehensive and elaborate explanation of this method and clearly states the equations that are solved in the AQWA code. The differential equation and boundary conditions that are solved are also given there. Some key assumptions, as they have been noted in the AQWA Theory Manual, are (ANSYS inc., 2019):

- The oscillating body is assumed to have none or very small forward speed.
- The water is inviscid, incompressible and water flow irrotational.
- All body motions are harmonic and the incident waves have a small amplitude with respect to wavelength, meaning their slope is small."

"

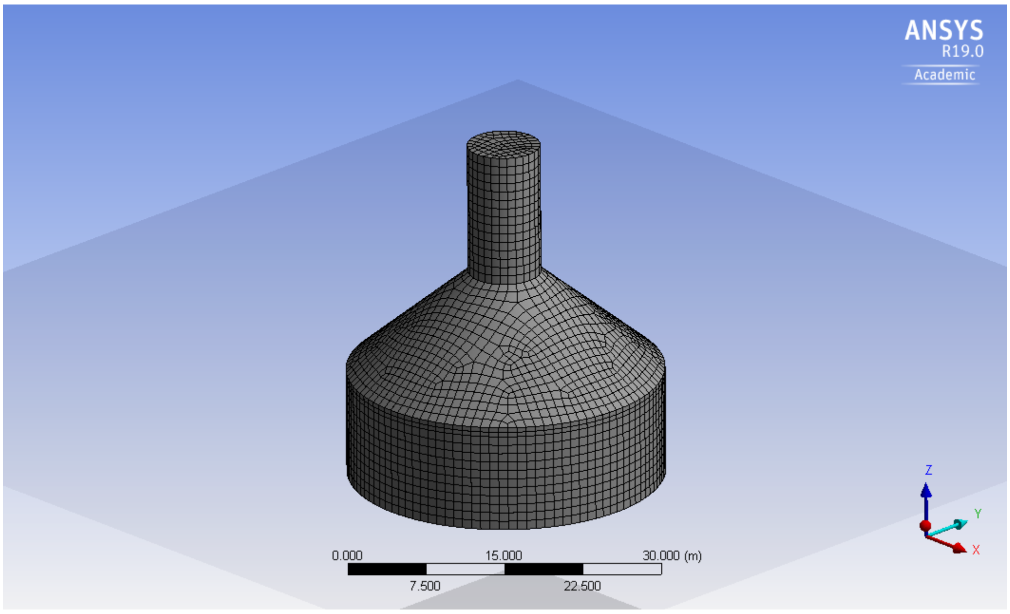

**Figure D.1:** Structure geometry and mesh used in ANSYS Aqwa calculations.

## D.1 Output and results

In Figures D.2 to D.7, the results for the mesh shown in Figure D.1 is shown. The figures show the hydrodynamic components for heave and pitch for a range of frequencies. Since only the natural frequencies are of interest, the RAO's are used to determine the natural frequency and the hydrodynamic components at these frequencies are determined.

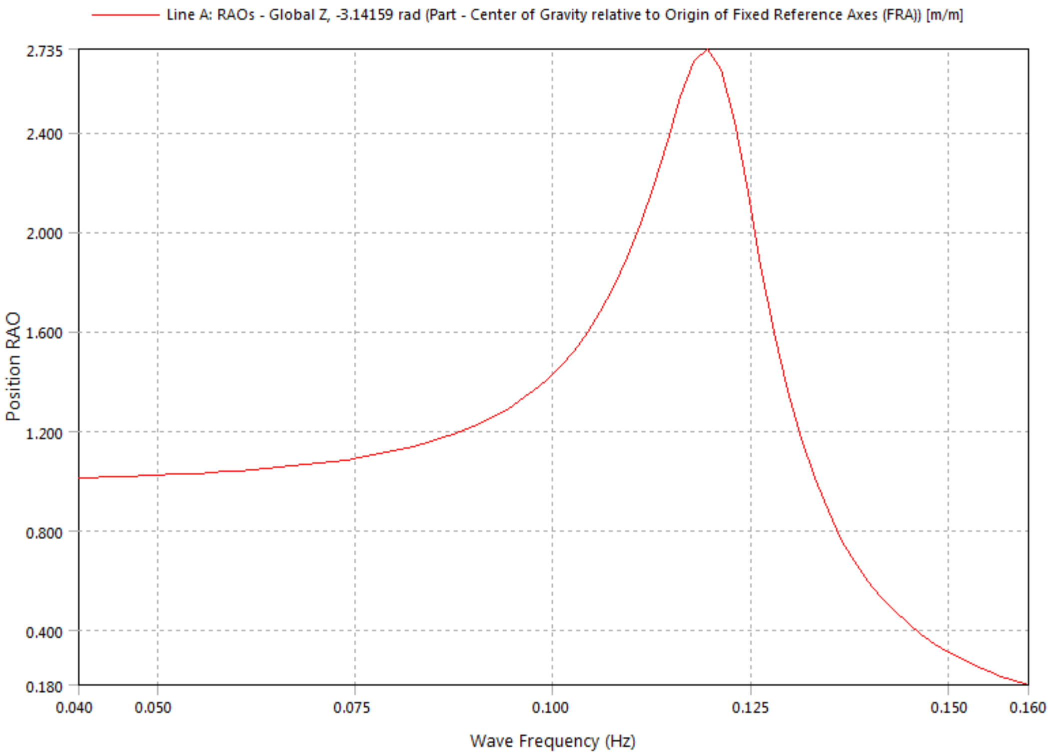

**Figure D.2:** Response Amplitude Operator for heave to determine the natural frequency

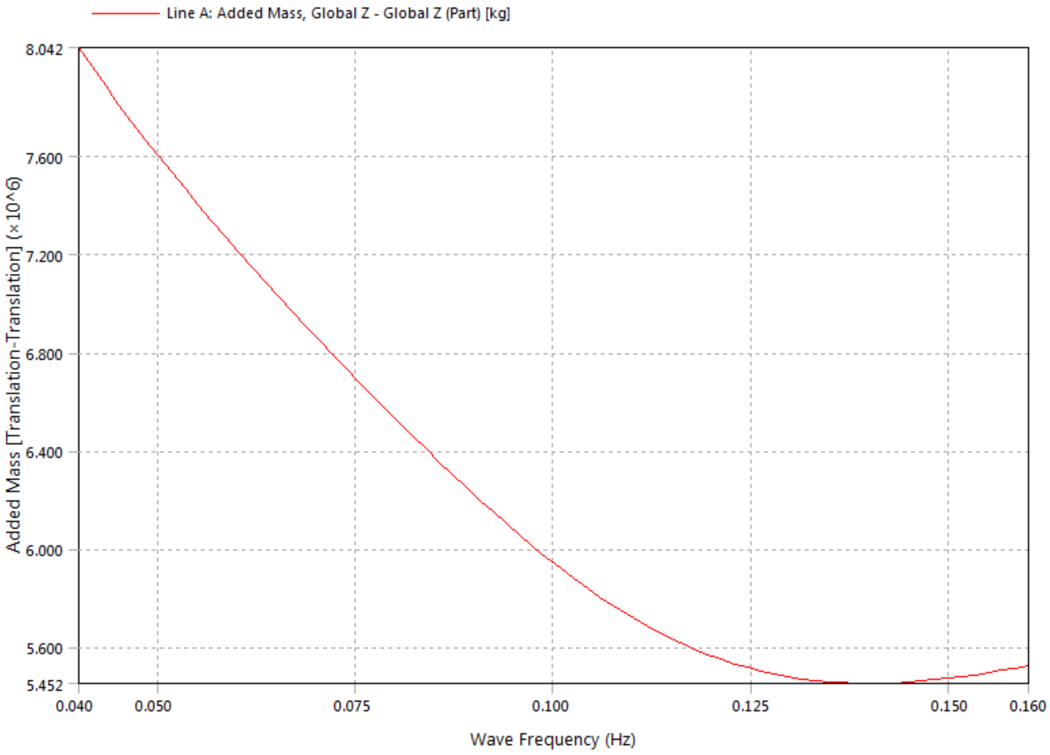

**Figure D.3:** Added mass for heave

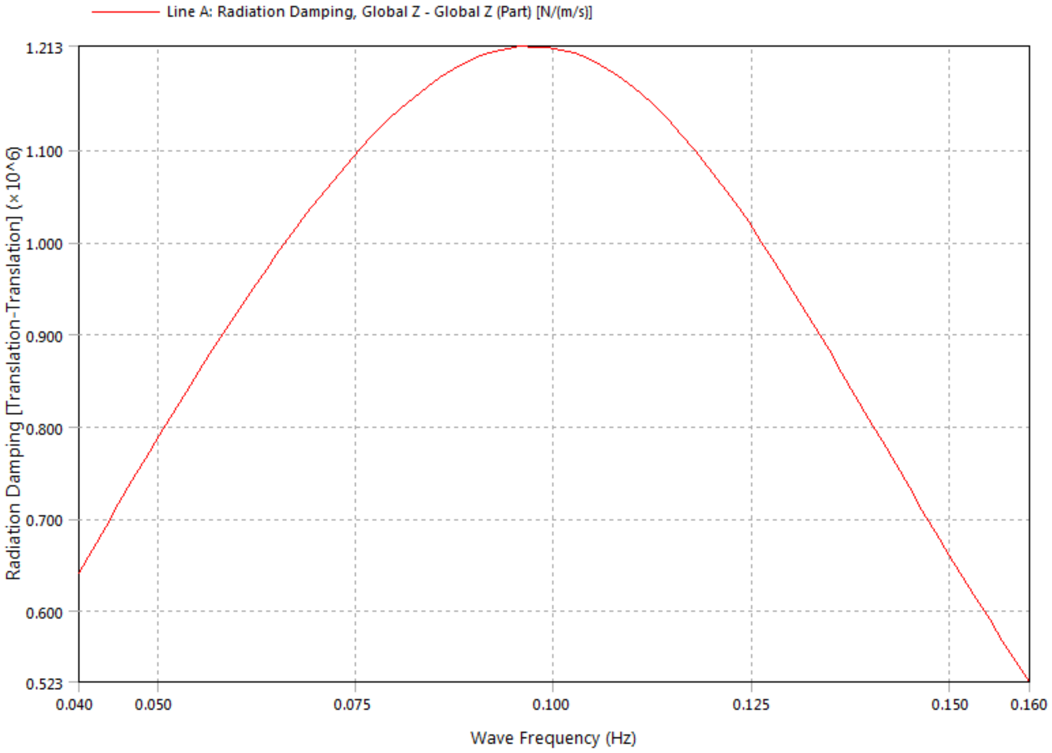

**Figure D.4:** Radiation damping for heave

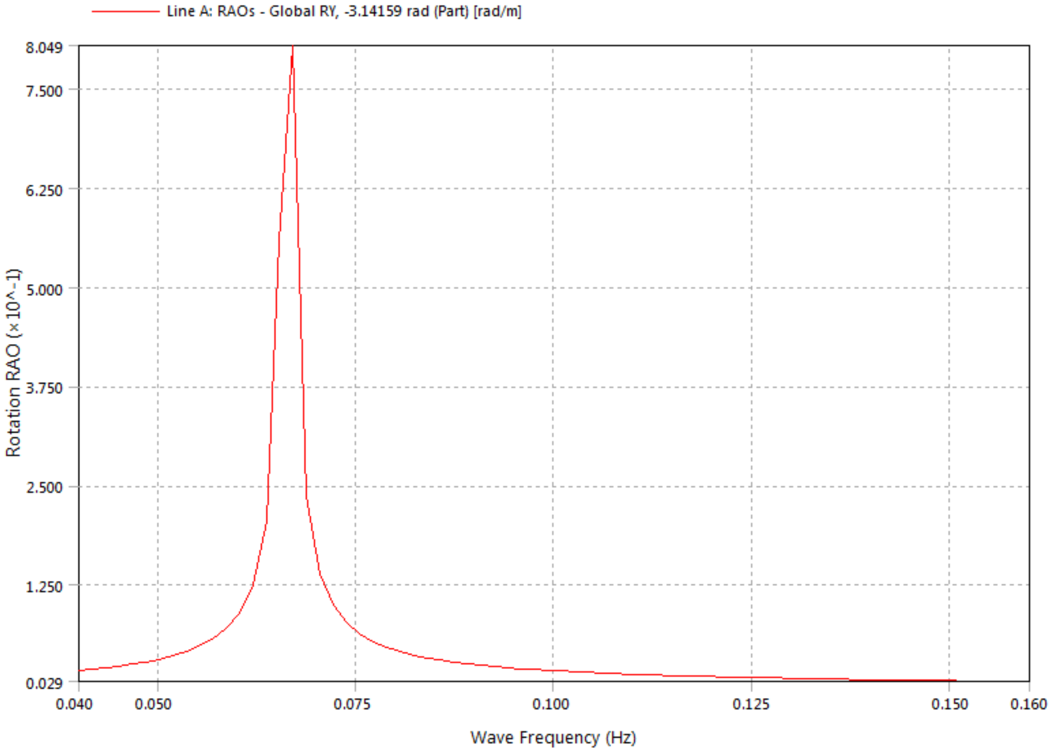

**Figure D.5:** Response Amplitude Operator for pitch to determine the natural frequency

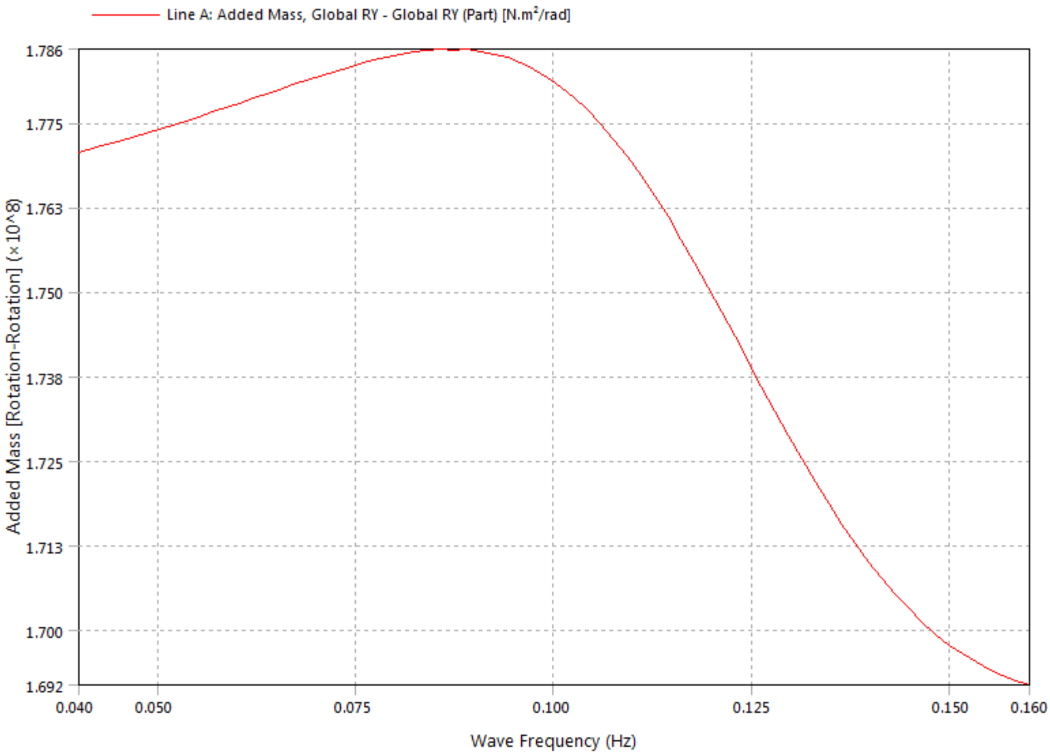

**Figure D.6:** Added mass for pitch. Units are: $kgm^2/rad$, the label in the figure is not correct.

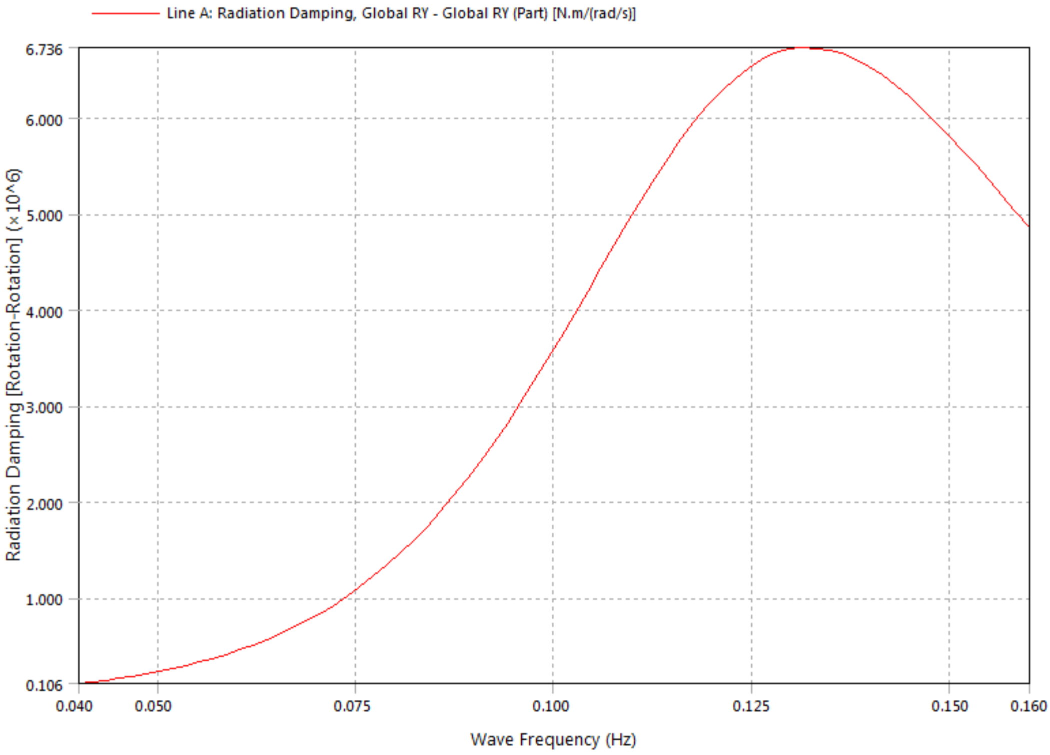

**Figure D.7:** Radiation damping for pitch

# Appendix E

# Experiment

This Appendix elaborates on the experiment set up and results in the main report. A more detailed experiment protocol is presented, as well as the python code used to analyse the videos and all result measurements recorded from the video files.

## E.1 Experiment Protocol

1. place GBF on slipway in 'high' or 'low' position
2. walk to and start far camera
3. walk to the set up
4. start close camera
5. Film the experiment number in the video for proper administration.
6. Remove the support (release the string) to set the GBF into motion.
7. After the motions have dissipated or the GBF has moved out of the picture, stop the close camera.
8. repeat steps 3-7 two more times
9. place the GBF in the position that was not used in step 1
10. repeat steps 3-8 three times
11. walk to the far camera and stop the video recording.

The resulting video file contains 6 launches, 3 for the 'low' position and 3 for the 'high' position. The above procedure is repeated 9 times, for three different slipway inclinations (9°, 14° and 21°) and for three different freeboards (-2 cm, 0 cm and +4 cm).

## E.2 Video Analysis

In this, Python code used to analyse the video (using the motion tracking software) is shown.

```
from collections import deque
from imutils.video import VideoStream
import numpy as np
import math as math
import argparse
import cv2
import imutils
import time
import pandas as pan
import matplotlib.pyplot as plt
from scipy.optimize import curve_fit
from scipy.signal import find_peaks

# construct the argument parse and parse the arguments
ap = argparse.ArgumentParser()
ap.add_argument("-v", "--video", default="14DHL20.mp4", help="path to
    the (optional) video file")
ap.add_argument("-b", "--buffer", type=int, default=50000, help="max 
    buffer size")
args = vars(ap.parse_args())

#frames per second of the video file
frames = 50

# define the lower and upper boundaries of the "green"
# ball in the HSV color space, then initialize the
# list of tracked points

pycolorLower = (colorLower[0]/2, colorLower[1]*255/100, colorLower
    [2]*255/100)
pycolorUpper = (colorUpper[0]/2,  colorUpper[1]*255/100, colorUpper
    [2]*255/100)

greenLower = pycolorLower
greenUpper = pycolorUpper

ptsc = deque(maxlen=args["buffer"])
ptsr = deque(maxlen=args["buffer"])
# if a video path was not supplied, grab the reference
# to the webcam
if not args.get("video", False):
    vs = VideoStream(src=0).start()

# otherwise, grab a reference to the video file
else:
    vs = cv2.VideoCapture(args["video"])

# allow the camera or video file to warm up
#time.sleep(2.0)
```

```
# keep looping
while True:
    # grab the current frame
    frame = vs.read()

    # handle the frame from VideoCapture or VideoStream
    frame = frame[1] if args.get("video", False) else frame

    # if we are viewing a video and we did not grab a frame,
    # then we have reached the end of the video
    if frame is None:
        break

    # resize the frame, blur it, and convert it to the HSV
    # color space
    frame = imutils.resize(frame, width=1920)
    blurred = cv2.GaussianBlur(frame, (11, 11), 0)
    hsv = cv2.cvtColor(blurred, cv2.COLOR_BGR2HSV)

    # construct a mask for the color "green", then perform
    # a series of dilations and erosions to remove any small
    # blobs left in the mask
    mask = cv2.inRange(hsv, greenLower, greenUpper)
    mask = cv2.erode(mask, None, iterations=2)
    mask = cv2.dilate(mask, None, iterations=2)

    # find contours in the mask and initialize the current
    # (x, y) center of the ball
    cnts = cv2.findContours(mask.copy(), cv2.RETR_EXTERNAL, cv2.
       CHAIN_APPROX_SIMPLE)
    cnts = imutils.grab_contours(cnts)
    center = None

    # only proceed if at least one contour was found
    if len(cnts) > 0:
        # find the largest contour in the mask, then use
        # it to compute the minimum enclosing circle and
        # centroid
        c = max(cnts, key=cv2.contourArea)
        (x, y), radius = cv2.minEnclosingCircle(c)
        M = cv2.moments(c)
        center = (int(M["m10"] / M["m00"]), int(M["m01"] / M["m00"]))
        rect = cv2.minAreaRect(c)
        box = cv2.boxPoints(rect)
        box = np.int0(box)
        cv2.drawContours(frame,[box],0,(0,0,255),2)
        # only proceed if the radius meets a minimum size
        if radius > 10:
            # draw the circle and centroid on the frame,
            # then update the list of tracked points
```

```
            cv2.circle(frame, (int(x), int(y)), int(radius),
                       (0, 255, 255), 2)
            cv2.circle(frame, center, 5, (0, 0, 255), −1)

    # update the points queue
    ptsc.appendleft(center)
    ptsr.appendleft(rect)


    # show the frame to our screen
    cv2.imshow(”Frame”, frame)
    key = cv2.waitKey(1) & 0xFF

    # if the ’q’ key is pressed, stop the loop
    if key == ord(”q”):
        break

# if we are not using a video file, stop the camera video stream
if not args.get(”video”, False):
    vs.stop()

# otherwise, release the camera
else:
    vs.release()

# close all windows
cv2.destroyAllWindows()

# horizontal coordinates = 0, vertical coordinates = 1
crd1 = np.zeros(len(ptsc))
crd2 = np.zeros(len(ptsc))
for i in range(len(ptsc)):
    crd1[i] = ptsc[i][0]
    crd2[i] = ptsc[i][1]

ptsr1=np.array(ptsr)
for j in range(len(ptsr1)):
    if ptsr1[j,2] > −30:
        ptsr1[j,2]=ptsr1[j,2]−90
phi=np.flip(ptsr1[:,2])[start:]+90
```

## E.3 Results

This section contains the measurements of the rotation of the GBF during the launches performed in the physical scale model tests. Three launches were performed for each set-up, so every figure contains results for a single set up.

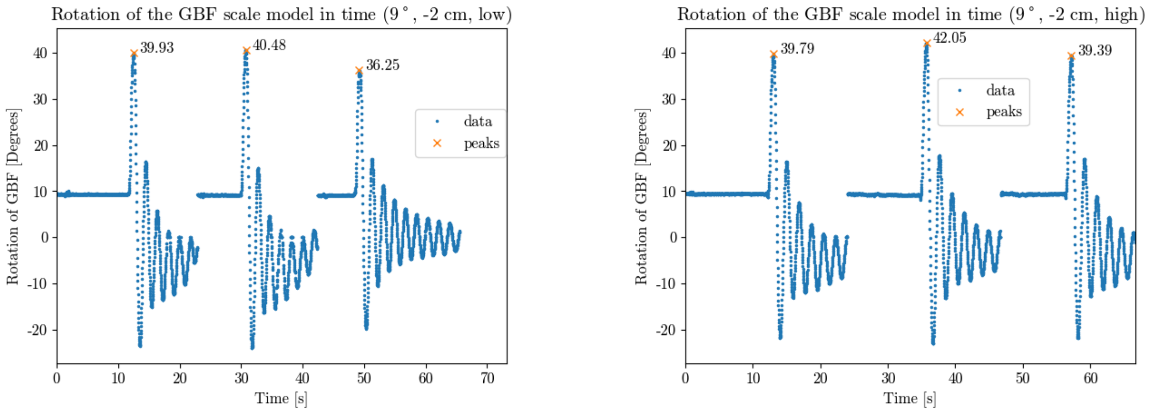

**(a)** Negative freeboard, low initial velocity **(b)** Negative freeboard, high initial velocity

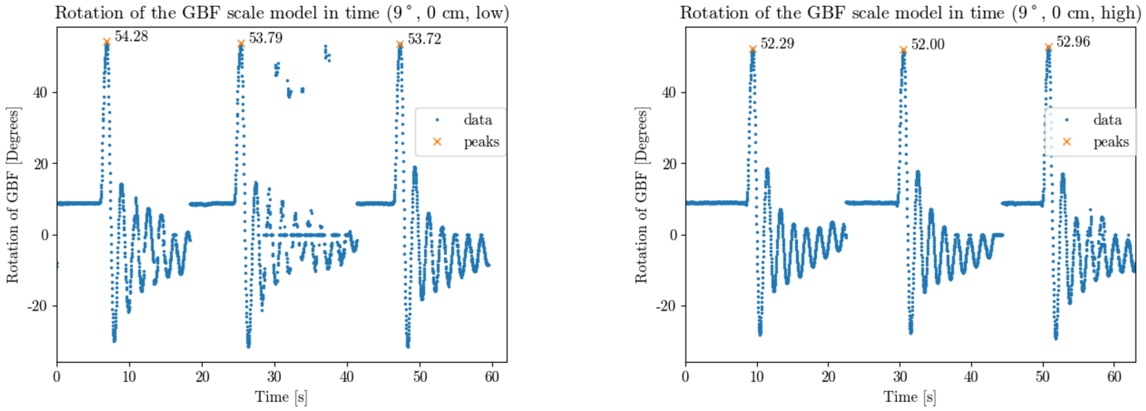

**(c)** Zero freeboard, low initial velocity **(d)** Zero freeboard, high initial velocity

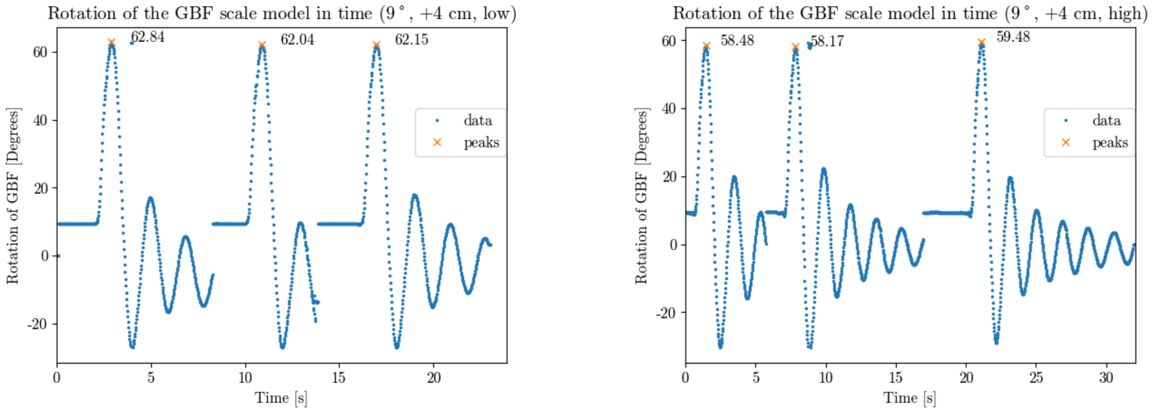

**(e)** Positive freeboard, low initial velocity **(f)** Positive freeboard, high initial velocity

**Figure E.1:** GBF rotation measured during abruptly ending slipway launches performed at 9°.

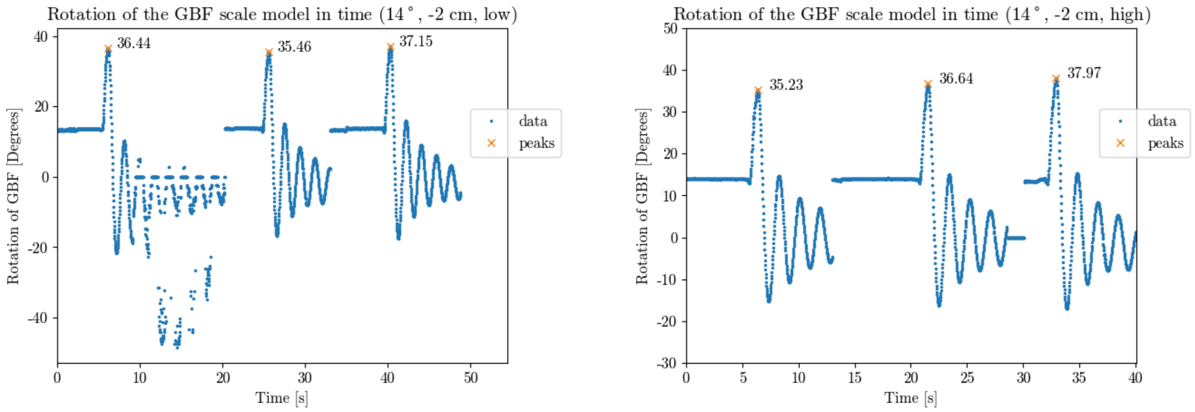

**(a)** Negative freeboard, low initial velocity **(b)** Negative freeboard, high initial velocity

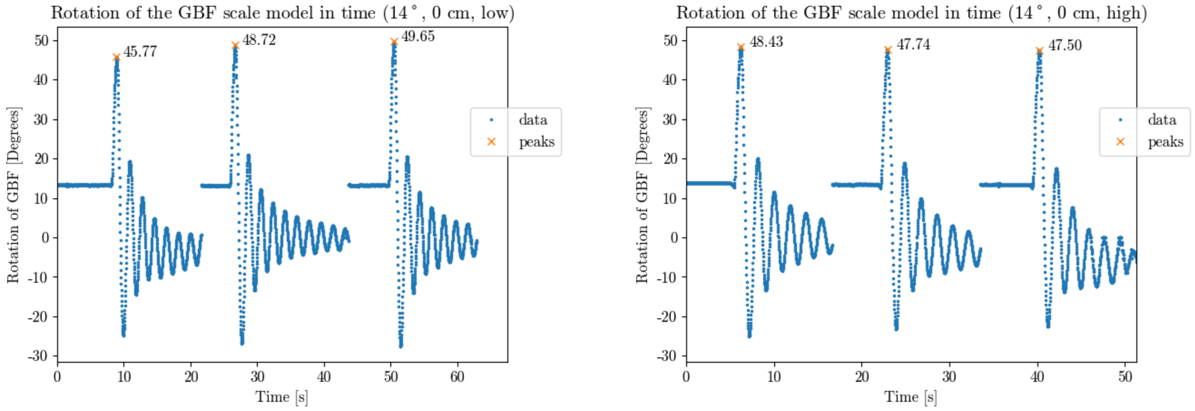

**(c)** Zero freeboard, low initial velocity **(d)** Zero freeboard, high initial velocity

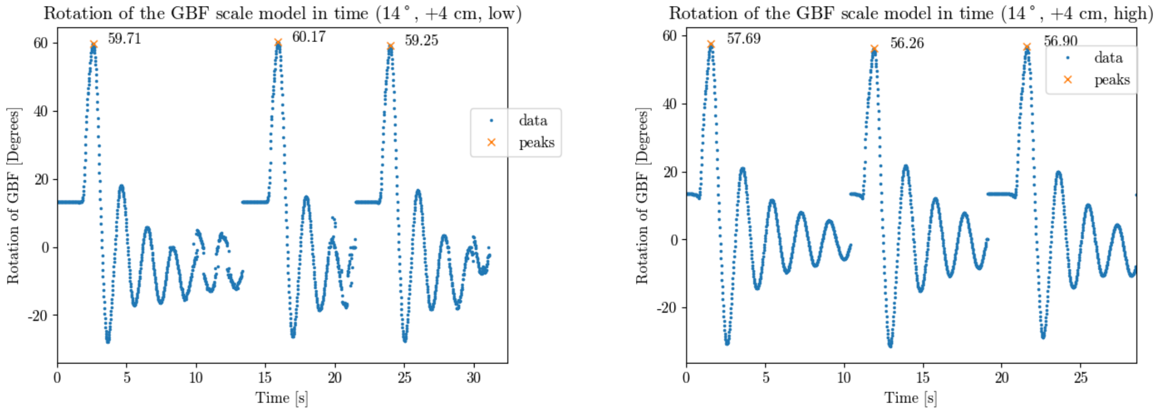

**(e)** Positive freeboard, low initial velocity **(f)** Positive freeboard, high initial velocity

**Figure E.2:** GBF rotation measured during abruptly ending slipway launches performed at 14°.

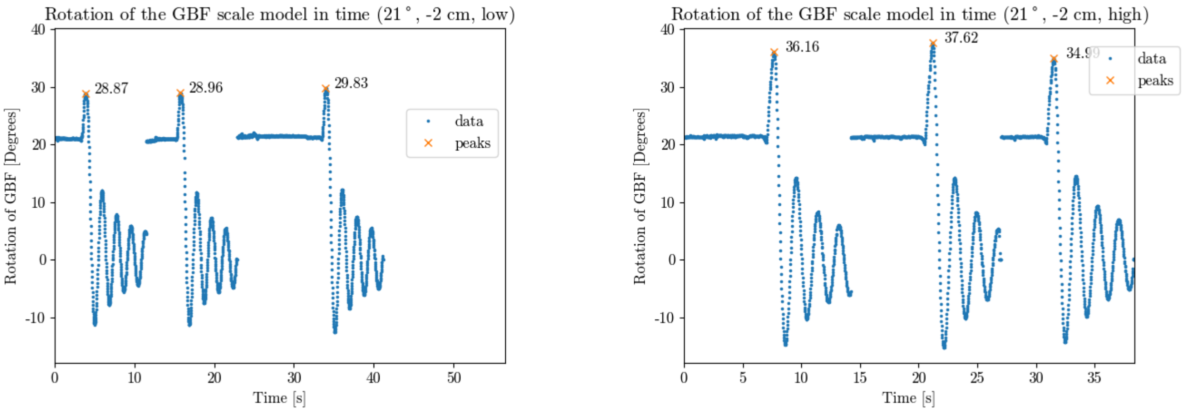

**(a)** Negative freeboard, low initial velocity **(b)** Negative freeboard, high initial velocity

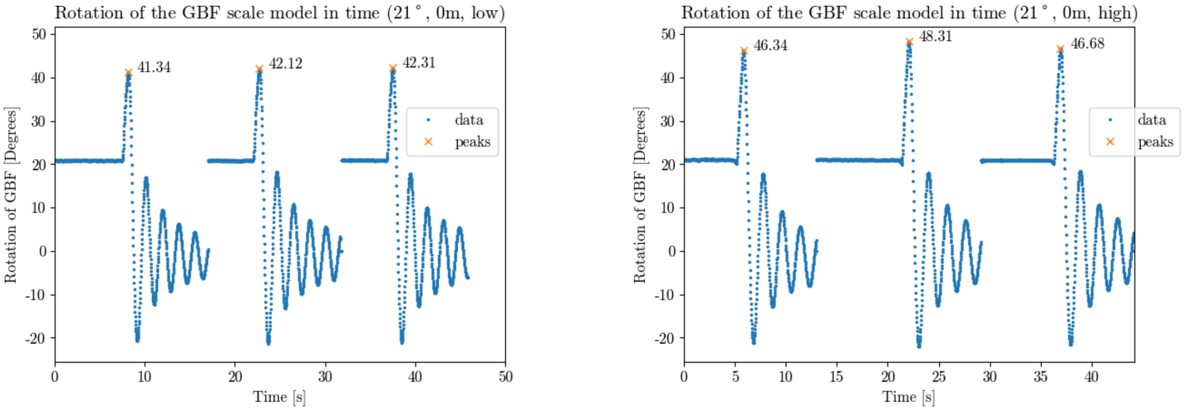

**(c)** Zero freeboard, low initial velocity **(d)** Zero freeboard, high initial velocity

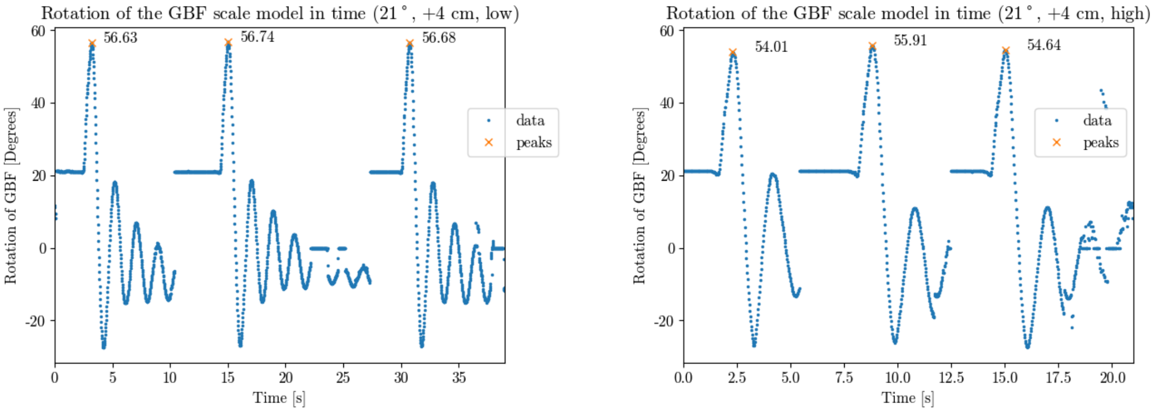

**(e)** Positive freeboard, low initial velocity **(f)** Positive freeboard, high initial velocity

**Figure E.3:** GBF rotation measured during abruptly ending slipway launches performed at 21°.

# Appendix F

# ANSYS Fluent model settings

This appendix contains the Fluent settings report that can be used to reproduce the model in ANSYS Fluent. This was the settings report of the model run at 1:1 scale.

## Summary

| | |
|---|---|
| Project: | **3D_pitch** |
| Date: | **9-10-2019** |
| Time: | **22:06:28** |
| Product Version: | **Release 19.0** |
| Last Saved Version: | **Release 19.0** |

## Project Schematic View

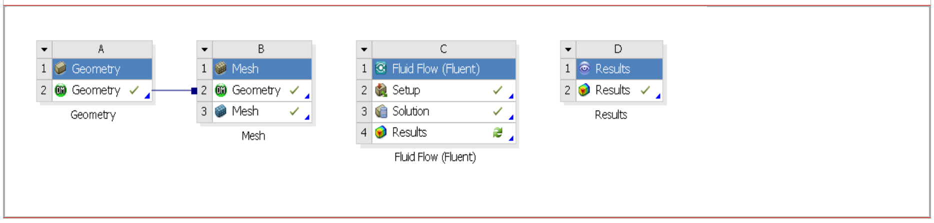

## FFF : Solution : dp0

```
Fluent
Version: 3d, dp, pbns, dynamesh, vof, ske, transient (3d, double precision, pressure-
based, dynamic mesh, VOF, standard k-epsilon, transient)
Release: 19.0.0
Title:


Models
------

   Model                        Settings
   ----------------------------------------------------------------
   Space                        3D
   Time                         Unsteady, 1st-Order Implicit
   Viscous                      Standard k-epsilon turbulence model
   Wall Treatment               Standard Wall Functions
   Heat Transfer                Disabled
   Solidification and Melting   Disabled
   Species                      Disabled
   Coupled Dispersed Phase      Disabled
   NOx Pollutants               Disabled
   SOx Pollutants               Disabled
   Soot                         Disabled
   Mercury Pollutants           Disabled


Material Properties
-------------------

   Material: water-liquid (fluid)

      Property                        Units      Method      Value(s)
      -------------------------------------------------------------
```

```
      Density                         kg/m3     constant   998.2
      Cp (Specific Heat)              j/kg-k    constant   4182
      Thermal Conductivity            w/m-k     constant   0.6
      Viscosity                       kg/m-s    constant   0.001003
      Molecular Weight                kg/kmol   constant   18.0152
      Thermal Expansion Coefficient   1/k       constant   0
      Speed of Sound                  m/s       none       #f

   Material: air (fluid)

      Property                        Units     Method     Value(s)
      ---------------------------------------------------------------
      Density                         kg/m3     constant   1.225
      Cp (Specific Heat)              j/kg-k    constant   1006.43
      Thermal Conductivity            w/m-k     constant   0.0242
      Viscosity                       kg/m-s    constant   1.7894e-05
      Molecular Weight                kg/kmol   constant   28.966
      Thermal Expansion Coefficient   1/k       constant   0
      Speed of Sound                  m/s       none       #f

   Material: aluminum (solid)

      Property               Units    Method     Value(s)
      ---------------------------------------------------
      Density                kg/m3    constant   2719
      Cp (Specific Heat)     j/kg-k   constant   871
      Thermal Conductivity   w/m-k    constant   202.4


Cell Zone Conditions
--------------------

   Zones

      name    id   type
      ------------------
      fluid   3    fluid

   Setup Conditions

      fluid

         Condition       Value
         ---------------------
         Frame Motion?   no
         Mesh Motion?    no


Boundary Conditions
-------------------

   Zones

      name              id   type
      --------------------------------------
      wall-fluid        1    wall
      pressure_outlet   7    pressure-outlet
      wall_gbf          13   wall

   Setup Conditions

      wall-fluid
```

```
         Condition                   Value
         ---------------------------------
         Wall Motion                 0
         Shear Boundary Condition    0
         Wall Roughness Height (m)   0.05

      pressure_outlet

         Condition   Value
         -----------------

      wall_gbf

         Condition                   Value
         ---------------------------------
         Wall Motion                 0
         Shear Boundary Condition    0
         Wall Roughness Height (m)   0.05


Solver Settings
---------------

   Equations

      Equation          Solved
      ------------------------
      Flow              yes
      Volume Fraction   yes
      Turbulence        yes

   Numerics

      Numeric                         Enabled
      ---------------------------------------
      Absolute Velocity Formulation   yes

   Unsteady Calculation Parameters


      -------------------------------------
      Time Step (s)                   0.005
      Max. Iterations Per Time Step   15

   Relaxation

      Variable                     Relaxation Factor
      ----------------------------------------------
      Pressure                     0.3
      Density                      1
      Body Forces                  1
      Momentum                     0.7
      Turbulent Kinetic Energy     0.8
      Turbulent Dissipation Rate   0.8
      Turbulent Viscosity          1

   Linear Solver

                                   Solver     Termination   Residual Reduction
      Variable                     Type       Criterion     Tolerance
      ------------------------------------------------------------------------
      Pressure                     V-Cycle    0.1
      X-Momentum                   Flexible   0.1           0.7
```

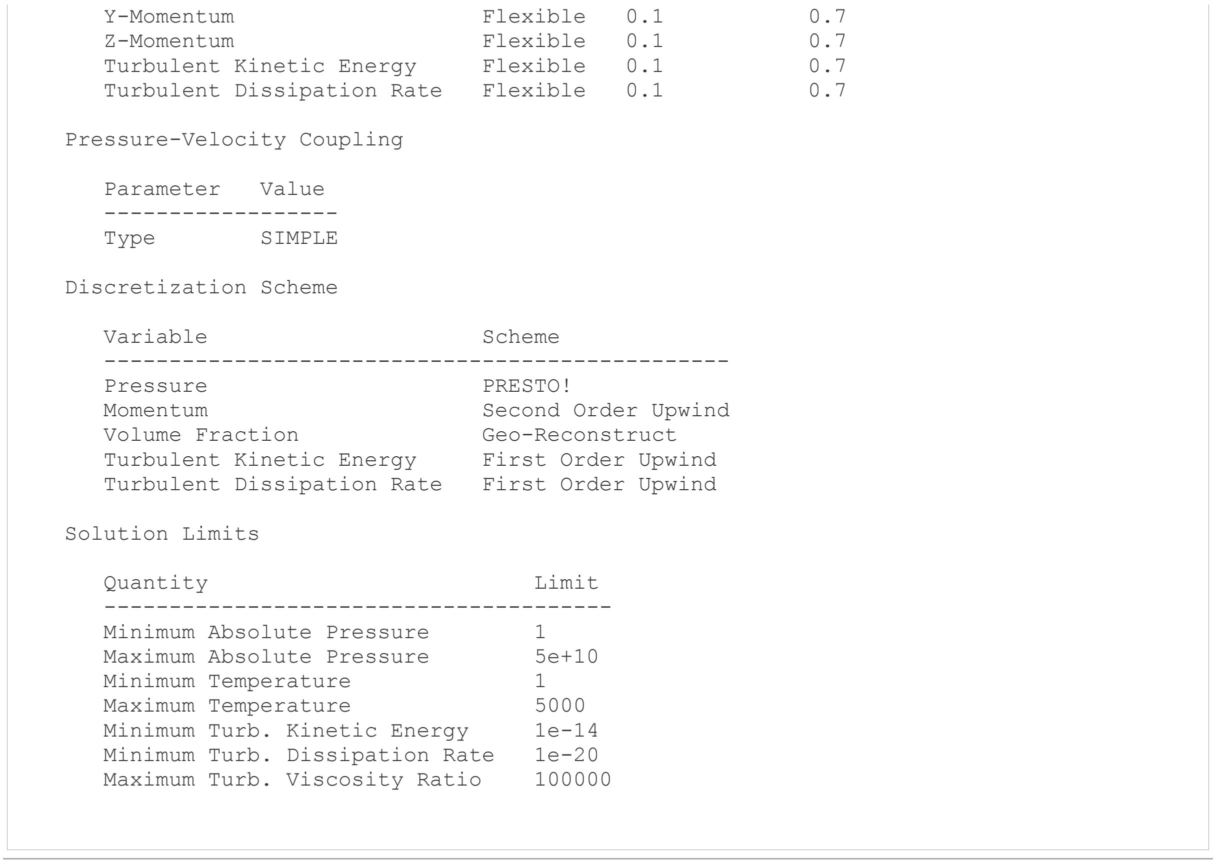

```
      Y-Momentum                   Flexible   0.1           0.7
      Z-Momentum                   Flexible   0.1           0.7
      Turbulent Kinetic Energy     Flexible   0.1           0.7
      Turbulent Dissipation Rate   Flexible   0.1           0.7

   Pressure-Velocity Coupling

      Parameter   Value
      ------------------
      Type        SIMPLE

   Discretization Scheme

      Variable                     Scheme
      ------------------------------------------------
      Pressure                     PRESTO!
      Momentum                     Second Order Upwind
      Volume Fraction              Geo-Reconstruct
      Turbulent Kinetic Energy     First Order Upwind
      Turbulent Dissipation Rate   First Order Upwind

   Solution Limits

      Quantity                         Limit
      ---------------------------------------
      Minimum Absolute Pressure        1
      Maximum Absolute Pressure        5e+10
      Minimum Temperature              1
      Maximum Temperature              5000
      Minimum Turb. Kinetic Energy     1e-14
      Minimum Turb. Dissipation Rate   1e-20
      Maximum Turb. Viscosity Ratio    100000
```

# References

ANSYS inc. (2019). ANSYS Fluent Theory Guide [Computer software manual].

ANSYS Inc. (2019). ANSYS Fluent User Guide [Computer software manual].

Avci, O. (2016). Amplitude-Dependent Damping in Vibration Serviceability: Case of a Laboratory Footbridge. *Journal of Architectural Engineering*, *22*. doi: 10.1061/(ASCE)AE.1943-5568.0000211

BAM. (2017). *GBF float out* [Internal project image folder].

Barltrop, N. D. P. (1998). *Floating Structures - A Guide for Design and Analysis, Volumes 1-2.* Energy Institute.

Bewell, R. (2018). Construction and Installation of 5No. Gravity Base Foundations for offshore wind turbines. In *Ced working day 2018.*

Birkeland, F. M. (2016). *Numerical Simulation of Installation of XL Monopile for Offshore Wind Turbines* (Unpublished doctoral dissertation). Norwegian University of Science and Technology.

Börkey GmbH. (n.d.). *Individuelle Konstruktionen.* Retrieved from `http://boerkey-gmbh.de/de/produktuebersicht/waelzwagen/individuelle-konstruktionen/?cn-reloaded=1&cn-reloaded=1`

Bruce, G. J., & Eyres, D. J. (2012). *Ship Construction* (7th ed.). Elsevier.

Campbell, T., Kong, W., & Manning, D. (1990). Laboratory Investigation of the Coefficient of Friction in the Tetrafluorethylene Slide Surf ace of a Bridge Bearing. *TRANSPORTATION RESEARCH RECORD*, 45–52.

de Jong, C., & Ainslie, M. (2012). *Underwater sound due to piling activities for Prinses Amaliawindpark* (Tech. Rep.). Den Haag: TNO.

de Jong, D. (2016). *Report Structural Design Loads* (Tech. Rep.). Gouda: BAM.

De Jong, E. (2010). *Dockwise investement research* (Tech. Rep.). SNS Securities.

De Silva, C. (2005). *Vibration and shock handbook.* Boca Raton: Taylor & Francis.

EDF. (2018). *Blyth Offshore Demonstrator Windfarm — EDF Renewables.* Retrieved from `https://www.edf-re.uk/our-sites/blyth`

Energinet.dk. (2015). *Technical Project Description for Offshore Wind Farms (200 MW)* (Tech. Rep.).

ESA. (2011). Recycled oil rigs could aid life in the deep seas. Retrieved from `https://www.esa.org/esablog/research/recycled-oil-rigs-could-aid-life-in-the-deep-seas/`

ESDEP. (n.d.). *ESDEP LECTURE NOTE [WG15A].* Retrieved from `http://fgg-web.fgg.uni-lj.si/~/pmoze/ESDEP/master/wg15a/l0900.htm#SEC_4`

European Environment Agency. (2009). *Europe's onshore and offshore wind energy potential: An assessment of environmental and economic constraints* (Tech. Rep.). doi: 10.2800/11373

European Wind Energy Association. (2012). *The European offshore wind industry key 2011 - trends and statistics* (Tech. Rep.). European Wind Energy Association.

European Wind Energy Association. (2013). *Deep water - the next step for offshore wind energy* (Tech. Rep.).

European Wind Energy Association. (2015). *Wind energy scenarios for 2030* (Tech. Rep.).

Fitriadhy, A., & Malek, A. (2017). Computational fluid dynamics analysis of a ship's side launching in restricted waters. *Journal of Mechanical Engineering and Sciences*, *11*(4), 2993–3003.

flow3d.com. (2019). *Understanding Relaxation and Convergence Criteria — CFD-101.* Retrieved from `https://www.flow3d.com/resources/cfd-101/numerical-issues/relaxation-and-convergence-criteria/`

Garus, K. (2016). *EEW has produced the world's heaviest Monopile — Offshore Wind Industry.* Retrieved from `http://www.offshorewindindustry.com/news/eew-produced-worlds-heaviest-monopile`

Ghadimi, P., Paselar Bandari, H., & Bankhshandeh Rostami, A. (2012). Determination of the Heave and Pitch Motions of a Floating Cylinder by Analytical Solution of its Diffraction Problem and Examination of the Effects of Geometric Parameters on its Dynamics in Regular Waves. *International Journal of Applied Mathematical Research*, *1*(4). doi: 10.14419/ijamr.v1i4.396

GS Yard. (2010). *Tewaterlating TMS Eventus.* Retrieved from `https://www.gsyard.nl/nieuws-en-agenda/detail/id/7/titel/tewaterlating-tms-eventus`

Hak, B. (2005). *Numerical simulation of the side launching of a ship* (Unpublished doctoral dissertation). University of Groningen.

Heinis, F. (2015). *Effecten van aanleg op zeezoogdieren* (Tech. Rep.).

Hermans, K. W., & Peeringa, J. M. (2016). *Future XL monopile foundation design for a 10 MW wind turbine in deep water* (Tech. Rep.).

Hickel, S. (2018). CFD for Aerospace Engineers..

Jacobsen, S. (2019). IEA says offshore wind set to become $1 trillion industry by 2040 — World Economic Forum. *World Economic Forum.* Retrieved from `https://www.weforum.org/agenda/2019/11/offshore-wind-energy-industry`

Jiang, S.-c., Gou, Y., & Teng, B. (2013, 10). Water Wave Radiation Problem by a Submerged Cylinder. *Journal of Engineering Mechanics*, *140*(5), 06014003. doi: 10.1061/(asce)em.1943-7889.0000723

John Rogers. (2017). *Key Messages on US Offshore Wind, in 5 New Quotes - Union of Concerned Scientists.* Retrieved from `https://blog.ucsusa.org/john-rogers/offshore-wind-quotes`

Journée, J. M. J., & Massie, W. W. (2001). *Offshore Hydromechanics* (1st ed.). Delft University of Technology.

Kelkitli, I. (2018). *Analysis of the Ocean Falls Wave Energy Converter in Regular Waves* (Master's thesis). TU Delft.

Koschinski, S., & Ludeman, K. (2011). *Development of Noise Mitigation Measures in Offshore Wind Farm Construction* (Tech. Rep.).

Koster, R. (2019, 7). *Miljarden nodig voor opruimen olie- en gasplatforms Noordzee.* Retrieved from `https://nos.nl/nieuwsuur/artikel/2291601-miljarden-nodig-voor-opruimen-olie-en-gasplatforms-noordzee.html`

Kundu, P. K., Cohen, I. M., & Dowling, D. R. (2012). *Fluid mechanics.* Elsevier Inc.

Kuron, M. (2015). 3 Criteria for Assessing CFD Convergence. *www.engineering.com.* Retrieved from `https://new.engineering.com/story/3-criteria-for-assessing-cfd-convergence-`

Leanwind. (2017). *Driving Cost Reductions in Offshore Wind THE LEANWIND PROJECT FINAL PUBLICATION* (Tech. Rep.).

Mansouri, R., & Hadidi, H. (2009). Comprehensive Study on the Linear Hydrodynamic Analysis of a Truss Spar in Random Waves. *International Journal of Mathematical and Computational Sciences*, *3*(5).

Muttray, M. (2019). [Personal conversation on 7 November 2019].

Oh, K.-Y., Nam, W., Ryu, M. S., Kim, J.-Y., & Epureanu, B. I. (2018). A review of foundations of offshore wind energy convertors: Current status and future perspectives. *Renewable and Sustainable Energy Reviews*, *88*, 16–36. doi: 10.1016/J.RSER.2018.02.005

ombugge. (2016). *Shipyards of the World - CaptainsVoyage™ Forums.* Retrieved from `https://www.captainsvoyage-forum.com/forum/windjammer-bar-maritime-interest/general-maritime-interrest-from-cruise-to-the-mercantile-marine-and-all-ships-between/2546-shipyards-of-the-world/page3`

Panton, R. L. (2013). *Incompressible Flow* (Fourth ed.). John Wiley & Sons, Incorporated.

Qingdao Eversafe Marine Engineering Co. (n.d.). *Heavy lifting and transfer.* Retrieved from `http://www.eversafe-marine.com/design.aspx?cid=14`

Rodriguez, C. A., Moura, M., Esperança, P. T. T., & Raigorodsky, J. (2014). An Experimental Approach for the Offshore Launching of Jack-Ups. *Journal of Offshore Mechanics and Arctic Engineering*, *136*(2). doi: 10.1115/1.4026478

Rosebrock, A. (2015). *Ball Tracking with OpenCV - PyImageSearch* [web page]. Retrieved from `https://www.pyimagesearch.com/2015/09/14/ball-tracking-with-opencv/`

Schaaf, T. V. D., & Sas, F. (2013). *MTP 2411 " Organisatie van Scheepsproductie 2 " Dictaat Tewaterlaten.*

Slater, S. (2016). Five ways to float your boat. *Hakai Magazine*. Retrieved from `https://www.hakaimagazine.com/article-short/five-ways-float-your-boat/`

Ten Oever, E. (2019). [Personal conversation on 7 November 2019].

Ten Oever, E., & Overbeeke, S. (2017). Reinforced concrete Gravity Base Foundations, Blyth Project Concrete Gravity Base Foundation. In *Bam gbf lezing kivi.* bam.

The Construction Index. (2016). Blyth debut for BAM gravity base foundations. *The Construction Index.* Retrieved from `https://www.theconstructionindex.co.uk/news/view/blyth-debut-for-bam-gravity-base-foundations`

TNO. (n.d.). *Design limitations for future very large monopiles — TNO.* Retrieved from `https://www.tno.nl/en/focus-areas/ecn-part-of-tno/roadmaps/towards-large-scale-generation-of-wind-energy/support-structure-just-as-important-as-the-wind-turbine-itself/design-limitations-for-future-very-large-monopiles/`

Topham, E., & McMillan, D. (2017). Sustainable decommissioning of an offshore wind farm. *Renewable Energy*, *102*, 470–480. doi: 10.1016/j.renene.2016.10.066

Tuin, J. (2018). *Optimal construction and transportation method for gravity based foundations for offshore wind farms on commercial scale* (Master's thesis). TU Delft.

Tupper, E. C., & Rawson, K. J. (2001). *Basic Ship Theory* (5th ed.). Elsevier Science & Technology.

Weisstein, E. W. (n.d.). *Cylindrical Wedge.* Mathworld - A Wolfram Web Resource. Retrieved from `http://mathworld.wolfram.com/CylindricalWedge.html`

WindEurope. (2018). *Offshore Wind in Europe - Key trends and statistics 2017* (Tech. Rep.).

www.4offshore.com. (2019). *Global Offshore Wind Farm Database.* Retrieved from `https://www.4coffshore.com/windfarms/`

www.bam150years.com. (n.d.). *Offshore windfarm gravity base foundations — BAM 150.* Retrieved from `https://www.bam150years.com/en/projects/offshore-windfarm-gravity-base-foundations`

Ye, Z. (1994). Dynamics of ships side launching. *Computers and Structures*, *53*(4), 861–865. doi: 10.1016/0045-7949(94)90374-3

YouTube. (2017). *Caisson construction 4x10m launch.* `https://www.youtube.com/watch?v=tLe84VVDB4k`. (Online; accessed 10 July 2019)